

# Modeling Transcutaneous Electrical Stimulation

A dissertation submitted to

ETH ZURICH

for the degree of

Doctor of Sciences

presented by

ANDREAS KUHN

Dipl. El.-Ing. ETH/ MSc. ETH

born 11 June 1979

citizen of Schwerzenbach ZH

accepted on the recommendation of

Prof. Dr. Manfred Morari, examiner

Prof. DDDr. Frank Rattay, co-examiner



# Acknowledgments

I would like to thank Prof. Manfred Morari who enabled me to make my PhD in the Electrical Stimulation Group of the Automatic Control Lab. Especially I emphasize two points that I am grateful for: First, during the discussion about possible projects, Prof. Morari advised me to join the Electrical Stimulation Group. Because of my interest in Biomedical Engineering I was quickly convinced that this was the right choice and in retrospective it was a very good advice. The second point is that Prof. Morari was able to ask the right questions during our meetings. He gave new ideas and asked the key questions in order to guide the project towards the right direction.

With Prof. Frank Rattay I have had one of the world leading researchers in the field of neural modeling as co-examiner. I would like to thank him for the time he invested to read this theses and his positive feedback, which was an honor for me.

I would also like to thank Thierry who was my supervisor for three years (2004-2007). I would like to thank him for many good discussions and arguments during his time at the Automatic Control Lab. These discussions and arguments enabled us to better understand our problems and to find good solutions.

Then I would like to thank Marc. I enjoyed to share office with him the last four years. Apart from our scientific discussions we have had a lot to laugh together. I also would like to thank all other colleagues from the Automatic Control Lab for the pleasant and inspiring atmosphere.

Furthermore, I appreciate the good collaboration with our industrial partners: SPEAG (Schmid & Partner Engineering AG), Compex Médical SA, Bischoff Textil AG, and EMPA. It was nice to see the application of our research in actual products.

Special thanks belong to my girlfriend Corinne who always supported me with her love but also with her scientific knowledge.

Finally, I would like to express my gratitude to my parents who are always here for me. By teaching me good values they enabled me to reach my envisioned goals.

Zurich, September 2008

ANDREAS KUHN



# Abstract

Transcutaneous electrical stimulation (TES) is a technique to artificially activate motor nerves and muscles by applying electrical current pulses to pairs of electrodes placed on the skin surface. TES can be used for sports, fitness, rehabilitation, and restoration of lost motor functions, e.g. in subjects with brain or spinal cord lesions. In this thesis a versatile TES simulation framework (TES model) that calculates nerve activation using a finite element model combined with non-linear nerve models was developed. The aim of this model was to investigate new TES technologies and to better understand specific effects in TES. Nerve activation in the TES model was calculated either in nerve bundles or by using activation volumes which describe whole regions where nerves are activated. Computer graphics methods were applied to the activation volumes in order to introduce measures to estimate the activation depth and the selectivity.

The TES model and its parametrization were verified using experimental measurements that were undertaken on human volunteers. Three types of measurements were performed and compared with the TES model:

- Voltage measurements using surface electrodes that measured the potential on the skin and needle electrodes in order to measure intramuscular voltages.
- Motor thresholds on the volunteers were measured using an accelerometer that was placed on the stimulation electrode.
- Finger forces were measured during TES using a grasp assessment system.

A sensitivity study was performed in order to quantify the influence of different model parameters on nerve activation (e.g. capacitive effects, electrode-skin contact resistance, electrode material resistance, or nerve depth). This revealed the parameters with the largest influence in TES and allowed us to conclude which model simplifications can be made.

One of the goals of TES systems is to selectively activate motor nerves in order to accomplish a specific motor function. However, TES

will not only activate the targeted motor nerves, but also sensory nerves in adjacent nerve bundles and sensory receptors in the skin. Such sensory activation may be uncomfortable, indeed painful, and can limit the effectiveness of TES. The presented TES model was expanded by a pain index which was based on experiments. This allowed us to identify optimized electrode sizes which maximize selectivity and comfort when stimulating motor nerves.

Array electrodes are a promising technology that is likely to bring transcutaneous electrical stimulation (TES) a step forward. The dynamic adaptation of electrode size and position helps to simplify the use of electrical stimulation systems and to increase their clinical efficacy. However, up to now array electrodes were designed by trial and error and it was unclear how, for example, the gaps between the array elements or the resistivity of the electrode-skin interface material influence the current distribution. Using the TES model, design rules for the gap sizes and gel resistivities were derived in order to limit the losses and to produce uniform activation fields.

# Zusammenfassung

Mittels Transkutaner-Elektrostimulation (TES) können motorische Nerven und Muskeln künstlich aktiviert werden. Dazu werden elektrische Strompulse über Elektroden, welche auf der Haut platziert werden, in den Körper geleitet. TES wird in den Bereichen Sport, Fitness, Rehabilitation und zur Wiederherstellung von verlorenen motorischen Funktionen verwendet (z.B. bei Personen mit Schlaganfall oder Querschnittlähmung). In dieser Arbeit wurde eine TES Simulations-Umgebung entwickelt mit welcher die Nervenaktivierung berechnet werden kann. Die Berechnung erfolgt in zwei Schritten; zuerst wird mit einer Finite-Elemente-Simulation die Potentialverteilung berechnet und anschliessend mit einem nicht-linearen Nerven-Modell auf die Aktivierung geschlossen. Das Ziel dieses Modells ist einerseits die Untersuchung von neuen TES-Technologien und andererseits die Möglichkeit zu schaffen, spezifische Effekte von TES besser zu verstehen. Die Nerven-Aktivierung im TES-Modell wurde entweder in Nerven-Bündeln oder mittels Aktivierungs-Volumen berechnet, welche die Aktivierung in ganzen Gebieten beschreiben. Mittels geometrischen Methoden wurde basierend auf den Aktivierungs-Volumen die Aktivierungs-Tiefe und die Selektivität berechnet.

Das TES-Modell und dessen Parametrisierung wurden mittels Experimenten an Freiwilligen verifiziert. Drei unterschiedliche Arten von Messungen wurden durchgeführt und mit dem TES-Modell verglichen:

- Mit Elektroden auf der Hautoberfläche und Nadelelektroden wurde die Spannung auf der Hautoberfläche und im Innern des Muskels gemessen.
- Die motorische Reizschwelle wurde mit Beschleunigungssensoren gemessen.
- Die von den Fingern produzierten Kräfte wurden mit einem Kraft-Messsystem gemessen.

Die Einflüsse unterschiedlicher Parameter (z.B. Kapazitäten, Kontaktwiderstand Elektrode-Haut, Elektrodenmaterialwiderstand oder Nerventiefe) wurde mit einer Sensitivitätsanalyse untersucht. Die Resultate zeigten, welche Parameter in der transkutanen Elektrostimulation dominant sind und welche Modellvereinfachungen zulässig sind.

Eines der Ziele von TES-Systemen ist die gezielte, selektive Aktivierung von bestimmten motorischen Nerven, um eine bestimmte motorische Funktion zu erreichen. Durch die Stimulation werden aber gleichzeitig auch sensorische Nerven und sensorische Rezeptoren aktiviert. Diese ungewollte Aktivierung kann unangenehm oder sogar schmerzhaft sein und die Effektivität von TES-Systemen einschränken. Das präsentierte TES-Modell wurde mit einem Indikator für den Komfort erweitert, welcher aus Messungen ermittelt wurde. Dies ermöglichte uns Elektrodengrößen, welche die Selektivität und den Komfort maximieren, abzuleiten.

Array-Elektroden sind eine vielversprechende Technologie, welche TES einen Schritt weiter bringen könnte. Die dynamische Anpassung von Elektrodengröße und Position vereinfacht die Anwendung von TES-Systemen und könnte deren klinischen Erfolg verbessern. Bis jetzt wurden die Abstände der einzelnen Elemente und der Widerstand des Elektroden-Haut-Interface von Array-Elektroden durch ausprobieren bestimmt. Mit dem TES-Modell wurde es möglich, für diese Parameter Entwurfsregeln abzuleiten, welche die entstehenden Verluste verkleinern.



# Contents

<b>Acknowledgments</b>	<b>iii</b>
<b>Abstract</b>	<b>v</b>
<b>Zusammenfassung</b>	<b>vii</b>
<b>Notation</b>	<b>xv</b>
<b>I BACKGROUND</b>	<b>1</b>
<b>1. Introduction</b>	<b>3</b>
1.1. Electrical Stimulation (ES) . . . . .	3
1.2. Existing ES models . . . . .	5
1.3. Objective and Contributions of this Thesis . . . . .	8
1.4. Outline of the Thesis . . . . .	8
<b>II TES MODELING</b>	<b>11</b>
<b>2. Anatomy and Neurophysiology of the Human Forearm</b>	<b>13</b>
2.1. Anatomy . . . . .	13
2.2. Neuromuscular System . . . . .	14
2.2.1. Motor Units . . . . .	14
2.2.2. The Neuron . . . . .	15
2.2.3. The Nerve Bundle . . . . .	18
2.2.4. Extracellular Stimulation of Axons . . . . .	18
2.2.5. Rheobase and Chronaxie . . . . .	22
<b>3. TES Model of the Forearm</b>	<b>25</b>
3.1. Model of Electrical Potential Distribution in Human Tissues . . . . .	26
3.1.1. Simple Impedance Model of Biological Tissues . . . . .	27
3.1.2. Equivalent Circuit Models . . . . .	28
3.1.3. General Equations to Describe Static and Transient Potential Distributions in Volume Conductors . . . . .	31

3.1.4.	Different Approaches to Calculate Electrical Potential Distribution within Biological Tissues . . .	32
3.1.5.	FE Model . . . . .	33
3.2.	Excitation Models (Axon Models) . . . . .	37
3.2.1.	Linear Axon Models . . . . .	37
3.2.2.	Non-Linear Axon Models . . . . .	39
3.3.	TES model (Combined FE and Axon Model) . . . . .	40
3.4.	Analysis (Postprocessing) using the TES model . . . . .	42
3.4.1.	AP Prediction using Linear Axon Models . . . . .	43
3.4.2.	Spatial Description of Nerve Activation . . . . .	44
3.4.3.	Limitations of the TES Models . . . . .	48
<b>4.</b>	<b>Verification of the TES Model (Measurements)</b>	<b>51</b>
4.1.	Surface and Intramuscular Potentials . . . . .	51
4.1.1.	Methods . . . . .	52
4.1.2.	Results . . . . .	53
4.1.3.	Discussion . . . . .	54
4.2.	Motor Thresholds, Chronaxie, and Rheobase . . . . .	56
4.2.1.	Methods . . . . .	56
4.2.2.	Results . . . . .	60
4.2.3.	Discussion . . . . .	63
4.2.4.	Conclusion . . . . .	64
4.3.	Recruitment and Forces . . . . .	64
4.3.1.	Methods . . . . .	65
4.3.2.	Results and Discussion . . . . .	67
4.4.	Conclusions . . . . .	68
<b>5.</b>	<b>Accuracy of AP Prediction Methods in TES</b>	<b>71</b>
5.1.	Methods . . . . .	73
5.1.1.	TES Model . . . . .	73
5.1.2.	Relative Threshold Prediction Errors . . . . .	73
5.1.3.	Spatial Prediction Errors . . . . .	74
5.2.	Results . . . . .	75
5.2.1.	Relative Threshold Prediction Errors . . . . .	75
5.2.2.	Spatial Prediction Errors . . . . .	77
5.3.	Discussion . . . . .	79
5.4.	Conclusions . . . . .	80

<b>III INFLUENCE OF TISSUE PROPERTIES ON TES</b>	<b>81</b>
<b>6. Overview</b>	<b>83</b>
<b>7. Electrical Tissues Properties and Tissue Composition</b>	<b>85</b>
7.1. Tissue Permittivities (Capacitive Effects) . . . . .	85
7.1.1. Methods . . . . .	86
7.1.2. Results . . . . .	87
7.1.3. Discussion and Conclusions . . . . .	88
7.2. Tissue Resistivities . . . . .	89
7.2.1. Non-linearity of Skin Resistance . . . . .	89
7.2.2. Common Resistivity Changes . . . . .	92
7.3. Detailed Anatomical Model (Segmentation from MRI) . . . . .	94
7.3.1. Methods . . . . .	97
7.3.2. Results . . . . .	100
7.3.3. Discussion and Conclusions . . . . .	102
7.4. Bone Position and other Inhomogeneities . . . . .	103
7.4.1. Methods . . . . .	103
7.4.2. Results . . . . .	104
7.4.3. Discussion and Conclusions . . . . .	106
7.5. Tissue Layer Thicknesses . . . . .	106
7.5.1. Methods . . . . .	106
7.5.2. Results and Conclusions . . . . .	106
7.6. Nerve Depth and Axon Diameter . . . . .	107
7.6.1. Methods . . . . .	107
7.6.2. Results . . . . .	107
7.6.3. Discussion and Conclusions . . . . .	110
<b>8. Influence of Nerve Bundles on Extracellular Potential</b>	<b>113</b>
8.1. Introduction . . . . .	114
8.2. Methods . . . . .	114
8.2.1. Finite Element Model . . . . .	114
8.2.2. Nerve Model . . . . .	118
8.2.3. Influence of Single Axon on Extracellular Potential	118
8.2.4. Influence of a Nerve Bundle on the Axon's Ex- tracellular Potential . . . . .	118
8.2.5. Axon Diameter and Electrode-Axon Distance in Nerve Bundle . . . . .	119
8.3. Results and Conclusions . . . . .	119

8.3.1.	Influence of Single Axon on Extracellular Potential	119
8.3.2.	Influence of a Nerve Bundle on the Axon's Extracellular Potential . . . . .	120
8.3.3.	Axon Diameter and Electrode-Axon Distance in Nerve Bundle . . . . .	120
<b>9.</b>	<b>Main Influences in TES (Summary)</b>	<b>123</b>
 <b>IV ELECTRODE PROPERTIES AND ELECTRODE GEOMETRIES</b>		 <b>127</b>
<b>10.</b>	<b>Overview</b>	<b>129</b>
<b>11.</b>	<b>Homogeneous Current Densities using High Resistance Electrodes</b>	<b>131</b>
11.1.	Methods . . . . .	132
11.1.1.	Electrode Edge Effects . . . . .	132
11.1.2.	Small Skin Inhomogeneities (Pores, Glands) . . .	133
11.1.3.	Large Inhomogeneities (Water Content, Structure)	133
11.1.4.	Comparison of Current Densities underneath Inhomogeneities . . . . .	134
11.2.	Results and Discussion . . . . .	135
11.2.1.	Electrode Edge Effects . . . . .	135
11.2.2.	Small Skin Inhomogeneities (Pores, Glands) . . .	137
11.2.3.	Large Inhomogeneities (Water Content, Structure)	138
11.3.	Conclusions . . . . .	140
<b>12.</b>	<b>Single Electrodes</b>	<b>143</b>
12.1.	Explaining Chronaxie Diversity . . . . .	143
12.1.1.	Methods . . . . .	144
12.1.2.	Results and Discussion . . . . .	144
12.1.3.	Conclusions . . . . .	145
12.2.	Influence of Electrode Material on Nerve Activation and Comfort . . . . .	145
12.2.1.	Methods . . . . .	146
12.2.2.	Results and Discussion . . . . .	147
12.2.3.	Conclusions . . . . .	148
12.3.	Optimizing Electrode Size to Stimulate a Certain Depth	149
12.3.1.	Methods . . . . .	150
12.3.2.	Results . . . . .	153

12.3.3. Discussion . . . . .	155
12.3.4. Conclusions . . . . .	158
<b>13. Array Electrode Design</b>	<b>159</b>
13.1. Methods . . . . .	160
13.1.1. Combined FE and Nerve Model . . . . .	160
13.1.2. Influence of Gel Resistivity and Array Gaps on Nerve Activation . . . . .	161
13.1.3. Losses in the Gel Layer when Anode and Cathode are on the same Array . . . . .	164
13.2. Results . . . . .	164
13.2.1. Influence of Gel Resistivity and Array Gaps on Nerve Activation . . . . .	164
13.2.2. Losses in the Gel Layer when Anode and Cathode are on the same Array . . . . .	166
13.3. Discussion . . . . .	169
 <b>V CONCLUSIONS AND OUTLOOK</b>	 <b>173</b>
 <b>VI APPENDIX</b>	 <b>181</b>
<b>A. Anatomy (Muscles in the Forearm)</b>	<b>183</b>
A.1. Flexors in the Forearm . . . . .	183
A.2. Extensors in the Forearm . . . . .	185
<b>B. ArmSimP</b>	<b>187</b>
<b>Bibliography</b>	<b>191</b>
<b>Curriculum Vitae</b>	<b>211</b>



# Notation

## Abbreviations

Abbreviation	Description
AF	Activating function
ANOVA	Analysis of variance
AP	Action potential
CD	Current density
EMG	Electromyography
ES	Electrical stimulation
FE	Finite element
FEM	Finite element model (-ling)
FES	Functional electrical stimulation
FFT	Fast fourier transform
FH	Frankenhaeuser and Huxley
HH	Hodgkin and Huxley
MRG	McIntyre, Richardson, and Grill (name of an axon model)
MRI	Magnetic resonance imaging
PD	Pulse duration (pulse width)
TES	Transcutaneous electrical stimulation
TP	Transmembrane potential
VTK	Visualization toolkit

## Symbols

Symbol	Description
$\Omega$	Ohm (Resistance)
$\Omega m$	Ohm Meter (Resistivity)
$\sigma$	Conductivity [S]
$\rho$	Resistivity [ $\Omega m$ ]
$\varepsilon_r$	Permittivity
$V(x, y, z, t)$	Electric scalar potential
$V_{TP,n}(t)$	Transmembrane potential at node $n$ and time $t$
$V_{e,n}(t)$	Extracellular potential at node $n$ and time $t$
$I_{i,n}(t)$	Ionic current at node $n$ and time $t$
$J_{Na}$	Ionic current density (sodium)
$J_K$	Ionic current density (potassium)
$J_P$	Ionic current density (nonspecific)
$J_L$	Ionic current density (leakage)
$C_m$	Membrane capacitance
$G_a$	Conductance of the axoplasm
$g_L$	Nodal leakage conductance
$\rho_i$	Axoplasmatic resistivity
$I_{rh}$	Rheobase
$T_{ch}$	Chronaxie
$I_{th}$	Threshold current
L	axon depth (measured from fat-muscle interface)
D	axon diameter
$I_{th}(L, D)$	Threshold current required to stimulate axon with diameter D at depth L
$\tau_{sim}$	Time constant of simulated recruitment-duration curve
$\tau_{exp}$	Time constant of measured recruitment-duration curve
<i>Rec</i>	Recruitment
<i>SEL</i>	Selectivity
<i>COMF</i>	Comfort
$Rec_{sat}$	Saturation value of recruitment
$V_{TP}^{th}$	Prediction threshold (TP voltage at $I_{th}$ )
$AF^{th}$	Prediction threshold for AF



Part I

# BACKGROUND



# 1

## Introduction

This chapter provides a general introduction to electrical stimulation (ES) including an analysis of existing and future TES technologies. Subsequently existing models that describe ES are introduced and discussed, focusing on transcutaneous electrical stimulation (TES) models. At the end of the chapter the objectives and contributions of this thesis are introduced and the outline of this thesis is presented.

### 1.1. Electrical Stimulation (ES)

ES is a technique to artificially activate nerve and muscle fibers through the application of electrical current pulses to the body. The electrical current pulse flows between an 'active' (cathode) and an 'indifferent' (anode) electrode, causing a depolarization of cellular membranes in excitable tissues. ES systems can be grouped into implantable, percutaneous, and transcutaneous ES (TES) (through the skin) systems. For the application of most implantable systems complex surgeries are required (e.g. cuff electrodes that are wrapped around nerves [LGD06, WA05]). There exists only one minimally invasive system which can be injected using a syringe (BION (Figure 1.1(a)) [PBL07]). The bio-compatibility of such implantable systems is still problematic

and the performance is unpredictable due to the positioning of the implant during the surgery, long term electrode migration, and soft tissue reactions. In percutaneous ES usually needle electrodes are inserted into the body in order to stimulate specific nerves or muscles. However, this method is also prone to infections because the percutaneous needle electrodes are left within the body. In TES the stimulation electrodes are applied on the skin and can easily be removed after the session and have therefore no bio-compatibility or infection problems.

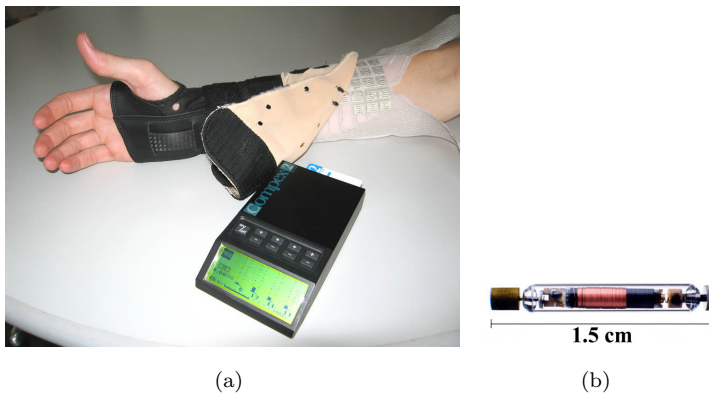


**Figure 1.1.** In 1.1(a) a current TES system using array electrodes is shown and in 1.1(b) the BION implantable microstimulator is depicted.

Electrical stimulation (ES) can be used for many applications within the fields of sports & exercise, pain control, and rehabilitation. In sports electrical stimulation is used to train specific muscle groups in order to train stamina and strength or to relax the muscles after an exercise session (Compex SA). In sports most often TES systems are used and no implantable ones because the application is temporary. In pain control ES decreases pain perception and may be used to control acute and chronic pain [CO04]. Implantable, percutaneous ES, and TES systems are available for pain treatment and compared to chemical medical treatment ES is non-addictive with no known side effects. The low electrical current increases the blood flow and generates heat that serves to relieve stiffness, improve mobility, and relieve pain. The treatment is believed to stimulate the production of endorphins or natural pain killers, however the exact mechanisms are

not completely understood yet. In rehabilitation therapy ES is used to build up muscle mass in specific muscles after bone or ligament injuries [EH79] or for the restoration of movements in subjects who suffer from some form of paralysis due to spinal cord injuries or brain lesions (e.g. stroke) [PSP<sup>+</sup>99, GK98, SNP95]. The aim is a functional improvement to restore, for example, grasping for supporting tasks of daily living [SC07] using so called neuroprostheses or to improve the quality of life (e.g., drop foot, walking, bladder function, coughing), in general. Usually transcutaneous systems [PSP<sup>+</sup>99] are favored over implantable systems [PKK<sup>+</sup>01] because they can be easily removed when the rehabilitation program is completed and the impaired patients are not challenged by surgeries. Different systems were proposed with the aim to improve hand function (e.g. Bionic Glove [PGWK97], Bioness H300 (Handmaster) [ITitG<sup>+</sup>96]) or leg function (e.g. drop-foot [PKP<sup>+</sup>01]). These systems use few large electrodes that do not allow to selectively stimulate specific nerves. Multi-channel array technology was proposed to improve selectivity and efficacy of such TES systems [KLT03, EFP04, PBBJ<sup>+</sup>05] (see Figure 1.1(a)). Array electrodes consist of multiple single elements which can be individually activated to form a virtual electrode of arbitrary size and location. The position and size of the activated region (virtual electrode) can be dynamically changed [LKK04, KLKM06]. For good wearability textile array electrodes are produced using embroidered silver coated fibers to integrate arrays of electrodes into garments [LPK<sup>+</sup>08]. Such new technologies will simplify the application of TES for patients and therapists. The development of these systems raises many questions related to electrode design (shape, material, ...) and electrode positioning (selectivity, comfort, ...). Such questions can be answered using experimental methods; however they are time consuming and depend on the availability of appropriate human subjects. To simplify the design process, dedicated mathematical models can be used to describe the essential aspects of the system in order to reduce the amount and to complement experiments.

## 1.2. Existing ES models

Mathematical models have been developed to describe and better understand the effect of electrical fields on excitable tissues in the human body [McN76, Cob85]. These models improve our understanding of underlying processes by providing the possibility to investigate specific

hypotheses and to analyze relationships that are too laborious to study only with experiments.

It is well known that nerve excitation (action potentials) can be initiated by perturbing the transmembrane potential (TP) of an axon. Hodgkin and Huxley [HH52] developed and experimentally validated a mathematical model of the voltage gated ion channels that describes the TP based on the intracellular and extracellular ionic concentrations. This exceptional work formed the basis for a large number of publications presenting various refined axon excitation models for different types of axon excitation or inhibition [McN76, SMD87, Rat90, MRG02].

McNeal embedded such an axon model in a purely resistive volume conductor that describes the axon's surrounding potential distribution [McN76] and referred to this combined model as two-step model. The first step describes the electrical potential distribution within the electrode-tissue interfaces and the bulk tissues (volume conductor) (see Figure 1.2) based on the exciting electrodes. The second step describes the complex behavior of the axons' transmembrane potential (TP), which depends upon the spatiotemporal potential distribution along the axon. This two-step approach is implemented in most ES models [Cob85, Rat88, MG02, RMMR04, MRRM04, LGD06] and is applied to peripheral and central nerves, for anodic and cathodic currents.

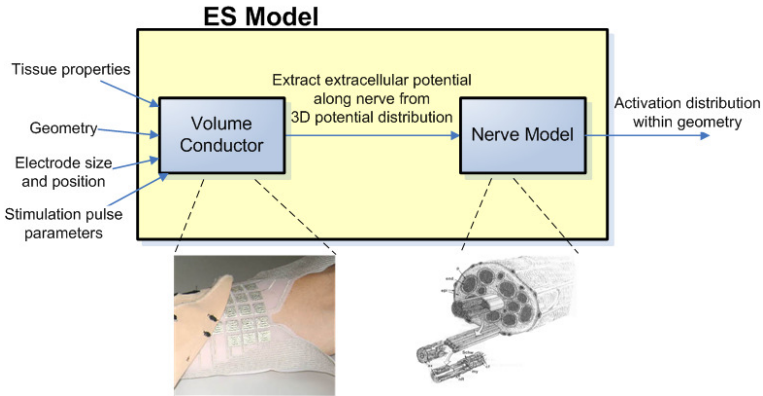


**Figure 1.2.** Two-step models are used to describe ES.

Several two step models were proposed to describe TES [HYL<sup>+</sup>98, MH90, LEM02, RMMR04, MRRM04]. However, these models exclu-

sively employed static models (i.e. neglecting capacitive effects) to describe the volume conductor, and linear nerve models to describe nerve activation. There are indications that a static volume conductor and the linear nerve models do not adequately capture the dynamics of the system:

**Volume conductor models** A crucial part of volume conductor models is the electrode-skin interface, which is responsible for the transmission of a stimulation pulse into the body. In [PWS94] it has been shown that the modeling of this system is possible using a finite element approach. However, a critical point in [PWS94] and others [Cob85, HYL<sup>+</sup>98, MSD<sup>+</sup>06, SMHR07] is that only static models have been used which neglect the time dependency of the current and potential field although the current and voltage are time dependent [DR99]. Dielectric parameters of the human tissue as published in [GLG96] therefore should be incorporated into the model in order to analyze the impact of the dynamics on nerve activation.

**Nerve models** Up to now non-linear nerve models, which can describe more facets of nerve activation [RACS98], such as anodic nerve blocking or the refractory period, were mainly used for implantable systems [LGD06, SS07] where the exciting electrodes are close to the nerve (near-field). However, it is not clear how these models expand to the far-field situation of TES.

The inhomogeneities of the human bulk tissues can be modeled to a certain resolution. Such approaches often use multiple layers or real magnetic resonance imaging (MRI) and computer tomography (CT) data to model the inhomogeneities. These techniques, however, have rarely [RBMR02, MSD<sup>+</sup>06] been applied for electrical stimulation. Examples where this technique was applied include electrical impedance tomography (EIT) [ZKI<sup>+</sup>02], Electrosurgery [NR03], and also Electromyography (EMG) [LSTK02]. The spatial arrangement of tissue layers and the different dielectric and resistive properties of these layers could have a significant effect on nerve activation, which needs to be taken into account in TES models.

Small structures (e.g., glands, pores) with different dielectric and resistive properties [PCWS93, PWS94] will also need to be incorporated into volume conductor models. For example pores or sweat glands in the skin layer have a lower resistivity with respect to the surrounding tissue and may act as tunnels for the current to penetrate deeper tissue layers. It was shown that these structures are important in models describing drug delivery through the skin [Gri84, CIK<sup>+</sup>98].

### 1.3. Objective and Contributions of this Thesis

Existing ES models were presented in the previous section. These models only describe the resistive property of the volume conductor and neglect the permittivities of the tissues. Hence, there are no transient models available that describe the time evolution of the potential distribution and the current density generated by TES inside the human tissues. In this thesis a TES model is presented that comprises a transient FE model and a nerve model in order to describe nerve activation. Such a model can quantify the influence of many parameters on nerve activation (e.g., capacitive effects, electrode-skin contact resistance, electrode material resistance, or nerve depth). This reveals the parameters with the largest influence in TES and allows to conclude which model simplifications can be made.

There exist no TES models that incorporate inhomogeneities like sweat pores, blood vessels, or other body inhomogeneities. It is possible that those structures could act as conductive tunnels and perturb the stimulation field and therefore have a large influence on ES. Specialized geometries were developed in order to analyze the effect of such inhomogeneities on TES.

Not only the inhomogeneities may influence TES, but also the complex arrangement of tissue layers. Models based on anatomical data (MRI, CT) are used to describe denervated muscle stimulation [RBMR02]. However, for neuromuscular stimulation the detailed anatomy is currently not incorporated in models. The TES model presented in this thesis incorporates a geometry that is based on MRI data. The goal is to investigate if such complex geometries are required to accurately describe TES or if geometric approximations (e.g. cylinder) are sufficient.

Array electrodes consisting of many single electrode pads that can be individually activated were developed [LKK04]. Up to now the design (element size, gap size, ...) of such electrodes was done by trial and error. New methods to assess the selectivity in TES models are presented that allow to optimize such array electrodes with the aim to improve efficacy and comfort of multichannel TES.

### 1.4. Outline of the Thesis

This thesis consists of four main parts. Part II introduces the developed TES model, part III focuses on investigations that are related to the



properties of human tissues, part IV discusses the influences of transcutaneous electrode designs, and part V summarizes the main conclusions of the thesis.

**TES Model (Part II)** Chapter 2 introduces the anatomical and electrical features that are relevant for the TES model. In chapter 3 the TES model that comprises a transient volume conductor model and a nerve model is presented as well as new post-processing methods that were developed to calculate the activation volume and the selectivity. Subsequently, in chapter 4 different aspects of the TES model are verified with experimental data. Often linear approximations of the non-linear nerve models are used due to the cheaper calculation and because certain postprocessing procedures could only be applied to data calculated with linear models. The accuracy of such linear nerve models was analyzed for implantable systems but not for TES what is undertaken in chapter 5.

**Tissue Properties (Part III)** In chapter 7 the TES model is used to analyze the influence of different tissue properties on nerve activation (resistivity, capacitance, inhomogeneities, layer thicknesses, ...). However, not only the macroscopic tissue properties can influence nerve activation but also the microscopic nerve bundles. In chapter 8 a specialized finite element model of a nerve bundle is used to calculate the influence of the complex tissue arrangement in nerve bundles on nerve activation. In chapter 9 the main influences are summarized and discussed.

**Electrode Properties (Part IV)** TES is applied using surface electrodes that are applied to the skin. The current distribution underneath electrodes can be non-uniform due to many reasons (edge effects, skin inhomogeneities, ...). It is hypothesized that electrodes with high resistivity can improve the homogeneity of the current density underneath the electrode. This hypothesis is treated in chapter 11. The size and the material of transcutaneous electrodes has an effect on the selectivity and the comfort of the stimulation. In chapter 12 the influence of the electrode material is quantified and the electrode sizes that optimize selectivity and comfort are determined. Thereafter array electrodes are treated in chapter 13. Up to now, designing array electrodes (gap size between single elements, material resistivity) has been done by trial and error. Using the TES model gap sizes and electrode materials were determined that enable to achieve efficient and comfortable stimulation.



**Part II**

**TES MODELING**



# 2

## Anatomy and Neurophysiology of the Human Forearm

This chapter begins with the anatomy of the human forearm and introduces the muscles that are responsible for finger flexion and extension. The second section examines the nerves that innervate these muscles and it is explained how electrically excitable membranes can generate action potentials (APs). Especially the case where such membranes are excited with extracellular stimulation using electrical currents is emphasized. This background is required to build a model that describes nerve activation in the human forearm during TES.

### 2.1. Anatomy

In Figure 2.1 an image of the profile of a human forearm is depicted. The main building blocks are two bones (ulna and radius), the muscles

which are connected with tendons to the bones, a fat layer, and a skin layer.

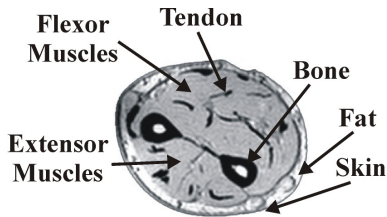


**Figure 2.1.** Profile of human forearm (MRI image).

The hand and finger flexors are the main muscle group dealt with throughout this thesis. The two muscle groups that are mainly responsible for finger extrinsic flexion movements in TES are the extrinsic muscle *m. flexor digitorum profundus* and the *m. flexor digitorum superficialis*. These extrinsic flexor muscles are located at the anterior side of the forearm (see Figure 2.2). A detailed description of all muscles in the forearm, together with their function, origin, insertion and innervation is given in the Appendix A.

## 2.2. Neuromuscular System

This section starts by introducing the motor units which are the connection between the muscles introduced in the previous section and the nerves described in this section. Such nerves (nerve bundles) are composed of many axons which transmit the actual information with APs through the body. AP flow is either from the brain or the spinal cord to the muscles (efferent or motor nerves) or from the body's sensory system to the spinal cord or the brain (afferent nerves). It will also be explained how externally applied currents influence axons and how APs can be generated.

### 2.2.1. Motor Units

A motor unit is a combination of one motor neuron and all the muscle fibers which it innervates (see Figure 2.3). Several motor units serve one muscle. When the motor neuron receives an AP it will transmit this on to the muscle which then contracts.

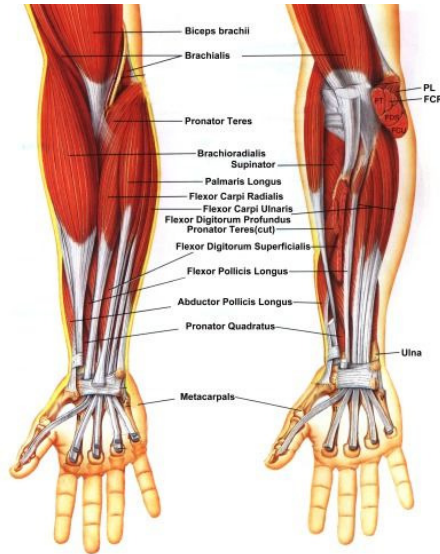


**Figure 2.2.** The muscles on the anterior side of the forearm. [Sta05]

Each AP can only generate a particular force regardless of the intensity of the stimulus [TMV99]. To increase the generated force either multiple motor units are recruited, or more APs are generated (frequency).

### 2.2.2. The Neuron

The main structures of the nervous system are neurons. A neuron has four main parts; the cell body, the axon, dendrites and presynaptic terminals [Sta05]. The cell body contains all the necessary structures for the cell to function. Dendrites extend from the cell body as short branches that act as signal receivers from other neurons. The axon transmits the signal (APs) to other neurons or directly to muscles. For faster conduction of the APs, axons are insulated with a myelin sheet which is interrupted at regular distances. These gaps are called "nodes of Ranvier". They cause a regeneration of the AP which ensures a fast propagation of the AP.

The underlying structure that allows axons to transmit APs is the

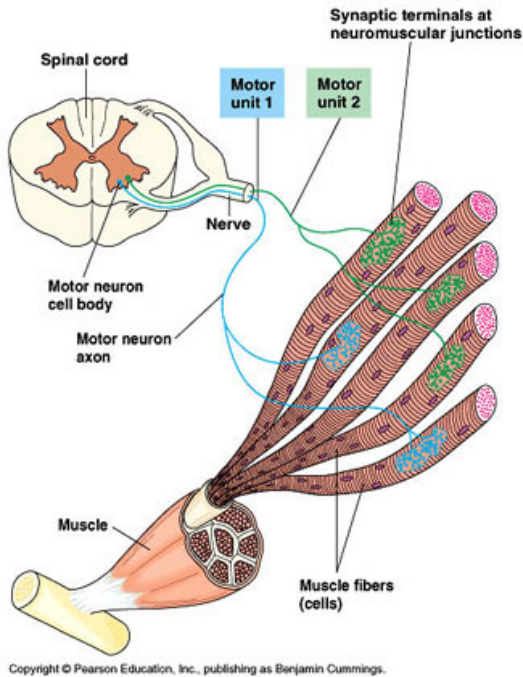


**Figure 2.3.** Two motor units [Sta05]

semipermeable cellular membrane [SD01]. This membrane regulates selectively the chemical exchange of certain ions from within the cell to its surrounding. The resulting ionic concentrations are determined by the concentrations of the ions in the fluids on both sides of the cell membrane and the ion transport proteins that are in the cell membrane. In most cells the resting TP has a negative value, which by convention means that there is excess negative charge inside compared to outside. The resting potential in human cells is around  $-70$  mV.

APs are all-or-none impulses with an amplitude of about 100 mV and a duration of about 1 ms. The speed of the AP propagating along the axon can be in the range of 1 - 100 m/s. An AP is evoked by a change in membrane selectivity and permeability of the ion channels. By changing its permeability to certain ions the resting TP of about  $-70$  mV can change and cause an AP. When an axon is depolarized



above the threshold of about  $-55\text{mV}$  an AP is generated (see Figure 2.4) [SD01]. Depolarization of the axon below this threshold does not generate an AP and the TP of the axon will return to the resting potential.

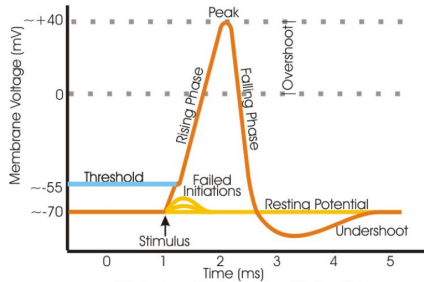


**Figure 2.4.** Schematic AP.

### 2.2.2.1. Nerve Fiber Types

The nervous system is built of axons which can be classified into type A and C fibers [RACS98]. The main difference is the speed with which they can conduct an AP.

*A-fibers* Type A-fibers are myelinated and have a large diameter. The diameter distribution of such type A axons in human nerve bundles is shown in Figure 2.5. They are able to conduct AP's at a speed of 15-120 m/s. Motor neurons that innervate skeletal muscles and sensory neurons mostly consist of A-fibers.  $A_\alpha$  and  $A_\beta$  fibers are mostly motor axons whereas the  $A_\delta$  fibers are mostly sensory axons. The axons that are activated with electrical stimulation are mainly the  $A_\alpha$  and the  $A_\beta$  fibers which show a bimodal distribution with peaks at  $6\ \mu\text{m}$  and  $12\ \mu\text{m}$  [RKd<sup>+</sup>96, PF07]. The  $A_\delta$  fibers are the thickest sensory fibers and therefore the first sensory fibers that are activated with TES.

*C-fibers* C-fibers are thinner (Figure 2.5) in diameter and not myelinated at all. They can conduct AP's with a speed of 2 m/s. These fibers are mainly used for the autonomous nervous system, the part of the nervous system that innervates the internal organs. They are needed to

keep these organs working in harmony with the rest of the body, but need not to be as fast as the reactions to the external environment.

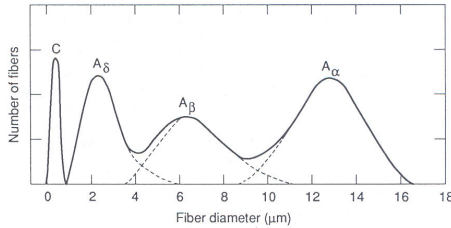


**Figure 2.5.** Diameter Distribution of axons in peripheral nerve bundles. (from [RACS98])

### 2.2.3. The Nerve Bundle

The axons that were discussed in the previous section are gathered in peripheral nerve bundles [Sta05]. Such nerve bundles contain several fascicles each of which contains many axons of different diameter (see Figure 2.6). Each fascicle is surrounded with a thin perineurial connective tissue layer and inside the fascicle the axons are embedded in connective tissues called endoneurium. The nerve bundle is surrounded by an encapsulating layer that is similar to the perineurial connective tissue [RACS98].

### 2.2.4. Extracellular Stimulation of Axons

As described in section 2.2.2, APs in axons are generated by electrochemical reactions in the brain or the spinal cord. However, it is also possible to excite axons with electrical currents that are applied to the human body. In TES electrodes are placed on the skin as depicted in Figure 2.7 and a current is applied [TMV99]. The cathode is placed on so called motor points that are shown in Figure 2.8 for the human arm. These are points where the nerves are close to the skin surface and can be activated with minimal current. With such an arrangement it is possible to selectively activate specific nerves and muscles. The electrical current that is applied between the electrodes is either voltage or current regulated (see also section 3.1.2) and most often of rectangular

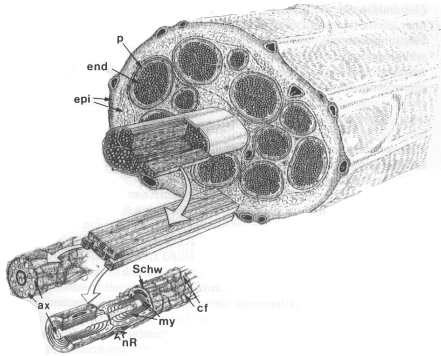


**Figure 2.6.** Microanatomy of a peripheral nerve bundle. [RACS98].

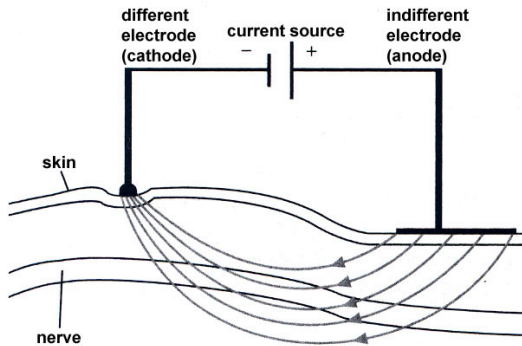


**Figure 2.7.** Electrodes are placed on the skin in order to generate APs in peripheral nerves using an electrical current. (from [TMV99])

shape (see Figure 2.9) [BMB<sup>+</sup>00]. These pulses have a certain pulse amplitude, pulse duration, rise time, and pulse repetition frequency. In order to reverse the modified charge distribution after the pulse a balancing pulse can be applied.

The applied pulse influences the TP of axons (Figure 2.10). Under the cathode the axon is depolarized (decreases TP) and under the anode the axon is hyperpolarized (increases TP). If the depolarization is large enough to drive the TP above about  $-55\text{ mV}$  an AP is generated.

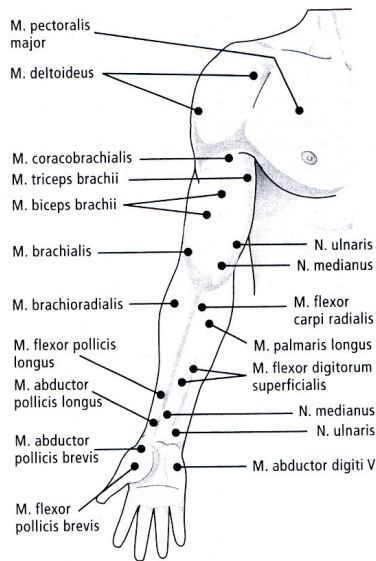


**Figure 2.8.** Motor points from which the specified nerves and muscle are excited using TES. (from [TMV99])

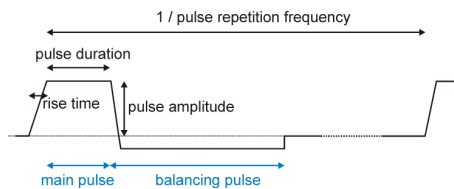


**Figure 2.9.** Rectangular current pulse that is commonly used in TES.

The smallest stimulation amplitude that is required to generate an AP is denoted motor threshold. The hyperpolarization under the anode drives the TP to lower values ( $< -70\text{mV}$ ) and suppresses the generation of APs. However, when the stimulation current is switched off the TP returns to its resting membrane potential of about  $-70\text{mV}$ . Such a relative depolarization can generate an AP if the hyperpolarization was large enough [TMV99]. A rule of thumb is that the current required for

an anodic stimulation is three times the current of a cathodic stimulation [Rat88].

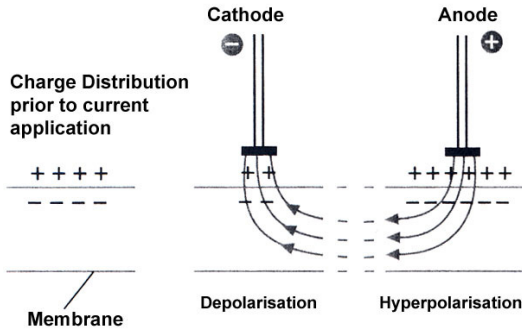


**Figure 2.10.** TP change of an axon using an extracellular electrical current. The cathode generates a depolarization and the anode a hyperpolarization. (from [TMV99])

#### 2.2.4.1. Generated Force and Recruitment

One of the goals in TES is to generate a certain muscle force in specific muscles. As described in section 2.2.3 muscles are innervated by nerve bundles that consist of many axons with different diameter (see Figure 2.5). With extracellular stimulation thicker axons are more depolarized than thinner axons. Furthermore, axons that are closer to the stimulation electrode are more depolarized because the current density is higher. Therefore, the thickest axons that are closest to the electrode are activated first (motor threshold). There are different alternatives to recruit more axons using TES (compare to Figure 2.9) [TMV99]:

- An increase of the *pulse amplitude* recruits thinner and more distant axons within nerve bundles and hence increases muscle force.
- The *pulse duration* can be increased which also recruits more axons and as a consequence increases muscle force.
- An increase of the *pulse repetition frequency*, does not recruit more axons, but it increases the frequency of APs in the activated axons and thus also increases the generated muscle force.

- A faster *rise time* of the rising edge of the rectangular pulse generates more APs. The underlying effect is that when the TP of an axon's membrane is changed from the resting membrane potential (e.g. due to extracellular stimulation) some gates for certain ions will open and try to drive the TP back to its resting potential. This opening of the membrane gates requires a certain amount of time. Hence shorter rise times leave the gates less time to counteract.

The term recruitment (REC) is used to describe the percentage of axons that are activated divided by all axons that innervate a certain muscle. 100% REC means that all motor units are activated and 0% means that no motor unit is activated.

### 2.2.5. Rheobase and Chronaxie

In order to check the excitability of nerves and muscles the chronaxie can be calculated [BMB<sup>+</sup>00]. To obtain the chronaxie first the rheobase is required. The rheobase is the smallest current amplitude of 'infinite' duration (practically, a few hundred milliseconds) that produces an activation. Chronaxie is the pulse duration required for motor threshold with an amplitude of two times the rheobase (see Figure 2.11). In humans the chronaxie is in the range of 0.05 msec to 1 msec. A prolongation of the chronaxie indicates a pathological process, e.g. a degeneration of the axons [Sta05].

A more complete picture of the excitability can be obtained by measuring motor thresholds for multiple pulse durations. From these data points a strength-duration curve can be drawn as depicted in Figure 2.11.

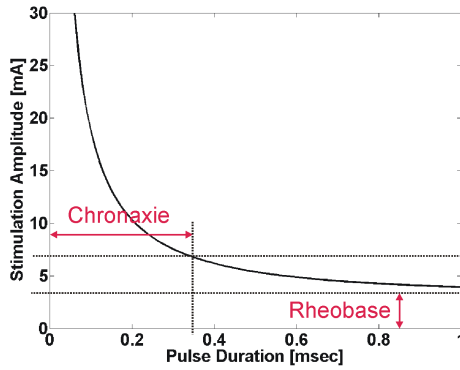


**Figure 2.11.** Strength-Duration curve with rheobase and chronaxie indicated.





# 3

## TES Model of the Forearm

Based on the knowledge of the anatomy and the neuromuscular system introduced in the previous chapter 2 and published literature (section 1.2) a TES model is derived. First, equations that describe electrical current flow and the potential distribution in biological tissues are presented (section 3.1). Then the TES model which is used for most simulations within this thesis is introduced (section 3.3). It consists of a FE model describing the potential distribution in the forearm (section 3.1.5) and a nerve model (section 3.2) that calculates a nerve activation distribution based on this potential distribution. FE models can have different levels of detail. A general model that includes the main tissue layers (skin, fat, muscle, bone) is introduced in section 3.1 and a model with small inhomogeneities (e.g. sweat ducts) is presented in section 3.1.5.4. The nerve activation distributions that is produced with the TES model can be analyzed with several techniques that are described in section 3.4.2. Figure 3.1 summarizes the different models and techniques that are presented in this chapter.

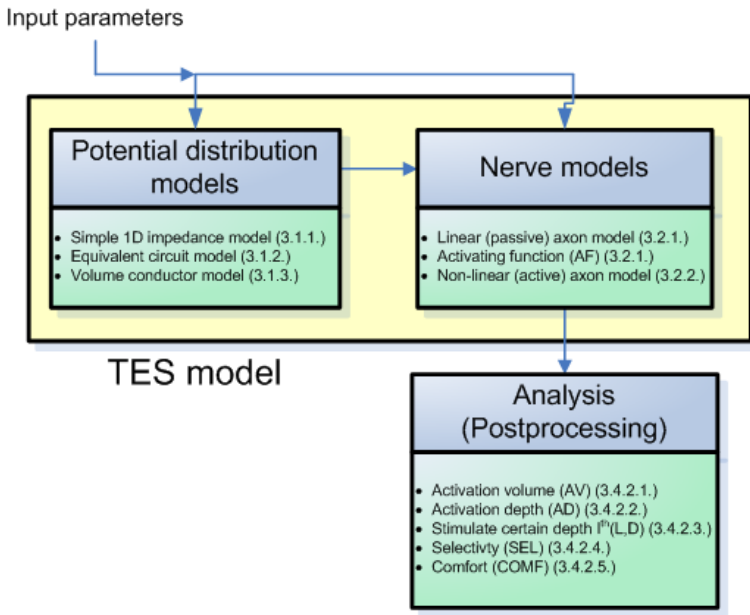


**Figure 3.1.** Graphical summary of the models and techniques that are introduced in this section.

### 3.1. Model of Electrical Potential Distribution in Human Tissues

This section introduces models that describe electrical current flow in biological tissues. It is known that the bulk impedance properties of biological tissues define the pathways of the current and the associated potential distribution for an applied stimulus [MH90]. The section starts with simple one dimensional models where current and voltage have only one direction (section 3.1.1) and ends with more complex volumetric models where current and voltage can have arbitrary directions (section 3.1.3). The introduced model equations for arbitrary directions of the current and voltage were solved using the FE technique (section 3.1.5). The reasons for choosing the FE technique are discussed in the same section.

### 3.1.1. Simple Impedance Model of Biological Tissues

In this section the simplest electrical model of biological tissues is presented. A tissue with homogeneous resistivity and permittivity is assumed. Figure 3.2 illustrates an arrangement where two electrodes of area  $A$  are used to contact a biological tissue with length  $d$ . Such an arrangement can be used to measure the resistive and capacitive properties of tissues. The current  $I$  flowing through the tissue is the sum of the conduction (resistive) current  $I_R$  and displacement (capacitive) current  $I_C$  (Equation (3.1)). The resistive conduction is carried by the mobility of ions within the biological tissue and the displacement current is due to polarization effects in the tissue [FS89]. For the case shown in Figure 3.2 where the current and voltage vectors are one dimensional (vectors are perpendicular to the electrode throughout the tissue) equation 3.2 describes the current  $I$  and the voltage  $V$  depending on the resistance  $R$  and the capacitance  $C$ . The resistance  $R$  is calculated using Equation (3.3) where  $\rho$  is the resistivity of the tissue. Often also the conductivity  $\sigma$  is used to describe the resistive property of tissue, which is the inverse of the resistivity (Equation (3.4)). The capacitance (Equation (3.5)) depends on the area  $A$ , the distance  $d$ , and the permittivity  $\epsilon = \epsilon_0 \epsilon_r$  that is a measure of a material's ability to become polarized in response to an applied electric field.

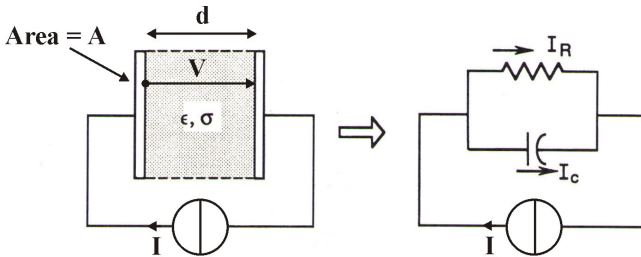


**Figure 3.2.** Simplified tissue model where voltage and current vectors are one dimensional. (adapted from [RACS98])

$$I = I_R + I_C \quad (3.1)$$

$$I = \frac{V}{R} + C \frac{dV}{dt} \quad (3.2)$$

$$R = \frac{\rho d}{A} = \frac{d}{\sigma A} \quad (3.3)$$

$$\rho = \frac{1}{\sigma} = \frac{RA}{d} \quad (3.4)$$

$$C = \frac{\varepsilon_0 \varepsilon_r A}{d} \quad (3.5)$$

While the illustration in Figure 3.2 indicates a simple method for measuring resistivity and permittivity, a more precise method is to use four electrodes. Two electrodes are used to supply the current or voltage and two electrodes are used to measure the voltage drop within the measured tissue [RA63]. As a consequence the measurement is not influenced by electrode polarization effects which are induced at the stimulating electrodes.

### 3.1.2. Equivalent Circuit Models

In the previous section biological tissue was modeled with one resistivity  $\rho$  and one permittivity  $\varepsilon$ . However, human tissues consist of different types and layers with different  $\rho$  and  $\varepsilon$  why such a model cannot describe the entire dynamics. A simple model that can be used to describe the dynamics of multiple tissues is an equivalent circuit model that uses multiple resistors and capacitors [YY81, Ede71]. An example of such a model is depicted in Figure 3.3. The hydrogel electrodes, which are mainly resistive are represented by a single resistor  $R_{elec}$ . The resistor  $R_{skin}$  and the parallel capacitor  $C_{skin}$  represent the resistivity and the capacitance of the skin. Evidence for this simple model of the skin was given in [Lyk71] where the voltage response of intact skin was compared with the response of skin with abraded stratum corneum. Fat and muscle are represented by the series resistor  $R_{body}$ . The polarization voltage and the interface resistance which are due to the contact of the electrode with the skin can be neglected in electrical stimulation [DR99]. At the electrodes either a voltage or current regulated source is connected as described in the following paragraph.

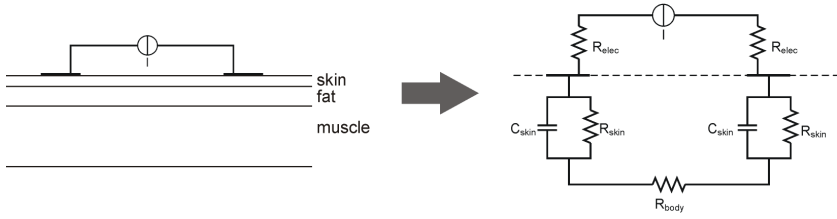


**Figure 3.3.** Equivalent circuit model of the main tissue layers.

**Voltage and Current Regulated Stimulation** Equivalent circuit models can be used to understand the basic effects when either a voltage or current regulated source is used in TES. Figure 3.4 shows the voltages and currents that are present at the different resistors and capacitors. The main advantage of current regulated stimulation is that, for example, contact resistance changes due to different moisture on the skin do not influence nerve activation [KK06]. This is visualized in Figure 3.4 where the voltage drop  $V_{body}$  within the resistive tissues remains constant when  $R_{skin}$  is changed. This indicates that the potential drops along nerves will remain constant. In voltage regulated stimulation the impedance ( $R_{skin}$ ) directly influences nerve activation. This is a major disadvantage and necessitates that the stimulation amplitude has to be adapted when the electrode contact changes due to the sweating of a patient.

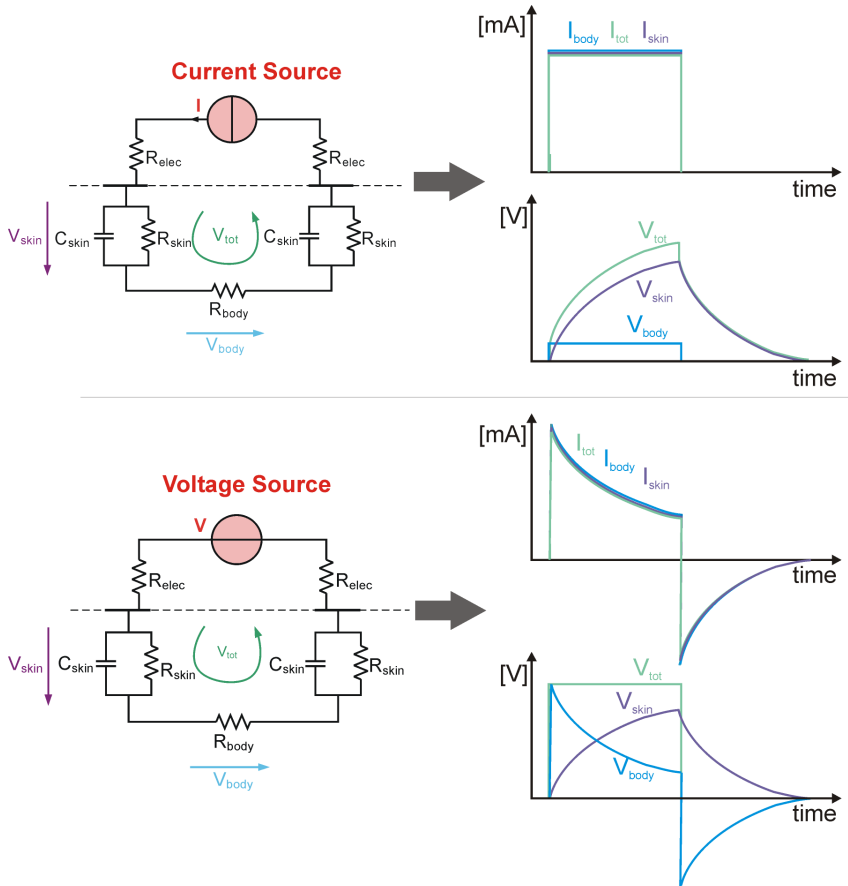


**Figure 3.4.** Simple equivalent circuit model of TES for current (upper sketch) and voltage regulated pulses (bottom sketch). The plots on the right hand side depict the current and voltage drops over the skin and body tissues (fat and muscle) for a rectangular current (upper) or voltage pulse (bottom).  $R_{elec}$  is assumed to be small compared to the other resistivities.

### 3.1.3. General Equations to Describe Static and Transient Potential Distributions in Volume Conductors

The two previous sections introduced two simple approaches for a coarse approximation of the voltages and currents that are present in human tissues. However, these models cannot calculate the potential and current distribution within complex geometries. In this section equations that calculate the current and voltage vectors for arbitrary directions within a volume conductor are introduced. The current flowing through the electrodes and the bulk tissues has a resistive and capacitive part (section 3.1.1) which can be described with Maxwell's equations (3.6)-(3.9). The time-derivative of the magnetic flux density can be neglected in human tissues [PH67], which reduces Maxwell's equations to the quasistatic approximation (3.10)-(3.13). The electric field described by Equation (3.11) is irrotational and can be described by equation (3.14) where  $V$  is the electric scalar potential. In the case of time-varying quasistatic electromagnetic fields governed by Maxwell's equations (3.10)-(3.13), the electric and magnetic fields are uncoupled. In other words the wave propagation and inductive effects in the medium are neglected [PH67]. Additionally, for TES, only the electric solution is of interest, therefore, the equations can be simplified using the continuity equation (3.15). This yields the differential equation (3.16) describing the transient electric scalar potential  $V$  in a volume conductor. This equation takes into account the resistive ( $\sigma = 1/\rho$ ) and the dielectric properties ( $\varepsilon = \varepsilon_0\varepsilon_r$ ) of the tissues. The static version of equation (3.16) is the Laplace equation given in equation (3.17).

$$\nabla \times \mathbf{H} = \mathbf{J} + \frac{\partial \mathbf{D}}{\partial t} \quad (3.6)$$

$$\nabla \times \mathbf{E} = \frac{\partial \mathbf{B}}{\partial t} \quad (3.7)$$

$$\nabla \mathbf{B} = 0 \quad (3.8)$$

$$\nabla \mathbf{D} = \rho \quad (3.9)$$

$$\nabla \times \mathbf{H} = \mathbf{J} + \frac{\partial \mathbf{D}}{\partial t} \quad (3.10)$$

$$\nabla \times \mathbf{E} = 0 \quad (3.11)$$

$$\nabla \mathbf{B} = 0 \quad (3.12)$$

$$\nabla \mathbf{D} = \rho \quad (3.13)$$

$$\mathbf{E} = -\nabla V \quad (3.14)$$

$$\nabla \left[ \mathbf{J} + \frac{\partial \mathbf{D}}{\partial t} \right] = 0 \quad (3.15)$$

$$-\nabla \cdot ([\sigma] \nabla V) - \nabla \cdot ([\varepsilon] \nabla \frac{\partial V}{\partial t}) = 0 \quad (3.16)$$

$$-\nabla \cdot ([\sigma] \nabla V) = 0 \quad (3.17)$$

### 3.1.4. Different Approaches to Calculate Electrical Potential Distribution within Biological Tissues

In the previous section 3.1.3 the equations that describe electrical potentials within human tissues were derived (Equations (3.16) and (3.17)). In this section an overview of the different approaches that can be used to solve these equations is presented and it is justified why the FE technique was used in this thesis.

Table 3.1 gives a summary of the different approaches that are discussed in the following. The requirements that were compared are whether the model can describe transient electrical potentials or only static ones, whether detailed geometries can be used, whether it is possible to add inhomogeneities, and whether the computational speed is satisfactory.

Analytical approaches have the advantage that calculation costs are cheap and that closed form solutions often exist [LEM00, LEM01, LEM02, TNK07]. A disadvantage of analytical approaches is that no detailed geometries (i.e. MRI segmentation) or small inhomogeneities (e.g. sweat ducts) can be included. Models consisting of large resistor and capacitor networks have also the disadvantage that small structures cannot be included. Finite difference time domain (FDTD) models allow including small inhomogeneities and detailed human physiology [www]. However, FDTD simulations are too slow at low frequencies that are required for TES (1 kHz). A rule of thumb for FDTD simulations is that the smallest geometric structure in the model should not be smaller than  $\frac{\lambda}{10}$ , with  $\lambda$  the wavelength in the medium. This yields  $\frac{\lambda}{10} = \frac{c}{f * n * 10} = \frac{3e8}{1e3 * 1.33 * 10} = 23 \text{ km}$  which is significantly larger than a human arm. The Transmission Line Method (TLM) which was used in [RBMR02] uses a mesh of equally sized rectangular cubes. This



has the disadvantage that a large number of elements is required when small structures are modeled. In FE models mixed size tetrahedral elements allow small and large structures in the same model [MH90]. FE models can cope with detailed geometries and can describe systems at low frequencies over time. For these reasons the potential distribution in a human forearm was described using a finite element time domain (FETD) model that is introduced in the following section. The trade-off are the computational costs of FE models that can be expensive for detailed models.

Model	Transient	Detailed Geometries	Inhomogeneities	Computational Speed
Analytical	+	-	-	+
RC network	+	-	-	+
Finite Difference Time Domain	+	+	+	-
Transmission Line Method	-	+	+	-
Finite Element Method	+	+	+	-

**Table 3.1.** Summarizes the main advantages and disadvantages of the different modeling techniques that can be used to describe electrical potential distributions within volume conductors. The requirements are marked with (+) if fulfilled or with (-) if not fulfilled.

### 3.1.5. FE Model

#### 3.1.5.1. Model Geometry

The geometry of the bulk tissues of the forearm can be modeled with different levels of detail. A detailed geometry using a segmentation of MRI scans and a coarse geometrical representation using multiple concentric cylinders were built (see Figure 3.5). The segmentation procedure to obtain the detailed geometry is described in section 7.3.

The cylindrical geometry was constructed using the standard CAD software package SolidWorks (SolidWorks Corporation, Concord, MA USA). The material types that are considered in the model are: electrode substrate, electrode-skin interface, skin, fat, muscle, and bone. The thicknesses of the layers in the cylindrical model are summarized in Table 3.2. The thicknesses are in a range that covers most human forearms [Sta05, RACS98, Val01]. How well the cylindrical model describes the complex composition of tissues in a human arm will be analyzed in more detail in section 7.3.

The human lower arm was modelled as a body with a finite length. If the cylinder were too short, errors would be introduced in the simula-

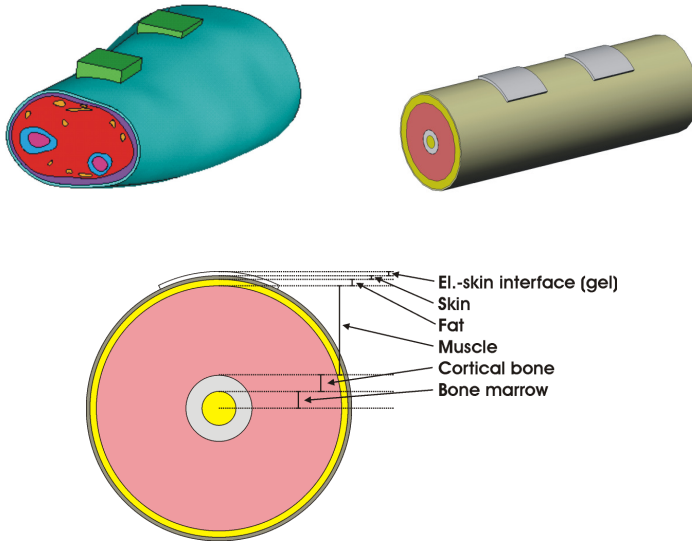


**Figure 3.5.** Top-Left: Detailed geometry using MRI segmentation techniques. Top-Right: Cylindrical geometry. Bottom: Cylindrical geometry with thickness definitions.

Material	Min [mm]	Standard [mm]	Max [mm]
El.-skin interface	0.5	1	2
Skin	1	1.5	3
Fat	2	2.5	30
Muscle	20	33.5	60
Cortical bone	4	6	8
Bone marrow	4	6.5	8

**Table 3.2.** Thicknesses of the different tissue layers used in the cylindrical geometry (compare with Figure 3.5). Columns Min and Max are extreme values that can be expected in practical applications. ([Sta05, RACS98, Val01])

tion result. Thus the model length was chosen such that no significant change of the electrical scalar potential was found for further elongations (an error of 1% was accepted).

In TES surface electrodes of different shapes are used to deliver currents into the human body. In this thesis single, square electrodes with different edge length and array electrodes were investigated. The

electrode model consisted of a good conducting substrate (conductive carbon rubber) and an electrode-skin interface (hydrogel) as proposed in [PWS94]. The physical electrodes (e.g., Compex electrodes) are contacted by many thin wires which are bonded onto the substrate. In the FE model this was modeled by coupling the degrees of freedom of the electrode substrate surface. This means that all potentials on the whole area of the top side of the electrode were forced to the same electrical potential value.

### 3.1.5.2. Element Types

The detailed and cylindrical geometries (see section 3.1.5.1) were meshed with tetrahedral FEs and the electrical potentials were calculated using the finite element time domain solver of the FEM package Ansys (EMAG, Ansys Inc., Canonsburg, PA). The element type of the tetrahedral FEs in Ansys was SOLID232. This element can be used to solve both the transient or the static solution (Equations (3.16) or (3.17)). The mesh-size was always refined until no significant change ( $< 1\%$ ) was found in the resulting potential distribution.

Current regulated rectangular pulses (Figure 2.9) were applied to the electrodes using the independent constant current source (element Type CIRCU124) in Ansys. The current source was connected to the substrate (top surface) of the electrode.

### 3.1.5.3. Tissue Properties

The resistive and capacitive properties that were used for the different tissues and electrodes are given in Table 3.3. The range of values that is shown in Table 3.3 covers the range of values that can be expected in practical applications of TES [GLG96, RACS98, FS89, PF86]. The anisotropy of the muscles' resistivity and the permittivity was considered with a factor of three (between axial and radial direction  $3 * \rho_{axial} = \rho_{radial}$ ) [RACS98].

The resistivity of the skin is non-linearly depending on the current density [YY81, vB77, DR99]. This non-linearity and its effect on nerve activation will be investigated in more detail in section 7.2.1.

		Min	Standard	Max
Electrode interface	$\rho$ [ $\Omega m$ ]	1	300	10000
	$\epsilon_r$	1	1	2000000
Skin	$\rho$ [ $\Omega m$ ]	500	700	6000
	$\epsilon_r$	1000	6000	30000
Fat	$\rho$ [ $\Omega m$ ]	10	33	600
	$\epsilon_r$	1500	25000	50000
Muscle (axial)	$\rho$ [ $\Omega m$ ]	2	3	5
	$\epsilon_r$	100000	120000	2500000
Muscle (radial)	$\rho$ [ $\Omega m$ ]	6	9	15
	$\epsilon_r$	33000	40000	830000
Cortical bone	$\rho$ [ $\Omega m$ ]	40	50	60
	$\epsilon_r$	2400	3000	3600
Bone Marrow	$\rho$ [ $\Omega m$ ]	10	12.5	15
	$\epsilon_r$	8000	10000	12000

**Table 3.3.** Resistivities and relative permittivities of different tissues. Columns "Min" and "Max" are extreme permittivity values from [GLG96, RACS98, FS89, PF86]. The column "Standard" contains properties used in an FE model that was verified with experimental measurements (section 4.2) [KK05].

#### 3.1.5.4. Potential Distribution in Inhomogeneous Tissues (Small Structures)

Tissue inhomogeneities like glands and sweat ducts can influence the potential distribution produced by TES. The size of such inhomogeneities can be as small as a couple of  $\mu m$ . The integration of such structures into the FE models that were introduced in section 3.1 is difficult. These inhomogeneities are about a factor of 1000 smaller than normal tissue layers introduced in Table 3.2. Small structures in FE models require many finite elements to accurately describe the potential distribution. As a consequence the computational complexity increases dramatically so that such problems can't be solved in reasonable time. One solution to reduce the number of finite elements is to build simplified geometries that only describe the region of interest (e.g. 1 cm cube of skin and fat to investigate the influence of glands in the skin layer). Two types of inhomogeneities were investigated: Inhomogeneities introduced by nerve bundles are investigated in section 8 using a special purpose geometry shown in Figure 8.1, and electrode and skin inhomogeneities are investigated with a multiple layer cube in section 11.

## 3.2. Excitation Models (Axon Models)

Activation of excitable tissues using extracellular ES in humans was described in section 2.2.4. Excitation models that describe the TP of axons when exposed to extracellular potentials were developed in order to better understand the influences of variations of the stimulation waveforms or of the electrode arrangement. This section begins with linear models and proceeds to more complex non-linear models.

### 3.2.1. Linear Axon Models

#### 3.2.1.1. Linear Cable Models

The electrical cable theory, which was originated in 1876 by Heaviside to analyze the first trans-atlantic telegraphy cable, can be employed to analyze the excitation of myelinated axons [JNT83]. The original cable models are linear and can only describe the capacitive behavior of the axon membrane but do not describe the generation of APs. Such models are referred to as linear cable models or passive cable models. However, it is possible to predict activation using these linear axon models what will be discussed in section 3.4.1 and chapter 5.

A myelinated axon can be modeled using the cable equation [McN76] (3.18) where  $V_{TP}$  is the TP and  $V_e$  is the extracellular potential.  $\tau_m$  denotes the membrane time constant and  $\lambda$  is the membrane space constant with  $\varrho_m$  the membrane resistivity (3.19). A spatial approximation of Equation (3.18) leads to Equation (3.20) which is the mathematical description of the equivalent circuit given in Figure 3.6. The discrete form (3.20) is derived from the continuous form (3.18) by using the approximations given in Equation (3.21). In the discrete form  $V_{e,n}$  denotes the potential at the nodes of Ranvier, which are the unmyelinated parts of an axon that are in contact with the extracellular potential. Further, the material parameters have to be substituted by (3.22), where  $d$  is the fiber diameter,  $\Delta x$  is the longitudinal increment,  $G_a$  is the axoplasm conductance,  $C_m$  is the membrane capacitance, and  $G_m$  is the membrane conductance.

$$\tau_m \frac{\partial V_{TP}}{\partial t} - \lambda^2 \frac{\partial^2 V_{TP}}{\partial x^2} + V_{TP} = \lambda^2 \frac{\partial^2 V_e}{\partial x^2} \quad (3.18)$$

$$\begin{aligned} \tau_m &= c_m / g_m \\ \lambda &= (r_m / r_i)^{1/2} = (d \varrho_m / (4 \varrho_i))^{1/2} \\ V_{TP} &= I_{i,n} / G_m \end{aligned} \quad (3.19)$$

$$\frac{dV_{TP,n}(t)}{dt} = \frac{1}{C_m} [G_a(V_{TP,n-1}(t) - 2V_{TP,n}(t) + V_{TP,n+1}(t) + V_{e,n-1}(t) - 2V_{e,n}(t) + V_{e,n+1}(t)) - I_{i,n}(t)] \quad (3.20)$$

$$\begin{aligned} \partial^2 V_{TP} / \partial x^2 &\approx (V_{TP,n-1}(t) - 2V_{TP,n}(t) + V_{TP,n+1}(t)) / \Delta x^2 \\ \partial^2 V_e / \partial x^2 &\approx (V_{e,n-1}(t) - 2V_{e,n}(t) + V_{e,n+1}(t)) / \Delta x^2 \end{aligned} \quad (3.21)$$

$$\begin{aligned} C_m &= c_m \pi d \Delta x \\ G_a &= \pi d^2 / (4 \rho_i \Delta x) \\ G_m &= g_m \pi d \Delta x \end{aligned} \quad (3.22)$$

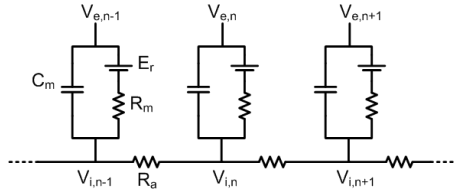


**Figure 3.6.** Electrical equivalent circuit of a myelinated axon (cable model).  $R_a$  is the axoplasm resistivity,  $C_m$  is the membrane capacitance, and  $R_m$  is the membrane resistivity, and  $E_r$  maintains the transmembrane resting potential.

### 3.2.1.2. Activating Function (AF)

The TP of an axon is influenced by the extracellular potential  $V_e(t)$  (equation (3.18)). More precisely it is the second spatial derivative of the extracellular potential  $\lambda^2 \frac{\partial^2 V_e}{\partial x^2}$  that drives the TP. Rattay et al. have introduced the term AF for this second spatial derivative of the extracellular potential along a given axon. This very simple calculation of the AF does not require nerve properties and can be used to predict AP generation [Rat88] with certain limitations that are discussed in detail in chapter 5.

### 3.2.2. Non-Linear Axon Models

#### 3.2.2.1. Membrane Equations

Hodgkin and Huxley (HH) [HH52] and later Frankenhaeuser and Huxley (FH) [FH64] introduced non-linear equations that describe the ionic current densities that flow through an unmyelinated axon membrane (section 2.2). The total ionic current density was subdivided into sodium  $J_{Na}$ , potassium  $J_K$ , nonspecific  $J_P$ , and leakage  $J_L$  currents (3.23). The individual current densities have the expressions given in equations (3.24) to (3.27) where  $V_{TP}$  is the TP. The values for the different parameters in equations (3.24) to (3.27) were published in [FH64, McN76, CRRS79, SMD87]. The variables  $m$ ,  $n$ ,  $h$ , and  $p$  are defined by the differential equations given in (3.28) to (3.30). The  $\alpha$  and  $\beta$  variables for the  $m$ ,  $n$ ,  $h$ , and  $p$  rate terms have the form given in equation (3.31). The values for the constants  $a$ ,  $b$ ,  $c$ , and  $d$  of this equation are given in [FH64].

$$J = J_{Na} + J_K + J_L + J_P \quad (3.23)$$

$$J_{Na} = \bar{P}_{Na} h m^2 \left( \frac{EF^2}{RT} \right) \frac{[Na]_0 - [Na]_i \exp(EF/RT)}{1 - \exp(EF/RT)} \quad (3.24)$$

$$J_K = \bar{P}_K n^2 \left( \frac{EF^2}{RT} \right) \frac{[K]_0 - [K]_i \exp(EF/RT)}{1 - \exp(EF/RT)} \quad (3.25)$$

$$J_P = \bar{P}_P p^2 \left( \frac{EF^2}{RT} \right) \frac{[Na]_0 - [Na]_i \exp(EF/RT)}{1 - \exp(EF/RT)} \quad (3.26)$$

$$J_L = g_L (V_{TP} - V_L) \quad (3.27)$$

$$\frac{dn}{dt} = \alpha_n (1 - n) - \beta_n n \quad (3.28)$$

$$\frac{dm}{dt} = \alpha_m (1 - m) - \beta_m m \quad (3.29)$$

$$\frac{dh}{dt} = \alpha_h (1 - h) - \beta_h h \quad (3.30)$$

$$\alpha_m, \beta_m, \text{etc.} = a(V_{TP} - b) \left[ 1 - \exp \left( \frac{V_{TP} - c}{d} \right) \right]^{-1} \quad (3.31)$$

### 3.2.2.2. Non-Linear Cable Model

McNeal [McN76] combined the linear cable model (equation (3.20)) with the non-linear membrane equations described in the previous section by adding the non-linear mechanisms to the nodes of the linear cable model. The current  $I_{i,n}$  in equation (3.20) was replaced with the ionic currents from equation (3.32).

$$I_{i,n} = \begin{cases} G_m V_{TP,n} & (linear) \\ \pi dW(J_{Na} + J_K + J_L + J_P) & (non-linear) \end{cases} \quad (3.32)$$

This type of model is usually referred to as non-linear cable model or active cable model. It was constantly improved by several groups to better describe the activation of human axons. The non-linear equations and the corresponding parameters which were first developed for amphibians were adapted to get a response that resembles mammalian nerve fibres [CRRS79, SMD87]. More details on the different versions of non-linear cable models are provided in the following section where different non-linear and linear cable models were combined with the FE model introduced in section 3.1.5.

## 3.3. TES model (Combined FE and Axon Model)

The aim of the TES model that is introduced in this section is to calculate nerve activation in a volume conductor. For this purpose the FE model from section 3.1.5 that calculates the potential distribution within a volume conductor representing a forearm with electrodes is combined with axon models (section 3.2). Such models are usually referred to as two step models (as introduced in section 1.2). In humans multiple axons with different diameters form nerve bundles (section 2.2.3). Multiple nerve bundles innervate muscles and these nerve bundles lie in different depth within the body [Sta05]. Therefore, the axon models were joined to multiple nerve bundles that are placed at desired locations within the volume conductor (Figure 3.7). In this thesis the depth of the nerves and axons is consistently defined as the distance from the fat-muscle interface to the nerve or axon (see Figure 3.7). The electric potentials in the volume conductor are interpolated along the axon and applied to the axon model in order to calculate the TP. The time dependent, spatially interpolated potentials from



the FE model  $V(x, y, z, t)$  (equation (3.16)) are linked to the corresponding extracellular potentials (equation (3.20)) of the axon model  $V_{e,n}(t) = V(x, y, z, t)$ . The coordinates  $x, y, z$  denote the interpolation location in the FE model that corresponds to the node  $n$  of the axon model (equation 3.20). The resulting TPs at every node of the axon models at the end of the applied current pulse are stored yielding the 3D activation distribution. From this 3D activation distribution further quantitative analysis can be performed (section 3.4.2).

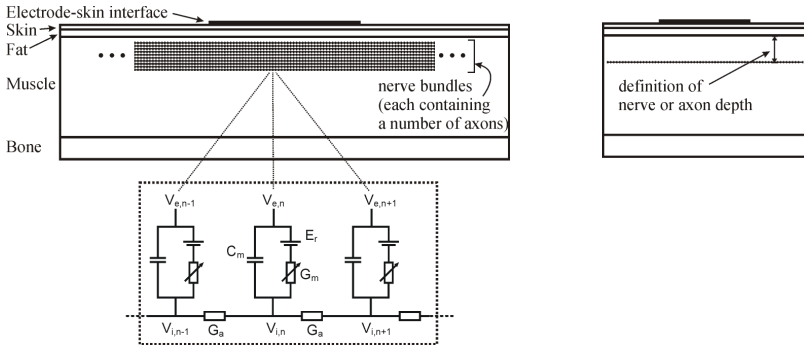


**Figure 3.7.** Left: Schematic representation of the combined model (TES model) consisting of a volume conductor (FE model) and nerve bundles at different depths. On the bottom the electrical equivalent circuit of a non-linear myelinated axon is shown. Right: Definition of nerve or axon depth is depicted (distance from fat-muscle interface to nerve or axon).

A summary of the axon models that were combined with the FE model is given in Table 3.4 and the underlying equations were introduced in the previous section 3.2.2. These axon models were chosen to cover different axon model structures (mono-domain, double-cable) and a wide range of chronaxie values [Zie01] (published chronaxie values are given in Table 4.1). Up to now such myelinated axon models were mainly used for implantable systems [LGD06, CCD01, SS07] where the exciting electrodes are close to the nerve (near-field). To address if these nerve models can also be used to model TES (far-field), a combined TES model that comprises a transient volume conductor and different axon models was developed (results are presented in section 4.2). Models A and B are based on the FH membrane [FH64] that describe sodium, potassium, and leakage membrane currents [McN76]

of the nodes of Ranvier. Model C is the CRRSS model (CRRSS stands for its authors' names) that only incorporates sodium and leakage currents at the nodes of Ranvier. The CRRSS membrane is similar to the HH membrane [HH52] but without potassium channels because they were found to be less important in the excitation process of myelinated mammalian nerves [SMD87]. Model D (MRG model) is the most recent axon model incorporating a double cable structure that not only describes the membrane currents at the nodes of Ranvier but also at the paranodal and internodal sections [MRG02]. Model  $D^P$  is the linear (passive) equivalent of axon model  $D$  where the non-linear membrane equations were replaced with the linear ones (equation (3.32)).

Models  $A$ ,  $B$ ,  $C$ , and  $AF$  were implemented in MATLAB (The Mathworks Inc., Natick, MA) and Model  $D$  and  $D^P$  in NEURON (Yale University School of Medicine, New Haven, USA). A custom software package to manage FE simulations, axon model simulations, and the postprocessing was developed (Appendix B).

Axon Model ID	Axon Model Name	Reference
$A$	Non-linear Cable Model (FH)	[McN76]
$B$	Non-linear Cable Temperature Compensated (FH)	[Rat90]
$C$	Non-linear Mammalian Nerve Model (CRRSS)	[CRRS79, SMD87]
$D$	Non-linear Double Cable Model (MRG model)	[MRG02]
$D^P$	Linear Double Cable Model (MRG model)	[MRG02]
$AF$	Activating Function (second derivative)	[Rat88]

**Table 3.4.** Different axon models used in the TES model.

### 3.4. Analysis (Postprocessing) using the TES model

The output of the TES model introduced in the previous section 3.3 is an activation distribution within the specified volume conductor. In this section the main types of analysis (postprocessing) that are performed on this activation distribution are introduced. First, the concept of AP prediction, which in literature is usually denoted as threshold prediction, is discussed. AP prediction uses linear axon models in order to predict APs. Afterwards, in section 3.4.2, the spatial analysis procedures that quantify the depth and the selectivity in TES models are introduced. These are the basic methods that will be used at different places in this thesis.

### 3.4.1. AP Prediction using Linear Axon Models

In section 3.2.1.1 it was mentioned that linear cable models only describe the capacitive properties of an axon and do not describe the generation of APs. However, it is possible to predict APs using linear axon models as shown in various studies [Rat90, WGD92, MMG04]. The benefits are the cheaper computational costs of linear models, that the superposition principle is applicable [RACS98], and the ability to invert the model [MMG04] (i.e. the stimuli can be designed based explicitly upon the desired output).

A method to predict APs using linear axon models was discussed in detail in [WGD92, MMG04] and is briefly reviewed for completeness.

In a TES model containing a non-linear cable model, threshold amplitudes (lowest current that generated an AP) that are denoted  $I^{th}$  for a specific axon are first identified (left plot in Figure 3.8).  $I^{th}$  can be determined using for example bisection search. The amplitude  $I^{th}$  is then applied to a TES model containing a linear axon model that is located at the same location as the non-linear axon model. The voltage of the TP reached in the linear nerve model at the end of the stimulation pulse is denoted  $V_{TP}^{th}(I^{th})$  (right chart in Figure 3.8). (In [MMG04] the threshold voltage  $V_{TP}^{th}$  is denoted critical voltage  $V_c$ .) The threshold  $V_{TP}^{th}(I^{th})$  can then be used in order to decide if an AP is generated or not. In axons where  $V_{TP} < V_{TP}^{th}$  no AP is predicted and in axons where  $V_{TP} \geq V_{TP}^{th}$  an AP is predicted.

A second possibility to predict APs is to use the AF instead of linear axon models. The calculation of the prediction threshold that is denoted  $AF^{th}(I^{th})$  can be done equivalent to the calculation of  $V_{TP}^{th}(I^{th})$ . Instead of calculating the TP using the linear axon model the AF (second derivative) is calculated.

The prediction thresholds  $V_{TP}^{th}$  and  $AF^{th}$  are not constant, rather they are a function of different parameters (electrode size, nerve depth, pulse duration, and axon diameter). The errors that occur when linear nerve models are used to predict the generation of APs are discussed in [WGD92, MMG04] for implantable stimulation systems. It was shown that errors due to different electrode sizes and nerve depths can be neglected but that lookup tables are required for changing pulse durations and axon diameters [WGD92, MMG04]. In chapter 5 simulation results for TES are presented that allow the same conclusion. The lookup tables for the thresholds  $V_{TP}^{th}$  and  $AF^{th}$  for different pulse durations and axon diameters are depicted in Tables 3.5 and 3.6. These Tables can be

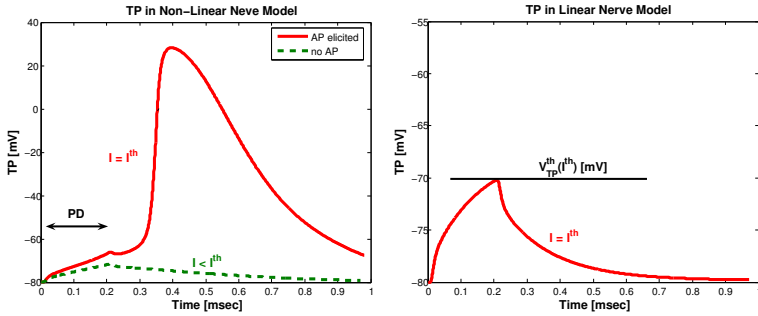


**Figure 3.8.** Determine activation threshold  $V_{TP}^{th}(I^{th})$  in linear nerve model.

used to predict APs using linear models in TES.

### 3.4.2. Spatial Description of Nerve Activation

In a computer model for deep brain stimulation Butson [BM06] introduced the volume of tissue activated in order to spatially describe the region where neural tissue was activated. The volume of tissue activated was defined by a 3D surface that encompasses the volume where the AF (second spatial derivative) was above a certain threshold. The volume of tissue activated allowed optimization of the stimulation parameters such that only the targeted region of the brain was activated. In this thesis the same concept of describing spatial activation with a volume is used. However, instead of volume of tissue activated we use the term activation volume (AV) because in TES not the whole region enclosed by the activation volume contains excitable tissue. In this section quantitative measures calculated from activation volumes that can estimate the activation depth and the selectivity in TES are introduced. These quantitative measures facilitate investigations of the size and shape of activation volumes for different current amplitudes, pulse durations, electrode sizes, and fat thicknesses.

The activation volumes and quantitative measures were calculated within a custom postprocessing module that was developed for Paraview and VTK (Kitware Inc., NY). This module was integrated in ArmSIMP (Appendix B). ParaView is an open source, freely available program for parallel, interactive, scientific visualization. The Visualization Toolkit (VTK) is an open source, freely available software system

$V_{TP}^{th}$		Pulse Duration [msec]					
		0.1	0.2	0.3	0.5	1	2
Axon $\varnothing$ [ $\mu\text{m}$ ]	4	2.2	0.9	0.8	0.2	-21.1	-32.7
	6	0.2	-27.6	-41.6	-52.6	-60.5	-64.1
	8	-39.5	-57.4	-63.3	-68.0	-71.3	-72.7
	10	-57.1	-67.3	-70.6	-73.3	-75.1	-75.8
	12	-63.9	-71.0	-73.4	-75.3	-76.6	-77.0
	14	-67.9	-73.3	-75.1	-76.5	-77.4	-77.8
	16	-70.9	-75.0	-76.3	-77.4	-78.1	-78.3

**Table 3.5.** Lookup table for the prediction thresholds  $V_{TP}^{th}$  that can be used to predict activation using a linear cable model. The values are given for different axon diameters and pulse durations. (The thresholds in this table were calculated using the linear MRG model as nerve model [MRG02]; model  $D^P$  in Table 3.4.)

$AF^{th}$		Pulse Duration [msec]					
		0.1	0.2	0.3	0.5	1	2
Axon $\varnothing$ [ $\mu\text{m}$ ]	4	36178	20424	15086	10836	7733	6212
	6	12388	6888	5048	3596	2558	2084
	8	5328	2973	2188	1573	1143	964
	10	3010	1674	1230	882	643	553
	12	2117	1177	864	619	453	394
	14	1588	881	646	462	336	294
	16	1190	661	484	347	254	223

**Table 3.6.** Lookup table for the prediction thresholds  $AF^{th}$  that can be used to predict activation using the AF. The values are given for different axon diameters and pulse durations. (The thresholds in this table were calculated using the second derivative [Rat88]; model  $AF$  in Table 3.4.)

for 3D computer graphics, image processing, and visualization used by thousands of researchers and developers around the world.

### 3.4.2.1. Activation Volume (AV)

The objective of activation volumes is to describe quantitatively the locations where axons of a certain diameter experience activation within a volume conductor. Activation volumes are constructed based on the 3D activation distribution that was calculated using the TES model (section 3.3). The activation volumes are defined with iso-surfaces that are generated with the iso-values  $V_{TP}^{th}$  or  $AF^{th}$  using for example the "marching cubes" algorithm [LC87]. The thresholds for different axon diameters and pulse durations are provided in Tables 3.5 and 3.6). Figures 3.9 and 3.10 show examples of activation volumes underneath the cathode in cylindrical arm models. For visual clarity the cover surface of the activation volume, which is the area between the fat and the muscle layer, is not drawn in Figures showing activation volumes.

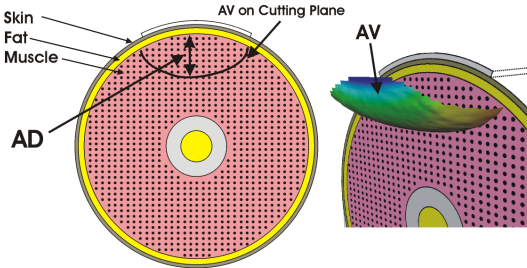


**Figure 3.9.** Cylindrical arm model. Each point drawn in the muscle represents a line on which the electrical potential was interpolated. The interpolated potentials are the input to the nerve models which calculate the activation distribution, from which the activation volumes are derived.

### 3.4.2.2. Activation Depth (AD)

The activation depth ( $AD$ ) is a measure to describe the depth of the activation in TES models. The activation depth is defined as the distance between two points on the normal vector centered underneath the stimulating electrode. One point is at the fat-muscle interface and the other one is the point where this normal vector intersects the activation

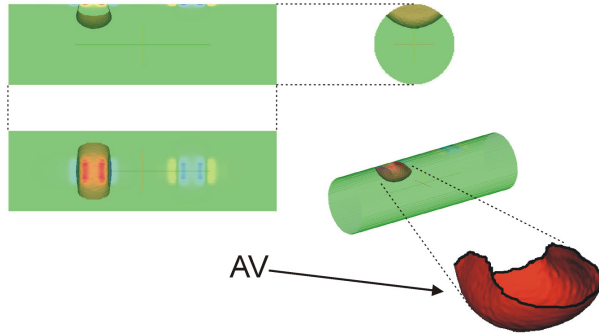


**Figure 3.10.** Cylindrical arm model with activation volume underneath cathode from different perspectives.

volume surface (see Figure 3.9). Note that the activation volume is calculated for a specific axon diameter and that therefore the activation depth is also calculated for a specific axon diameter.

### 3.4.2.3. Current to Stimulate in Certain Depth ( $I^{th}(L, D)$ )

The current amplitude that is required to activate an axon of a specific diameter in a certain depth was used as a measure to compare simulation results. This threshold current amplitude is denoted  $I^{th}(L, D)$ , where  $L$  is the target activation depth ( $AD$ ) and  $D$  is the axon diameter that is activated at threshold.

### 3.4.2.4. Selectivity ( $SEL$ )

The selectivity is understood as the ability to stimulate a specific nerve without stimulating adjacent nerves. In other words the activation volume encloses the target nerve but no other nerves. Because the exact positions of specific nerves are not exactly known, the shape and size of the activation volume ( $AV$ ) was investigated instead. As a measure for the selectivity ( $SEL$ ) the ratio between the activation depth ( $AD$ ) and the average breadth ( $\frac{V_{AV}}{AD}$ ) was used (see equation (3.33)). The average breadth was the ratio between the volume of the activation volume ( $V_{AV}$ ) and the activation depth. This yields for ( $SEL$ ) a ratio between the squared activation depth  $AD^2$  and the volume ( $V_{AV}$ ). A

deeper stimulation or a stimulation with a smaller activation volume increases the selectivity.

$$SEL = \frac{AD}{\frac{V_{AV}}{AD}} = \frac{AD^2}{V_{AV}}. \quad (3.33)$$

### 3.4.2.5. Comfort (*COMF*)

As proposed in [VvD06] pain is assumed to be proportional to the current density in the TES model. However, because pain is not perceived to be the same for different electrode sizes [AKH94], the current density has to be adapted with an additional factor  $\overline{ThP}_A$  to correct for different electrode sizes. The factor  $\overline{ThP}_A$  was derived from experimental measurements described in more detail in section 12.3.1.1. The measure for the estimated comfort is

$$COMF = \overline{ThP}_A / I \quad (3.34)$$

where  $I$  is the applied current amplitude and  $A$  indicates that the pain threshold changes for different electrode areas. The derivation of this equation is discussed in detail in section 12.3.1.2.

### 3.4.3. Limitations of the TES Models

- In all models only effects that are relevant for TES are considered, i.e. current levels above 0.1 mA and voltage levels that exceed 1 V. For the characterization of the body's response to microampere and millivolts the reader is directed to the work of Geddes [Ged72].
- The non-linear dependence of the bulk tissue properties to current density was neglected. This is not a major concern as it was shown that with current-regulated pulses the non-linear resistive properties of the bulk tissues can be neglected ([KKPM06], section 7.2.1).
- The direction of the nerves was always in axial direction of the arm model. Changing the direction of the nerve can influence nerve recruitment. More realistic nerve distributions could be integrated by changing the direction of the interpolation in the TES model.



- The comfort during TES is influenced by the choice of the electrode material (see section 12.2). This is not incorporated in the presented TES model. The comfort in the TES model was only calculated for hydrogel electrodes (see section 12.3).
- Electrochemical effects that occur at the electrode (hydrogel) skin interface are not considered. When using current regulated stimulation such effects mainly cause resistance and capacitance changes of the electrode-skin interface which have a minor influence on activation as shown in part III.



# 4

## Verification of the TES Model (Measurements)

In sections 1.2 and 3.3 a two step model that can be used to conclude from an applied current with surface electrodes on nerve activation is described. In section 4.1 the potential distribution calculated with the FE model (first step) is verified using measurements on human volunteers. Nerve activation of the TES model comprising the FE model and different axon models are then verified in sections 4.2 and 4.3 using motor threshold and force measurements.

### 4.1. Surface and Intramuscular Potentials

In this section the simulated potential distributions of the transient FE models are compared with experimental data taken from three human volunteers. An experimental validation of surface potentials that were

calculated using a transient FE model was also described in [LSDK04]. However, in that paper a sinusoidal source was used as excitation whereas here a current regulated pulse source as normally applied in TES was used. In addition to the surface potentials, the intramuscular potentials are measured with needle electrodes and compared with the FE model.

### 4.1.1. Methods

#### 4.1.1.1. FE Model

The parameters that were used for the FE model that was introduced in section 3.1.5 are summarized in the tree structure below.

FE model	
	Geometry .....cylindrical geometry (Figure 4.1)
	Tissue thicknesses .....standard values from Table 3.2
	Tissue properties .....standard values from Table 3.3
	Electrode type ..... single electrodes
	Electrode sizes ..... $5 \times 5 \text{ cm}^2$
	Electrode distance ..... 6 cm
	Equation ..... transient equation (3.16)
	Stimulation pulse ..... monopolar current regulated
	Amplitude ..... 9 mA
	Duration ..... $0.1 \text{ ms} - 1 \text{ ms}$

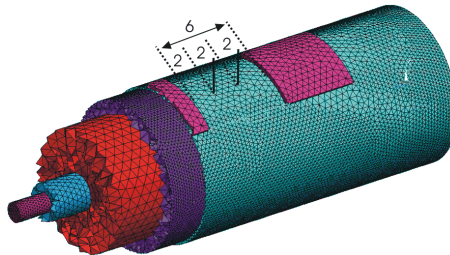


**Figure 4.1.** Cylindrical forearm model with different tissue layers and the square stimulating electrodes. Between the electrodes the recording needle electrodes are shown for clarity (not included in FE model).

#### 4.1.1.2. Measurements

The electric potential calculated with the FE model was verified using experimental data obtained in the upper arms of three healthy male subjects. The size and distance of the electrodes was the same as in the FE model ( $5 \times 5 \text{ cm}^2$ , distance 6 cm). A current regulated stimulator [KPPM02] using the same pulse amplitudes (9 mA) and pulse durations (0.1 msec and 1 msec) as in the FE models was used. Higher stimulation currents were not used to avoid too strong muscle contractions with needles inserted in the muscle.

The electrical potentials inside the muscle (intramuscular potential) and at the electrodes (surface potentials) were measured during one stimulation pulse. The voltage and current of a single pulse were measured after 2s of stimulation when steady state was reached [KKPM06]. The potentials inside the muscle were measured using needle electrodes from Medtronic (9013R0252). They measure the potential only at the tip of the needle. The needles were inserted 2 cm into the biceps muscle, at a spacing of 2 cm between the stimulating electrodes (see Figure 4.2). The surface potentials were measured directly at the contact of the stimulation electrodes.

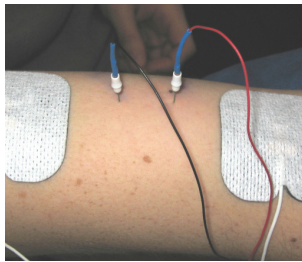


**Figure 4.2.** Experimental setup to measure intramuscular and surface potentials during TES.

#### 4.1.2. Results

The simulated and measured intramuscular potentials are depicted in Figure 4.3. The stimulation pulse is shown in the upper plot and the intramuscular potentials in the bottom plot. The rise times of the potentials are fast, indicating that the capacitive effect within the muscle

tissue is small. The simulation compares well with the experimentally measured potentials when using standard tissue thicknesses and tissue properties.

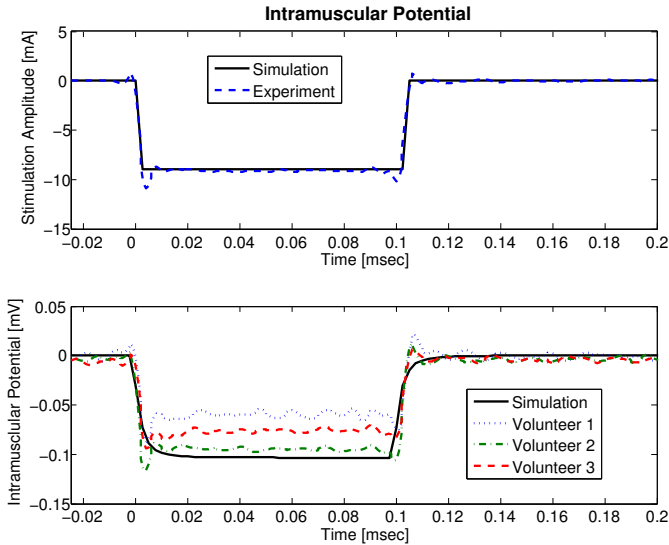


**Figure 4.3.** Validation of intramuscular potential.

In Figure 4.4 the simulated and measured surface potentials are plotted. The slow rise time of the surface potential indicates the strong capacitance of the skin layer. The simulated surface potentials also compare well with the measured potentials.

### 4.1.3. Discussion

The comparison of the simulation results with the experimental results showed that it is possible to describe the electrical potentials during TES with a transient FE model that incorporates published values of resistivities and permittivities. The model described not only the resistive properties of the tissues [MSD<sup>+</sup>06, LME01] but also the capacitive properties. This is particularly important to describe the strong capacitive effect of the potentials on the skin [Lyk71, DR99]. The time dependence is relevant if new pulse stimulation technologies, as for example presented in [JM05], are being developed. For such cases a transient

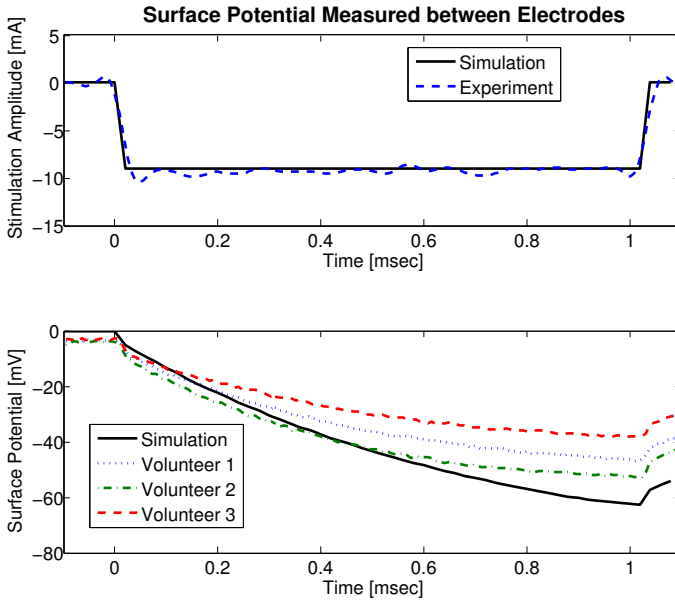


**Figure 4.4.** Validation of surface potential.

model allows one to optimize the power consumption because both the time dependent currents and the time dependent voltages can be simulated ( $P(t) = U(t) * I(t)$ ). However, the simulation results also show that due to the fast rise times of the potentials within the muscle tissue a static simulation is adequate if only these potentials are of interest. This is for example the case when the potentials along axons are calculated and then applied to axon models (section 3.3). A further analysis and discussion on the influences of the capacitive effects can be found in chapter 7.1.

In conclusion, by comparing simulations with experiments it has been shown that intramuscular and surface potentials that are present during TES can be described with a transient FE model.

## 4.2. Motor Thresholds, Chronaxie, and Rheobase

Electrical stimulation models can be verified by comparing simulated motor thresholds at one specific pulse duration with experimentally obtained motor thresholds [BK04]. Alternatively, simulated strength-duration curves can be compared with experimentally obtained strength-duration data [SMD87]. Strength-duration curves describe the stimulation current amplitude versus the pulse duration (PD) for threshold activation (Figure 2.11). From strength-duration curves rheobase and chronaxie (section 2.2.5) can be derived [Ged04]. Experimentally obtained chronaxie values using electrodes placed close to the excited axon (implantable systems, clamp experiments, animal studies and needle electrodes) are between  $30 \mu s$  and  $150 \mu s$  [Fit62, Bos83, Rat90]. Published non-linear nerve models were experimentally verified in this range of chronaxie values [McN76, CRRS79, SMD87, Rat90, MRG02]. However, chronaxie values that were obtained experimentally using surface electrodes are longer. In dogs the chronaxie using surface electrodes was  $170 \mu s$  [VVG<sup>+</sup>92] and in humans between  $200 \mu s$  and  $700 \mu s$  [SKPS05, Har71, KBAB00].

It is unclear if such non-linear axon models that were designed for implantable systems (chronaxie:  $30 - 150 \mu s$ ) can be used in a combined TES model to describe TES (chronaxie:  $200 - 700 \mu s$ ). Therefore, in this section motor thresholds, chronaxie, and rheobase of the TES model were compared with values measured in human volunteers. These values were calculated and measured for different electrode sizes and for single and array electrodes. Different axon models were used in the TES model in order to find an adequate axon model to describe nerve activation in TES.

### 4.2.1. Methods

#### 4.2.1.1. TES Model

Nerve activation was calculated using the TES model introduced in section 3.3 with the parameters that are summarized in the tree structure below.



FE model	
—	Geometry .....cylindrical geometry
—	— Tissue thicknesses .....standard values from Table 3.2
—	— Tissue properties .....standard values from Table 3.3
—	— Electrode type .....single and array electrodes
—	— — Electrode sizes ..... $0.8 \times 0.8 - 5 \times 5 \text{ cm}^2$
—	— — Gaps in array .....1 mm, 3 mm, and 5 mm
—	— — Electrode distance .....11 cm
—	Equation .....transient equation (3.16)
—	Stimulation pulse .....monopolar current regulated
—	— Amplitude .....bisection search
—	— Duration .....0.05 ms to 2 ms
Nerve model	
—	Model IDs .....A to D (see Table 3.4)
—	Type .....one single axon
—	Axon diameter ..... $16 \mu\text{m}$
—	Axon depth (from fat-muscle interface) .....1 mm

The cathodes had sizes between  $0.8 \times 0.8 \text{ cm}^2$  and  $5 \times 5 \text{ cm}^2$  (the same as used in the experiments in section 4.2.1.2). The motor thresholds of three array electrodes with gap sizes of 1 mm, 3 mm, and 5 mm were investigated. The geometry of the array electrode is shown in Figure 13.1. The active region of the array electrode had a size of 2 by 2 elements (element size 13 mm). The anode had a size of  $5 \times 10 \text{ cm}^2$ . Biphasic current regulated pulses with a certain pulse amplitude ( $I$ ) and pulse duration  $PD$  were used.

Axon models A to D from Table 3.4 were used in the TES model to conclude on activation. Because motor thresholds were of interest a thick superficial axon ( $16 \mu\text{m}$  diameter) was placed just below the fat layer at a depth of 1 mm (measured from the fat-muscle interface) centered under the cathode. This is an intermediate value of the possible depths and axon diameters that can be found amongst different subjects [RACS98, Sta05]. The motor threshold amplitudes were determined using bisection search with an accuracy of 0.01 mA.

Initial fiber activation was verified in order to make sure that the AP was not initiated at the nerve model boundary. The threshold of the TP to detect activation was set to 0 mV. Additionally, only axons with propagating APs were counted as activated by ensuring that after detection of the initial AP also at all other nodes the TP was above 0 mV.

#### 4.2.1.2. Automated Motor Threshold Measurements

The goal of the experimental measurements was to identify motor thresholds for different electrode sizes on the forearm of human volunteers in order to verify the TES model.

**Subjects** Experimental measurements were undertaken from ten healthy subjects (two females and eight males). The subjects' mean age was  $27.6 \pm 2.27$  (range 25-32), mean height was  $182.3 \pm 9.64$  (range 167-197), and mean body mass was  $72.9 \pm 13.65$  (range 51-97).

**Procedure** Transcutaneous electrical stimulation was applied using a Compex Motion stimulator [KPPM02]. On each subject the muscle motor point of the right Flexor Digitorum Superficialis, which articulates the middle finger, was identified using a stainless steel searching probe (0.5 cm tip diameter). Water was used to ensure good contact of the probe with the skin. Biphasic, asymmetric pulses with a duration of  $300 \mu\text{s}$  and a repetition frequency of 1 Hz were applied. The probe was moved over the muscle until the point that required the least current to generate minimal movement of the middle finger was identified. Because motor points move depending on limb configuration it was ensured that the arm position was not changed during the experiment. After marking the motor point, motor thresholds for different electrode sizes were determined. The different exciting electrodes (cathode) were placed centered on the marked motor point and the indifferent electrode (anode) was placed 11 cm distally. Standard self adhesive hydrogel electrodes (Compex) with sizes of  $0.8 \times 0.8 \text{ cm}^2$ ,  $1.4 \times 1.4 \text{ cm}^2$ ,  $2.3 \times 2.3 \text{ cm}^2$ ,  $3.2 \times 3.2 \text{ cm}^2$ ,  $4.1 \times 4.1 \text{ cm}^2$ , and  $5 \times 5 \text{ cm}^2$  were used as cathode and a large  $5 \times 10 \text{ cm}^2$  electrode as anode. The array electrodes with the different gap sizes were custom made using a carbon rubber substrate and a hydrogel skin interface. The different electrodes were tested in random. Biphasic current regulated pulses with a duration of  $300 \mu\text{s}$  and a repetition frequency of 25 Hz were applied using a Compex Motion stimulator [KPPM02]. For the largest electrode ( $5 \times 5 \text{ cm}^2$ ), additional pulse durations (0.05 ms to 2 ms) were applied in order to obtain strength-duration curves. Kuwabara et al. [KBO<sup>+</sup>04] demonstrated that motor thresholds can be accurately detected with an accelerometer placed at the articulated finger (QTRAC-Program). We used a similar approach using an accelerometer (Compex MI-sensor) that was placed on top of the cathode (left image in Figure 4.5) in order to automatically detect

the motor threshold by measuring the 25 Hz vibration of the activated muscle. The accelerometer was held in place with an elastic bandage that was wrapped around the subject's arm (right image in Figure 4.5). For the detection of the motor threshold a fast fourier transform (FFT) of the signal from the accelerometer was performed. When the amplitude of the FFT at 25 Hz was at least three times larger than the mean amplitude at frequencies between 20 Hz and 30 Hz, then the motor threshold was "detected".

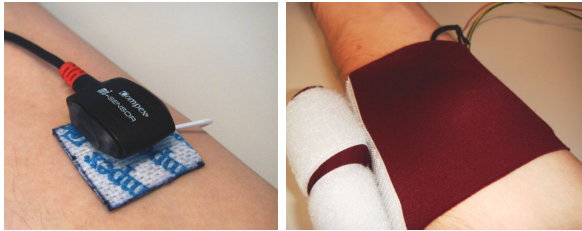


**Figure 4.5.** Left: Accelerometer placed on top of stimulation electrode in order to detect motor threshold. Right: Elastic bandage was used to hold accelerometer in place.

**Technical Setup** The Compex Motion stimulator offered two analog inputs and a digital trigger to control different stimulation parameters. One analog input was programmed to control the current amplitude, the second analog input controlled the pulse duration, and the trigger was used to start and stop stimulation. The two analog inputs and the trigger were controlled with a digital acquisition card (National Instruments DAQ Card 6036) from National Instruments (NI) on a Notebook PC. The signal from the accelerometer was measured using the same DAQ card. A Labview (National Instruments Corporation, Austin, TX, USA) program on the Notebook PC increased the current amplitude every second by 0.3 mA (starting at 0 mA) until the motor threshold was detected. This detection was repeated three times and the average was calculated for each electrode size. The motor threshold using the presented method could be determined with an accuracy of 0.3 mA what is comparable to a method that detected finger twitch movements (QTRAC-Program) [KBO<sup>+</sup>04].

**Data Analysis** Using the described technique motor thresholds were detected for different electrode sizes. The effect of the electrode size was analyzed using a one way analysis of variance (ANOVA). Significant ( $p < 0.01$ ) F ratios were further analyzed with Fisher's post hoc test.

#### 4.2.1.3. Rheobase and Chronaxie

Rheobase  $I_{rh}$  and chronaxie  $T_{ch}$  (see section 2.2.5) obtained from strength-duration curves calculated with the TES model were compared to experimentally obtained rheobase and chronaxie values that were previously published. Lapicque's equation  $I_{th} = I_{rh}/(1 - \exp(-PD/T_{ch}))$  [Lap07] was fitted to the simulated and measured strength-duration data in order to obtain  $I_{rh}$  and  $T_{ch}$ . R-square ( $R^2$ ) values between the fitted curves and the actual strength-duration data were calculated and were above 0.995 what indicated a reasonable accuracy of the fit.

### 4.2.2. Results

#### 4.2.2.1. Strength-Duration Curves, Chronaxie, and Rheobase

Figure 4.6 shows the comparison of the strength-duration curves that were calculated using the TES model with experimentally obtained motor thresholds for different PDs. The TES model containing axon model D matches best the experimental measurements for all measured PDs. The thresholds obtained with axon models A, B, and C are all at least a factor of four higher.

In Figure 4.6 the chronaxie values ( $T_{ch}$ ) of the TES model that were calculated from the simulated strength-duration curves are depicted. The calculated chronaxie values for the different axon models are summarized in Table 4.1. The previously published chronaxie values for implantable systems are shown in the same Table 4.1. For all axon models the chronaxie values of the TES model were higher compared to the published chronaxie values (implantable). The chronaxie values using axon model D were in the range of experimentally obtained chronaxie values for TES, which are between  $200 \mu s$  and  $700 \mu s$  [SKPS05, Har71, KBAB00]. The values with axon model A ( $157 \mu s$ ), B ( $137 \mu s$ ), and C ( $33 \mu s$ ) were below the experimental range of  $200 \mu s$  to  $700 \mu s$ . Also the rheobasic currents using nerve model D compared the best with the experiments as already indicated by the strength duration curves in Figure 4.6.

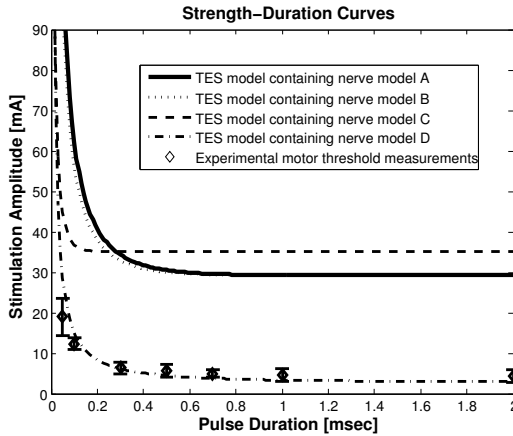


**Figure 4.6.** Strength-duration curves from the TES model with the different tested axon models and the experimentally obtained motor thresholds for different PDs (mean and standard deviation) are shown. These results were produced using the  $5 \times 5 \text{ cm}^2$  electrodes.

Axon Model ID	Published Chronaxie Values [ $\mu\text{s}$ ]	Chronaxie in TES model [ $\mu\text{s}$ ]	Rheobase in TES model [mA]
A	100	157	29.3
B	100	137	29.2
C	26	33	35.1
D	150	457	2.97

**Table 4.1.** Comparison of published chronaxie values (implantable systems) with chronaxie values obtained with the TES model. Further, the rheobasic currents of the TES model including the different axon models are given.

The results show that nerve model D compares best with the experiments. Therefore, in the following two sections, where different electrode sizes and array electrodes are analyzed, only simulation results using nerve model D (MRG) are shown.

#### 4.2.2.2. Motor Thresholds for Different Electrode Sizes

The motor thresholds for different electrode sizes that were obtained with the TES model including axon model D are depicted in the notched

box plot<sup>1</sup> in Figure 4.7 for a pulse duration of  $300 \mu s$ . The measured motor thresholds are also depicted in Figure 4.7. As expected the current amplitudes required to reach motor threshold increase for larger electrodes. The one way ANOVA test for the effect of the electrode size was significant at the ( $p < 0.01$ ) level. Fisher's post hoc test revealed that the current amplitude increased significantly as electrode size increased.

When comparing the simulated with the experimental motor thresholds it can be seen that for small electrodes the simulated thresholds are at the lower end of the experimentally obtained motor thresholds. However, overall the simulation results are within the range of experimentally measured motor thresholds.

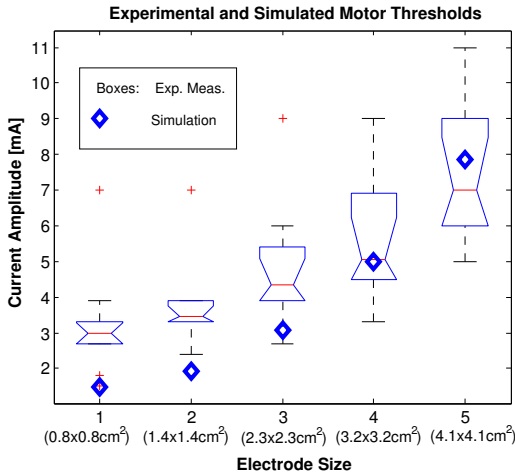


**Figure 4.7.** Notched box plot of the experimentally measured motor thresholds for different electrode sizes with overlaid simulated motor thresholds. The simulated thresholds (TES model including axon model D, pulse duration  $300 \mu s$ ) are in the range of experimentally measured thresholds.

<sup>1</sup>The results are presented in a notched box plot with whiskers. The box has lines at the lower quartile, median, and upper quartile values. The whiskers are lines extending from each end of the box to show the extent of the rest of the data. Outliers are data with values beyond the ends of the whiskers. The notches represent a robust estimate of the uncertainty about the medians for box-to-box comparisons. Boxes whose notches do not overlap indicate that the medians of the two groups differ at the 5% significance level.

### 4.2.2.3. Motor Thresholds of Array Electrodes with Different Gap Sizes

The motor thresholds for array electrodes with different gap sizes that were obtained using the TES model containing axon model D are depicted in Figure 4.8. Also the measured motor thresholds are depicted in Figure 4.8. They compare well with the simulated data. The motor thresholds significantly increase with larger gap sizes because nerve activation decreases underneath the gaps. A more detailed investigation on the determination of appropriate gap sizes for array electrodes is presented in chapter 13.

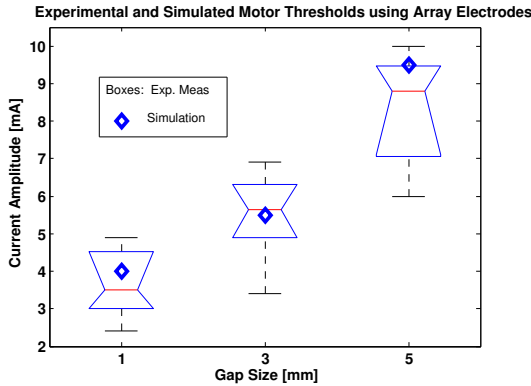


**Figure 4.8.** Experimentally obtained motor thresholds using array electrode with different gap sizes are compared with simulation results (TES model including axon model D, pulse duration  $300\ \mu\text{s}$ ).

### 4.2.3. Discussion

The results show that simulations using nerve model D compared the best with experimentally obtained data. Possible reasons are the following two:

- It was investigated if changes in the parameters of axon models A, B, and C can increase the chronaxie to values found with axon model D. The parameters from axon model D that mainly influence the chronaxie (membrane capacity, membrane resistivity,

and axoplasm resistivity [RB87]) were applied to axon models A, B, and C. The chronaxie values of axon models A, B, and C were at the most increased by 20%. Therefore, most probably, the double cable structure, with explicit representation of the nodes of Ranvier, paranodal, and internodal sections [MRG02] was responsible for the longer chronaxie and not the different parameters of axon model D.

- It was shown that the TES models using axon models A, B, or C had too high a rheobase (Figure 4.6) compared to the experimental measurements. The reason might be the different parameters of model D compared with model A, B, and C. The nodal leakage conductance  $g_L$  was  $7 \text{ mS/cm}^2$  in D, but  $30.3 \text{ mS/cm}^2$  in A and B, and  $128 \text{ mS/cm}^2$  in C. The axoplasmic resistivity  $\rho_i$  was  $70 \Omega\text{cm}$  in D instead of  $110 \Omega\text{cm}$  in A and B, and  $54.7 \Omega\text{cm}$  in C. Applying the parameters from model D in model A and B lowered the thresholds at  $0.2 \text{ msec}$  PD from  $36 \text{ mA}$  to  $10 \text{ mA}$  in A and from  $34 \text{ mA}$  to  $9 \text{ mA}$  in B. These thresholds are closer to the experimentally obtained thresholds (see Figure 4.6) of  $6.3 \text{ mA}$ . Applying the parameters from model D in model C did not significantly change the motor threshold found in the TES model containing axon model C.

**Spatial Position of the Nodes of Ranvier** Axons with different diameters do not have the same internodal distance. As a consequence the nodes do not lie at the same position underneath the electrode and could lead to different activation thresholds. This was investigated by shifting the node of an axon by  $0.1 \text{ mm}$  steps within the internodal distance. Only small changes of the motor thresholds ( $<0.01 \text{ mA}$ ) could be observed that only minimally influence the results.

#### 4.2.4. Conclusion

The TES model containing axon model D (MRG) can describe nerve activation for different electrode sizes and for array electrodes.

### 4.3. Recruitment and Forces

Apart from strength-duration curves, which describe only the excitability at motor threshold (thickest axons activated), measured force or



torque versus PD curves were used to describe the excitability of nerves (where thinner axons are also activated) [RACS98] and to verify ES models [LGD06]. Such measurements at higher stimulation intensities provide additional understanding of the nerve recruitment and show how many axons are activated within nerve bundles (section 2.2.4.1) as long as muscles are not directly activated (Crago et al. [CPMVdM74] showed that only about 3% of the measured twitch force is produced by direct muscle stimulation). These curves show either the stimulation amplitude versus the PD at a fixed force output [VCR67, CPMVdM74, KBM06] or the force versus the PD at a fixed amplitude [BJ87, GDB07]. The influence of the muscle properties on the measurement can be minimized by measuring twitch forces (single stimulation pulse) instead of tetanic forces [BMB<sup>+</sup>00]. This has the advantage that experimentally measured twitch forces can be directly compared with nerve recruitment obtained from nerve models [LGD06]. As such, twitch force measurements from human volunteers that are compared with the nerve recruitment from the TES model are presented in this section. This comparison can be used to show which of the tested nerve models (Table 3.4) are most suitable to be used for TES.

### **4.3.1. Methods**

#### **4.3.1.1. TES Model**

Nerve activation was calculated using the TES model introduced in section 3.3 with the parameters that are summarized in the tree structure below.

FE model	
├	Geometry .....cylindrical geometry
├	├ Tissue thicknesses .....standard values from Table 3.2
├	├ Tissue properties .....standard values from Table 3.3
├	├ Electrode type ..... single electrodes
├	├├ Electrode sizes ..... $5 \times 5 \text{ cm}^2$
├	├├ Electrode distance ..... 11 cm
├	Equation ..... transient equation (3.16)
├	Stimulation pulse .....monopolar current regulated
├	├ Amplitude ..... 20 mA
├	├ Duration ..... 0.05 ms - 2 ms
Nerve model	
├	Model IDs ..... A to D (Table 3.4)
├	Type .....multiple nerve bundles
├	Axon diameter .....bimodal with peaks at $6 \mu\text{m}$ and $13 \mu\text{m}$
├	Axon depth .....0.2 cm - 1.1 cm

In section 2.2.3 it was introduced that in humans axons with different diameters are gathered in nerve bundles. Multiple nerve bundles innervate muscles and these nerve bundles lie in different depth within the body [Sta05]. The nerve model in the TES model was designed accordingly. It consisted of nerve bundles that had a length of 15 cm and were centered under the cathode at depths (from fat-muscle interface) between 0.2 cm and 1.1 cm with 0.1 cm spacing (see Figure 3.7). Each of the ten nerve bundles consisted of 100 axons with diameters distributed according to the bimodal distribution in human nerve bundles with peaks at  $6 \mu\text{m}$  and  $13 \mu\text{m}$  [RHK<sup>+</sup>94, PF07]. The minimal axon diameter was  $4 \mu\text{m}$  and the maximal diameter was  $16 \mu\text{m}$ . Axon models A to D from Table 3.4 were used in the nerve bundles. Recruitment *Rec* was defined as the percentage of axons that were activated in all nerve bundles that consisted in total of 1000 axons (10 nerve bundles each 100 axons). Axons with different diameters had different inter-nodal distances ranging from 0.4 mm to 1.6 mm. The first nodes of all axons in each nerve bundle were aligned with each other.

#### 4.3.1.2. Experimental Measurements

Isometric twitch forces were measured in three human volunteers (age: 25-28, one female, two male) in order to compare recruitment-duration curves with results from the TES model.

Monophasic, current regulated stimulation pulses were applied with

the Compex Motion Stimulator [KPPM02]. The electrodes ( $5 \times 5 \text{ cm}^2$ , Compex hydrogel) were placed over the motor point of the Flexor Digitorum Superficialis that articulates the middle finger as described in section 4.2.1.2. In order to avert potentiation, 300 stimulation pulses were applied prior to data capture.

The isometric twitch forces of the middle finger were measured with the dynamic grasp assessment system (DGAS) [KPA<sup>+</sup>00]. Single stimulation pulses with an amplitude of 20 mA and with PDs of 0.05, 0.1, 0.3, 0.5, 0.7, 1, and 2 msec were randomly applied every 2.5 s to 5 s. Each PD was applied a total of six times (randomized). Each data series was normalized to its maximal value in order to obtain recruitment-duration curves.

#### 4.3.1.3. Recruitment-Duration Curves and Time Constants

Simulated recruitment-duration curves were compared with experimentally obtained recruitment curves by comparing the corresponding time constants  $\tau$  [CBM07]. The time constants  $\tau_{sim}$  of the recruitment-duration curves from the TES model were compared with the time constants  $\tau_{exp}$  of the experimentally measured recruitment-duration curves. Both time constants were calculated by fitting equation (4.1) to the recruitment data as suggested in [CBM07].

$$Rec = Rec_{sat}(1 - e^{-(PD - PD_0)/\tau}) \quad \text{for } PD \geq PD_0 \quad (4.1)$$

$$Rec = 0 \quad \text{for } PD < PD_0 \quad (4.2)$$

$Rec$  is the recruitment,  $Rec_{sat}$  is the value where the recruitment saturates,  $PD$  represents the stimulation PD,  $PD_0$  is the threshold PD above which an AP is generated, and  $\tau$  is the time constant of the rising recruitment. R-square ( $R^2$ ) values between the fitted curves and the actual recruitment data were calculated and were above 0.995 what indicated a reasonable accuracy of the fit.

#### 4.3.2. Results and Discussion

The time constants  $\tau_{sim}$  (section 4.3.1.3) of the recruitment-duration curves from the TES model were compared with the time constants  $\tau_{exp}$  of the experimentally obtained recruitment-duration curves. The TES models including axon model A, B, or C used a current amplitude of 90 mA and the TES model with axon model D used a current amplitude of 20 mA. The current amplitude for models A, B, and C had to be

increased due to the higher motor thresholds of these axon models (compare to Figure 4.6).

The normalized recruitment-duration curves obtained from simulations are shown in Figure 4.9. The time constants  $\tau_{sim}$  were  $189 \mu s$  with axon model A,  $164 \mu s$  with axon model B,  $19 \mu s$  with axon model C, and  $476 \mu s$  with axon model D. The experimentally measured recruitment curves are shown in Figure 4.10. The time constants  $\tau_{exp}$  of these curves were  $489 \mu s$  in volunteer one,  $240 \mu s$  in volunteer two, and  $380 \mu s$  in volunteer three. The time constants  $\tau_{sim}$  obtained with the TES model containing axon models A, B, or D were within the 95% confidence interval of the time constants  $\tau_{exp}$  obtained by experimental measurements.  $\tau_{sim}$  using axon model C was more than a factor of ten shorter than the shortest  $\tau_{exp}$ .

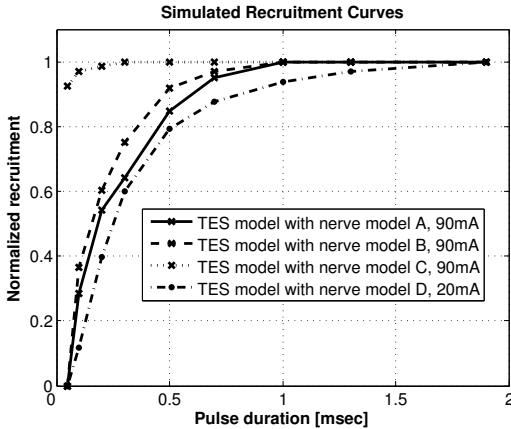


**Figure 4.9.** Simulated recruitment-duration curves (normalized) using TES model with different axon models (A to D).

## 4.4. Conclusions

The surface and intramuscular potential distribution of the transient FE model compared well with the measured electrical potentials in three human volunteers. This is in agreement with a comparison presented in [LSDK04]. By combining the FE model with different axon models a TES model was built and compared with measurements on

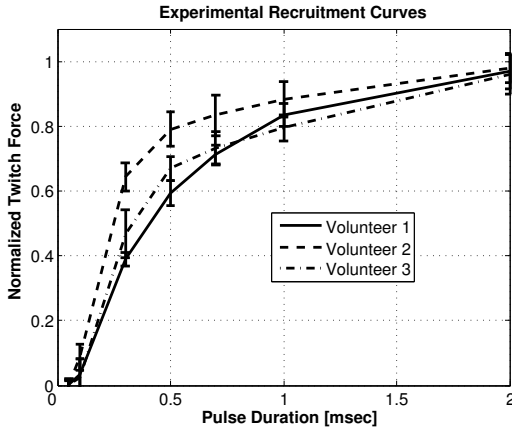


**Figure 4.10.** Recruitment-duration curves (normalized) of the middle finger from experimental measurements measured in three human volunteers. The stimulation amplitude was 20 mA.

human volunteers. Strength-duration curves and recruitment-duration curves calculated by the TES model and different axon models were compared with measurements. Only the TES model including axon model D (MRG-model) compared well with the experiments. The rheobasic currents using axon models A, B, and C were too high. Until now axon model D (MRG-model) was exclusively used for implanted ES systems [LGD06]. With the presented investigation it is shown that the MRG-model can also be used to model transcutaneous ES where the electrode-nerve distances are much larger than in implanted systems.



# 5

## Accuracy of AP Prediction Methods in TES

AP prediction (or threshold prediction) is a technique used to predict APs using linear axon models. The benefits compared to more accurate non-linear models are the cheaper computational costs of linear models and that they are invertible [MMG04] (i.e. the stimuli can be designed based explicitly upon the desired output). This prediction is an approximation and therefore afflicted by inaccuracies. These inaccuracies are documented for implantable systems where the electrodes are small ( $<0.2\text{ cm}^2$ ) and the electrode-axon distance is also small ( $<0.4\text{ cm}$ ) [WGD92, MMG04]. However, for TES where electrodes and distances are significantly larger these data is not available and are therefore presented in this chapter.

One of the goals of TES systems is to selectively activate certain nerves in order to accomplish a specific motor function, e.g. functional

grasp [Nat79, Nat92, PGWK97, CC98] without co-activation of adjacent nerves, e.g. wrist flexors. The degree of selectivity of transcutaneous electrodes is influenced by many parameters such as electrode sizes, the fat layer thickness or the nerve depth. In section 3.4.2.4 it was introduced how the selectivity can be calculated using activation volumes. The calculation of such activation volumes utilizes threshold prediction methods (section 3.4.2.1) which use linear approximations of non-linear nerve models to predict nerve activation (section 3.4.1). These are therefore prone to inaccuracies. The simplest but still powerful linear approximation is the AF (section 3.2.1.2,  $AF$  in Table 3.4) introduced by Rattay et al. [Rat88]. For implantable stimulation systems with small electrode-axon distances Warman et al. [WGD92] found that not only the AF at each axon node should be considered but also an ohmic term due to currents from adjacent nodes. Therefore, the use of a linear cable (LC) model (e.g.,  $D^P$  in Table 3.4), which includes these ohmic currents, was proposed instead of the AF [WGD92]. A detailed analysis of the accuracy of threshold predictions (using AF and linear cable model) was presented in [MMG04] and [BM06]. The relative errors between models were assessed for different electrode sizes, electrode-axon distances, pulse durations, and axon diameters. However, the investigated geometries and parameters were chosen for implantable or invasive systems. Stimulation was from either point sources or small electrodes ( $<0.2\text{ cm}^2$ ) and short electrode-axon distances ( $<0.4\text{ cm}$ ) were used (e.g. [SG06, MG02, PB98]).

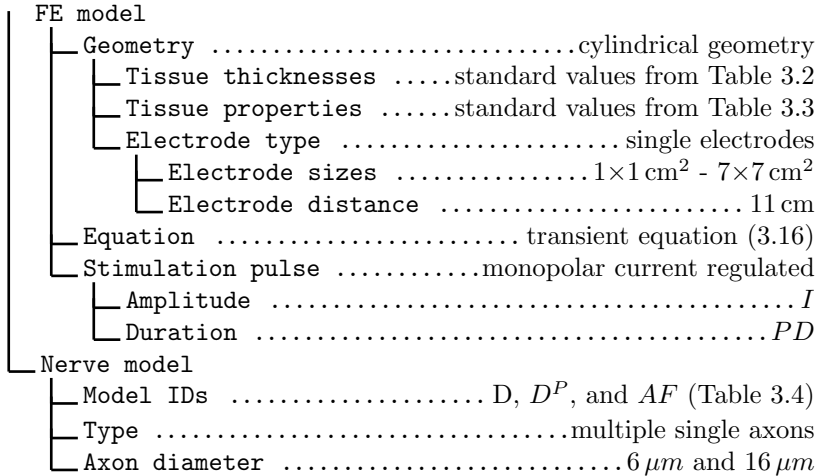
In this chapter the accuracy of two AP prediction methods (linear cable model and AF) is quantified with relative threshold prediction errors that were previously used in [WGD92, MMG04]. The difference to the previous publications is that the parameters chosen are common in TES (larger electrodes between  $1\times 1\text{ cm}^2$  and  $7\times 7\text{ cm}^2$ , larger electrode-axon distances between  $0.4\text{ cm}$  and  $3\text{ cm}$ ) rather than for implantable electrodes. Furthermore, a new spatial description of such prediction errors is introduced (section 5.1.3). These spatial prediction errors are of special importance in order to quantitatively define the accuracy of activation volumes (activation volumes were introduced in section 3.4.2.1).



## 5.1. Methods

### 5.1.1. TES Model

The parameters that were used for the TES model (section 3.3) are summarized in the tree structure below.



One non-linear axon model (model D (MRG) in Table 3.4) and two linear axon models (models  $D^P$  and  $AF$  in Table 3.4) were used to describe nerve activation based on the potential distribution calculated with the FE model. The axon models (12 cm long with axon diameters between 6  $\mu m$  and 16  $\mu m$ ) were placed in the volume representing muscle underneath the cathode (Figure 3.9).

### 5.1.2. Relative Threshold Prediction Errors

A method to predict nerve activation thresholds with linear nerve models was discussed in detail in [WGD92, MMG04] and was reviewed in section 3.4.1.

The error that occurs when linear nerve models are used to predict nerve activation instead of non-linear nerve models can be expressed with relative threshold prediction errors [WGD92, MMG04]. These errors were calculated for the linear cable model (model  $D^P$  in Table 3.4) and the AF (model  $AF$  in Table 3.4) with respect to the non-linear cable model (model D in Table 3.4). Relative threshold prediction errors are not constant, rather they are a function of the parameters of electrode

size, nerve depth, pulse duration and axon diameter. In the presented work parameters that are common in TES were used. Electrode sizes  $S$  were  $1 \times 1 \text{ cm}^2$ ,  $2 \times 2 \text{ cm}^2$ ,  $3 \times 3 \text{ cm}^2$ ,  $5 \times 5 \text{ cm}^2$ , and  $7 \times 7 \text{ cm}^2$ . Nerve depths  $L$  were 0.1 cm, 0.6 cm, 1.1 cm, 1.6 cm, 2.1 cm, and 2.6 cm (nerve depth was the distance from the fat-muscle interface to the nerve model and is indicated in Figure 3.9 with the term  $AD$  (activation depth)). Stimulation pulse durations  $PD$  were 0.1 msec, 0.2 msec, 0.3 msec, 0.5 msec, and 1 msec. Axon diameters  $D$  were  $6 \mu\text{m}$ ,  $8.5 \mu\text{m}$ ,  $11 \mu\text{m}$ ,  $13.5 \mu\text{m}$ , and  $16 \mu\text{m}$ .

The threshold voltages  $V_{TP}^{th,LC}(I^{th}(S, L, PD, D))$  of the TP for the linear cable model and  $V_{TP}^{th,AF}(I^{th}(S, L, PD, D))$  for the AF are compared with the threshold voltages using standard values  $S_0$ ,  $L_0$ ,  $PD_0$ , and  $D_0$ , which are denoted  $V_{TP,0}^{th,LC}(I^{th}(S_0, L_0, PD_0, D_0))$  and  $V_{TP,0}^{th,AF}(I^{th}(S_0, L_0, PD_0, D_0))$ . Electrode size  $S_0$  was  $3 \times 3 \text{ cm}^2$ , nerve depth  $L_0$  was 1.1 cm, pulse duration  $PD_0$  was 0.3 msec and axon diameter  $D_0$  was  $11 \mu\text{m}$ . The relative threshold prediction errors are defined for the linear cable model (Equation (5.1)) and the AF (Equation (5.2)).

$$E^{LC} = \frac{(V_{TP}^{th,LC} - V_{TP,0}^{th,LC})}{V_{TP,0}^{th,LC}} * 100[\%] \quad (5.1)$$

$$E^{AF} = \frac{(V_{TP}^{th,AF} - V_{TP,0}^{th,AF})}{V_{TP,0}^{th,AF}} * 100[\%] \quad (5.2)$$

### 5.1.3. Spatial Prediction Errors

In addition to the established relative threshold prediction errors a new method that calculates absolute spatial prediction errors is proposed. This spatial representation is especially useful to assess the accuracy of the size of activation volumes.

The spatial prediction errors are calculated on a 2D axial cut as shown in Figure 5.1. The cut was performed through the center of the cathode. The cut of the activation volumes are denoted activation lines (AL) (see Figure 5.1). The predicted activation line is a contour that was produced using the prediction threshold  $V_{TP,0}^{th,LC}$  or  $V_{TP,0}^{th,AF}$ . The "accurate" activation line was calculated using non-linear axon models that were placed perpendicular to the cutting plane (indicated with dots in the left part of Figure 5.1) on a grid with 0.2 mm spacing as it was done in [BM06]. The "accurate" activation line in Figure 5.1 encloses all axons

that were activated and was constructed using the "marching cubes" algorithm [LC87]. The distances between the predicted and the "accurate" activation line (shown with arrows in the right part of Figure 5.1) indicate the local metric error of the prediction. These distances were calculated by intersecting the normal vectors of one curve with the second curve. The mean of all distances is denoted mean distance and was used to quantify the spatial prediction error.

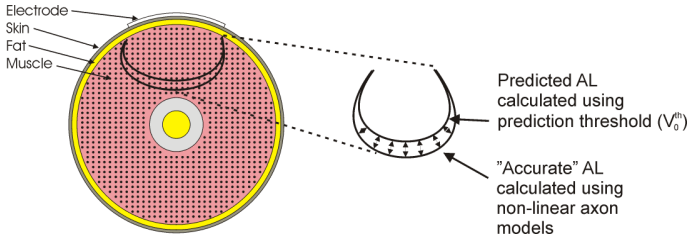


**Figure 5.1.** In the left part of the image an axial cut of the cylindrical arm model containing two activation volumes is shown. The cut goes through the center of the electrode. One activation volume on the cutting plane was produced using a prediction threshold (predicted activation volume) and the second one was generated using non-linear axon model ("accurate" activation volume). In the right part of the image the arrows indicate the inaccuracy of the predicted activation volume. The mean of the length of all arrows is denoted mean distance and was used to quantify spatial prediction errors.

## 5.2. Results

### 5.2.1. Relative Threshold Prediction Errors

Relative threshold prediction errors for the linear cable model  $E^{LC}$  and the AF  $E^{AF}$  were calculated for different electrode sizes  $S$ , nerve depths  $L$ , pulse durations  $PD$ , and axon diameters  $D$  (see Tables 5.1, 5.2, and 5.3). Predictions with the linear cable model produce smaller errors compared to predictions using the AF. Relative threshold prediction errors for different electrode sizes and nerve depths are largest for stimulations with small electrodes close to the axon (Table 5.1 (linear cable) and 5.2 (AF)). The threshold prediction errors for the tested pulse durations and axon diameters (Table 5.3) are larger than the threshold prediction errors for the tested electrode sizes and nerve depths.

$E^{LC}$ [%]		Electrode size (S)				
		$1 \times 1 \text{ cm}^2$	$2 \times 2 \text{ cm}^2$	$3 \times 3 \text{ cm}^2$	$5 \times 5 \text{ cm}^2$	$7 \times 7 \text{ cm}^2$
Depth (L)	0.1 cm	19.08	-1.24	4.51	6.34	6.90
	0.6 cm	10.59	3.60	-1.14	-4.12	-2.89
	1.1 cm	7.32	3.87	0.00	-4.90	-5.30
	1.6 cm	1.62	-0.99	-0.85	-5.12	-6.09
	2.1 cm	9.72	-3.00	-2.51	-5.52	-5.35
	2.6 cm	12.60	-2.55	-2.46	-4.42	-5.94

**Table 5.1.** Relative threshold prediction errors  $E^{LC}$  [%] of linear cable model for different nerve depths  $L$  and electrode sizes  $S$  for fixed pulse duration  $PD = 0.3 \text{ msec}$  and axon diameter  $D = 11 \mu\text{m}$ .

$E^{AF}$ [%]		Electrode size (S)				
		$1 \times 1 \text{ cm}^2$	$2 \times 2 \text{ cm}^2$	$3 \times 3 \text{ cm}^2$	$5 \times 5 \text{ cm}^2$	$7 \times 7 \text{ cm}^2$
Depth (L)	0.1 cm	51.25	8.47	26.47	29.97	29.70
	0.6 cm	25.17	9.71	-2.68	-4.08	-0.99
	1.1 cm	9.73	4.83	0.00	-6.75	-6.68
	1.6 cm	3.78	0.87	-1.81	-6.09	-7.80
	2.1 cm	-3.04	-2.91	-4.04	-6.11	-7.53
	2.6 cm	-7.02	-4.44	-5.21	-5.89	-7.57

**Table 5.2.** Relative threshold prediction errors  $E^{AF}$  [%] of AF for different nerve depths  $L$  and electrode sizes  $S$  for fixed pulse duration  $PD = 0.3 \text{ msec}$  and axon diameter  $D = 11 \mu\text{m}$ .

		Pulse duration (PD)				
		0.1 msec	0.2 msec	0.3 msec	0.5 msec	1 msec
$E^{LC}$ [%]		144.81	36.13	0	-28.26	-47.63
$E^{AF}$ [%]		144.81	36.13	0	-28.26	-47.63
		Axon diameter (D)				
		$6 \mu\text{m}$	$8.5 \mu\text{m}$	$11 \mu\text{m}$	$13.5 \mu\text{m}$	$16 \mu\text{m}$
$E^{LC}$ [%]		394.73	80.56	0	-32.20	-52.52
$E^{AF}$ [%]		394.73	80.56	0	-32.20	-52.52

**Table 5.3.** Relative threshold prediction errors  $E^{LC}$  and  $E^{AF}$  [%] for different pulse durations  $PD$  and axon diameters  $D$  for fixed electrode size  $S = 3 \times 3 \text{ cm}^2$  and nerve depth  $L = 1.1 \text{ cm}$ .

$MD$ for LC [mm]	Electrode size (S)				
	$1 \times 1 \text{ cm}^2$	$2 \times 2 \text{ cm}^2$	$3 \times 3 \text{ cm}^2$	$5 \times 5 \text{ cm}^2$	$7 \times 7 \text{ cm}^2$
0.1 cm	0.12	-0.06	0.18	0.23	0.25
0.6 cm	0.21	0.11	-0.05	-0.37	-0.21
1.1 cm	0.16	0.12	0	-0.39	-0.71
1.6 cm	0.04	-0.04	-0.04	-0.42	-0.75
2.1 cm	0.34	-0.14	-0.14	-0.48	-0.63
2.6 cm	0.54	-0.17	-0.16	-0.42	-0.79

**Table 5.4.** Spatial prediction errors described by mean distances (MDs) [mm] using prediction based on linear cable model with different nerve depths  $L$  and electrode sizes  $S$  for fixed pulse duration  $PD = 0.3msec$  and axon diameter  $D = 11\mu m$ .

### 5.2.2. Spatial Prediction Errors

The spatial prediction errors were described with mean distances as introduced in section 5.1.3 and are obtained by comparing a predicted activation line with an "accurate" activation line in a 2D plain (see Figure 5.1). Table 5.4 shows mean distances between the activation line produced using the non-linear (MRG) model ("accurate" activation line) and the predicted activation line produced using the linear cable model. In Table 5.5 the mean distances for the prediction using the AF is shown. In those two tables the mean distances were calculated for different electrode sizes and nerve depths. Table 5.6 contains the mean distances for pulse duration and axon diameter changes. In all tables positive distances [mm] mean that the predicted activation line was larger (overestimated) and negative distances mean that the predicted activation line was smaller (underestimated) than the activation line calculated using the non-linear axon models. Spatial prediction errors for changing pulse durations and axon diameters are larger than errors obtained for different electrode sizes and nerve depths which agrees with the results using the relative threshold prediction errors (section 5.2.1). The spatial prediction errors for different electrode sizes and nerve depths are below 1 mm with both prediction methods (Tables 5.4 and 5.5). However, they are up to several millimeters (9.92 mm) for different pulse durations and axon diameters (Table 5.6).

<i>MD</i> for AF [mm]		Electrode size ( <i>S</i> )				
		$1 \times 1 \text{ cm}^2$	$2 \times 2 \text{ cm}^2$	$3 \times 3 \text{ cm}^2$	$5 \times 5 \text{ cm}^2$	$7 \times 7 \text{ cm}^2$
Depth ( <i>L</i> )	0.1 cm	0.35	0.15	0.59	0.67	0.65
	0.6 cm	0.42	0.29	-0.12	-0.37	-0.06
	1.1 cm	0.2	0.16	0	-0.57	-0.93
	1.6 cm	0.11	0.03	-0.09	-0.51	-0.99
	2.1 cm	-0.11	-0.13	-0.22	-0.53	-0.97
	2.6 cm	-0.33	-0.24	-0.33	-0.56	-0.96

**Table 5.5.** Spatial prediction errors described by mean distances (MDs) [mm] using prediction based on AF for different nerve depths  $L$  and electrode sizes  $S$  for fixed pulse duration  $PD = 0.3 \text{ msec}$  and axon diameter  $D = 11 \mu\text{m}$ .

		Pulse duration ( <i>PD</i> )				
		0.1 msec	0.2 msec	0.3 msec	0.5 msec	1 msec
<i>MD</i> for LC [mm]		3.19	1.32	0	-1.54	-3.01
<i>MD</i> for AF [mm]		4.72	1.47	0	-1.51	-2.89
		Axon diameter ( <i>D</i> )				
		$6 \mu\text{m}$	$8.5 \mu\text{m}$	$11 \mu\text{m}$	$13.5 \mu\text{m}$	$16 \mu\text{m}$
<i>MD</i> for LC [mm]		5.02	2.42	0	-1.79	-3.43
<i>MD</i> for AF [mm]		9.92	2.97	0	-1.78	-3.33

**Table 5.6.** Spatial prediction errors described by mean distances (MDs) [mm] using prediction with linear cable model and AF for different pulse durations  $PD$  and axon diameters  $D$  for fixed electrode size  $S = 3 \times 3 \text{ cm}$  and nerve depth  $L = 1.1 \text{ cm}$ .

### 5.3. Discussion

Relative threshold prediction errors were proposed to estimate the accuracy of predictions with linear nerve models [WGD92, MMG04]. For implantable systems, where usually single nerve bundles close to the small stimulation electrode were investigated, such a definition is sufficient. However, in TES where nerves are expected at different places within a human limb, a spatial definition of the prediction errors is more powerful. The spatial prediction errors (defined in section 5.1.3) indicate how much larger or smaller the activation volume actually is when a more precise non-linear nerve model is used. The relative prediction errors as used in [WGD92, MMG04] were for example as high as 51.25% (Table 5.2) although the spatial errors were only 0.35 mm (Table 5.5). This indicates that spatial threshold prediction errors are more illustrative for TES.

Spatial prediction errors were assessed in a plane (2D) on activation lines and not in 3D on activation volumes. The reason is that non-linear axon models that are only oriented in axial direction cannot be used to calculate an activation volume. An AP elicited at one node of a non-linear axon will propagate over the whole axon; even at nodes that would not be activated by the applied stimulation current. Therefore, a non-linear axon that passes a region where nerves are activated will be entirely activated. The only way to use non-linear axons to generate an activation volume would be to place all axons tangentially to the activation volume. However, this would mean that axons are no longer only oriented in axial direction, and that the orientation of an axon would be determined by the shape of the activation volume itself. This was not done because the simulation results were aimed not to be influenced by the axon orientation (only axially oriented axons were allowed).

Prediction errors for varying pulse durations and axon diameters are too large (up to 9.92 mm) for accurate predictions (Tables 5.3 and 5.6). Therefore, also in TES models either a lookup table or a curve fit as described in [BM06] is required for predictions with varying pulse duration and axon diameter. Such lookup tables for the two tested linear nerve models are provided in Tables 3.5 and 3.6.

Spatial prediction errors increase for smaller electrode sizes (Table 5.4 and 5.5). The identified reason is that the number of activated nodes on the nerve models change with respect to electrode size. Smaller electrodes stimulate less axon nodes simultaneously what results in a

higher activation threshold in non-linear models [RACS98]. This effect is not reproduced when using a constant prediction threshold in linear models and results in the prediction errors shown in Tables 5.4 and 5.5. This effect is mainly observed for nerves at less than 1.1 cm depth because the currents are spreading out quickly with depth.

The prediction errors also increase for smaller nerve depths (Tables 5.4 and 5.5). The reason is the same as found with different electrode sizes, a different number of axon nodes is activated for different nerve depths. For both, the electrode size and the nerve depth, the prediction using the linear cable model is slightly more accurate than the prediction using the AF (see Tables 5.4 and 5.5). However, the spatial prediction errors for both methods are always below 1 mm for the tested electrode sizes and nerve depths. Therefore, linear nerve models can be used for these parameters.

## 5.4. Conclusions

Threshold prediction errors for a linear cable model and the AF were investigated. It was found that threshold predictions for changing pulse durations and axon diameters require a lookup table or a curve fit for accurate predictions. For the tested electrode sizes and nerve depths spatial prediction errors are small ( $<1\text{mm}$ ). Thus, linear models can be used to produce activation volumes in TES.



Part III

**INFLUENCE OF  
TISSUE PROPERTIES  
ON TES**



# 6

## Overview

In this part the TES model introduced in chapter 3 is used to quantify the influences of different tissue properties on nerve activation. The aim is to identify the parameters that have a large influence on nerve activation. This indicates which parameters and tissue structures are important in TES models and which parameters can be neglected. Chapter 7 analysis the influences of macroscopic tissue properties within six sections:

- Section 7.1 investigates the influence of the *tissue permittivities* and if the capacitive effects can be neglected in TES.
- Section 7.2 investigates *tissue resistivities* with a focus on the non-linearity of the skin resistivity.
- Section 7.3 quantifies the influence of the *complex tissue composition* compared with simplified geometries like cylinders.
- Section 7.4 analyzes the impact of *tissue inhomogeneities*.
- Section 7.5 shows the influence of *tissue layer thicknesses*.
- Section 7.6 investigates the influence of the *electrode-axon distance* and the *axon diameter*.

After the focus on the macroscopic influences in chapter 7, the influence of a nerve bundle's microscopic structure on nerve activation is analyzed in chapter 8.

In chapter 9 the results of the analyzed influences are summarized and it is concluded on which parameters have the largest effect on nerve activation in TES.

# 7

## Electrical Tissues Properties and Tissue Composition

### 7.1. Tissue Permittivities (Capacitive Effects)

According to Plonsey et al. [PH67] capacitive effects in biological tissues can be neglected when modeling electromagnetic fields. This hypothesis is used in most recent TES models [MH90, RMMR04]. However, a review of material properties [GLG96] showed that the permittivities of the bulk tissues used in Plonsey's study were chosen too low. As a consequence Plonsey's argumentation which was based on inequality (7.1) is no longer valid.

$$\frac{\omega \varepsilon_0 \varepsilon_r}{\sigma} \ll 1 \quad (7.1)$$

In Equation (7.1)  $\omega$  is the angular frequency,  $\varepsilon_0 = 8.854 \times 10^{-12}$  F/m is the permittivity of vacuum,  $\varepsilon_r$  is the relative permittivity and  $\sigma$  denotes

Tissue Type	$\omega\varepsilon_0\varepsilon_r/\sigma$
Skin	0.03 - 10.01
Fat	0.0008 - 1.67
Muscle	0.01 - 0.69
Cortical Bone	0.006 - 0.01
Bone Marrow	0.004 - 0.01

**Table 7.1.** Capacitive effect criteria (7.1) evaluated with range of tissue properties from Table 3.3 and a frequency of 1 kHz.

the conductivity of the tissue. Evaluating the left hand side of Equation (7.1) using the range of permittivities and resistivities given in Table 3.3 and a frequency of 1 kHz leads to the ranges of values in Table 7.1. Inequality (7.1) is not always fulfilled and as a result the capacitive effects of the bulk tissues may have an effect and need further investigation before being neglected. In particular Stoykov et al. [SLTK01] found that the capacitive effects may have a considerable impact on EMG signals, which are in the same frequency range as TES pulses. For deep brain stimulation Butson et al. showed that the capacitance of the electrode-tissue interface has an influence on neural activation [BM05, BCHM07]. In this section the influence of the capacitive effects in TES is analyzed.

### 7.1.1. Methods

The parameters that were used for the TES model (section 3.3) are summarized in the tree structure below.

FE model	
├	Geometry .....cylindrical geometry
├	├ Tissue thicknesses .....standard values from Table 3.2
├	├ Tissue properties .....standard values from Table 3.3
├	├ Electrode type ..... single electrodes
├	├├ Electrode sizes ..... $5 \times 5 \text{ cm}^2$
├	├├ Electrode distance ..... 11 cm
├	Equation ..... transient equation (3.16)
├	Stimulation pulse .....monopolar current regulated
├	├ Amplitude ..... 5 mA - 20 mA
├	├ Duration ..... 0.05 ms - 2 ms
Nerve model	
├	Model ID ..... D (Table 3.4)
├	Type ..... multiple nerve bundles (see Figure 3.7)
├	Axon diameter .....bimodal with peaks at $6 \mu\text{m}$ and $13 \mu\text{m}$
├	Axon depth .....0.2 cm - 1.1 cm

The influence of the capacitive effects on nerve activation was investigated by changing the permittivities within the range of reported values in TES (Table 3.3). Nerve activation was quantified by calculating the nerve recruitment (REC) (section 2.2.4.1) for a current amplitude and a pulse duration that are commonly used in TES (15 mA and 0.3 msec). Furthermore, recruitment-(pulse)duration curves (section 2.2.4.1) of models including the capacitive effects were compared with models neglecting the capacitive effects.

### 7.1.2. Results

The influence of the capacitive effects of the different tissues (range given in Table 3.3) on *Rec* is shown in Table 7.2. Permittivity changes at the electrode-skin interface had no influence on *Rec* ( $< 0.1\%$ ). Skin and fat permittivities changed *Rec* by less than 2%. The muscle permittivity had the largest influence with 4.8%. Recruitment-duration curves were therefore calculated for the published range of muscle permittivities (Table 3.3) in order to identify an upper limit for the influence of the capacitive effects.

The recruitment-duration curves for the smallest and largest muscle permittivity are depicted in Figure 7.1. The curves show the percentage of axons that are activated in the nerve model for different pulse amplitudes and durations. The influence on the time constants  $\tau_{sim}$  (defined in section 4.3.1.3) was largest for small pulse amplitudes. For

Permittivity sensitivity ( $\epsilon_r$ )	
Electrode-skin interface (1 to 2000k)	0.1%
Skin (from 1k to 30k)	1.6%
Fat (from 1.5k to 50k)	1.8%
Muscle (from 100k to 2500k)	4.8%
Cortical bone (from 2.4k to 3.6k)	0.9%
Cone marrow (from 8k to 12k)	0.4%

**Table 7.2.** Influence of published range of permittivities on recruitment (REC).

5 mA pulses the time constant changed from  $408 \mu s$  to  $433 \mu s$  (6%) when increasing the permittivity from  $1.2e5$  to  $25e5$ . However, the changes in recruitment due to the capacitive effects of the muscle are small compared to changes in recruitment caused by pulse duration or pulse amplitude changes.

Figure 7.1 also shows the recruitment-duration curve described by a FE model that uses Laplace's Equation (3.17) (static equation). It can be seen that the curves are nearly congruent with the curves obtained using the transient model considering the permittivities.

### 7.1.3. Discussion and Conclusions

The high variability of the electrical properties of the electrode-skin interface and the published bulk tissue capacitances were found to have a minor influence on recruitment in TES (Figure 7.1). Therefore, the capacitive effects can be neglected, which is equivalent to setting the time derivative term in equation (3.16) to zero which yields the Laplace equation. However, a dynamic model is necessary for the following cases:

- Investigations of time dependent voltage drops in the skin layer (which have a slow rise time): Such investigations are relevant if new pulse stimulation technologies, as for example presented in [JM05], are developed. For such cases a transient model allows one to optimize the power consumption because both the time dependent currents and the time dependent voltages can be simulated ( $P(t) = U(t) * I(t)$ ).
- Investigation of voltage regulated stimulation: It is important to note that only a transient simulation is able to produce reasonable values for the extracellular potential at the axon for voltage



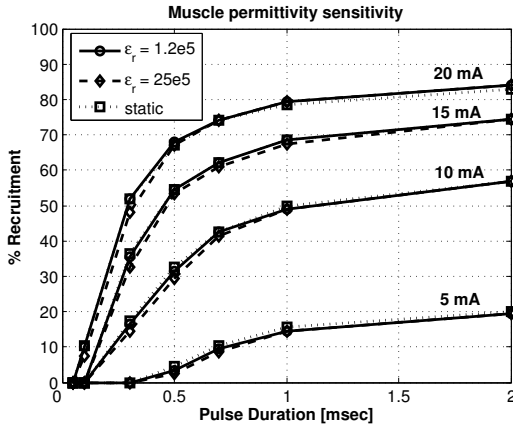


**Figure 7.1.** Recruitment-duration curves for different pulse amplitudes and the minimal and the maximal muscle permittivity (Table 3.3). Also shown are recruitment-duration curves calculated with a model using Laplace’s Equation (3.16) (static equation). The changes produced by the capacitance (permittivity) are seen to be small.

regulated stimulation. The voltage drop in the skin layer increases over time because of the high skin capacitance [DR99] and thus the extracellular potential at the nerve significantly drops during the applied course of the pulse. This was also depicted in Figure 3.4.

## 7.2. Tissue Resistivities

### 7.2.1. Non-linearity of Skin Resistance

In applications where surface electrodes are used for ES (e.g. rehabilitation of stroke subjects, sports, ...) the electrical impedance of the skin influences the electrical potential distribution. The knowledge of the electrical tissue properties of the skin is important for the design of electrical stimulators because it influences the maximally required power and it is also fundamental for TES models in order to accurately describe the potential distribution and nerve activation. It is known that the skin impedance is a nonlinear function of the current density

[Lyk71, YY81]. However, in the combined TES model (section 3.3) and in models described in literature (section 1.2) the skin is modeled with constant resistivity neglecting the non-linearity of the skin. In this section it is quantified how much the non-linear skin properties influence nerve activation in order to accept or reject the use of a constant skin resistivity in models.

The non-linear skin resistivities were measured in humans for current densities up to  $5 \text{ mA/cm}^2$  [DR99]. For large electrodes (e.g.  $5 \times 5 \text{ cm}^2$ ) such current densities are sufficient. However, when using smaller electrodes (e.g., on array electrodes) higher current densities can be required. We performed experimental measurements on human volunteers in order to obtain skin resistivities also at higher current densities (up to  $15 \text{ mA/cm}^2$ ).

In vivo the skin resistivity cannot directly be measured. A way to obtain the skin resistivity is by using an equivalent network model which is tuned to give the measured current-voltage response [vB77, Lyk71]. Such a network model (see Figure 7.2) consists of a capacitor  $C_{skin}$  in parallel with a resistor  $R_{skin}$  representing the skin and a series resistor for the plain resistive part (fat, muscle). Polarization voltage  $C_{Pol}$  and interface resistance  $R_{Pol}$  from the electrode skin interface can be neglected in surface electrical stimulation [DR99].

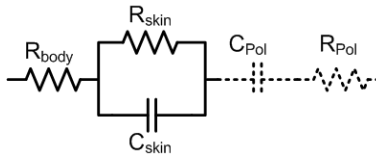


**Figure 7.2.** Equivalent circuit to model skin ( $R_{skin}$ ,  $C_{skin}$ ) and deep tissues ( $R_{body}$ ).  $C_{Pol}$  and  $R_{Pol}$  can be neglected in transcutaneous electrical stimulation [DR99].

### 7.2.1.1. Methods

**Measurements** Experimental measurements were undertaken in three female and four male volunteers with surface self adhesive electrodes ( $5 \times 5 \text{ cm}^2$ ) and a current regulated electrical stimulator [KPPM02]. A long pulse duration of 5 ms was applied in order to see the capacitive charging of the skin. The voltage  $V_{tot}$  (compare to Figure

3.4) was recorded using a digital oscilloscope. The stationary value of the capacitive charging of  $V_{tot}$  is denoted  $\overline{V_{tot}}$ .  $R_{skin}$  was then obtained using equation  $R_{skin} = \frac{\overline{V_{tot}} - V_{body}}{I_{stim}}$  where  $I_{stim}$  is the stimulation amplitude ( $V_{body}$  is the voltage across  $R_{body}$ ). To obtain the non-linear relationship between the skin resistance and the current amplitude the skin resistance  $R_{skin}$  was calculated at different current amplitudes. From the skin resistance  $R_{skin}$  the skin resistivity  $\rho_{skin}$  can be calculated by assuming a certain thickness of the skin using  $\rho_{skin} = \frac{R_{skin} * A_{elec}}{d_{skin}}$  where  $A_{elec}$  is the electrode area and  $d_{skin}$  is the skin thickness. A skin thickness of 1.5 mm was assumed. This agrees with mean values of human forearms (see Table 3.2 [Sta05]).

**Simulations** The same TES model and parameters as described in section 7.1.1 were used.

The non-linearity of the skin was incorporated into the model by applying the maximal range of measured skin resistivity values to the model and by comparing the resulting nerve activations. This yielded the maximal error that can be expected when neglecting the non-linearity of the skin resistivity. In order to quantify the error, the current amplitude to stimulate an axon at a certain depth  $I^{th}(L, D)$  (see section 3.4.2.3) was calculated for the maximal ( $16.78 k\Omega m$ ) and minimal ( $585 \Omega m$ ) skin resistivity obtained from experiments.

### 7.2.1.2. Results

**Measurements** The dependence of the skin resistance on the current density is depicted in Figure 7.3. The charts show the mean and standard deviation amongst the 7 human volunteers. The resistance starts at high values for low current densities and becomes smaller for higher densities. The found resistivities for different current densities are in agreement with other experimental publications [Lyk71, DR99].

**Simulations** The maximal range of skin resistivities obtained experimentally was applied to the TES model. For the maximal resistivity ( $16.78 k\Omega m$ )  $I^{th}(0.2 cm, 11 \mu m)$  was 19.8525 mA and  $I^{th}(1.6 cm, 11 \mu m)$  was 43.8139 mA. For the minimal resistivity ( $585 \Omega m$ )  $I^{th}(0.2 cm, 11 \mu m)$  was 19.8541 mA and  $I^{th}(1.6 cm, 11 \mu m)$  was 43.8268 mA. Expressing this influence of the skin resistivity in percentages yields values below 0.01%. This demonstrates that nerve activation is very similar whether the non-linearity of the skin resistivity is considered or not.

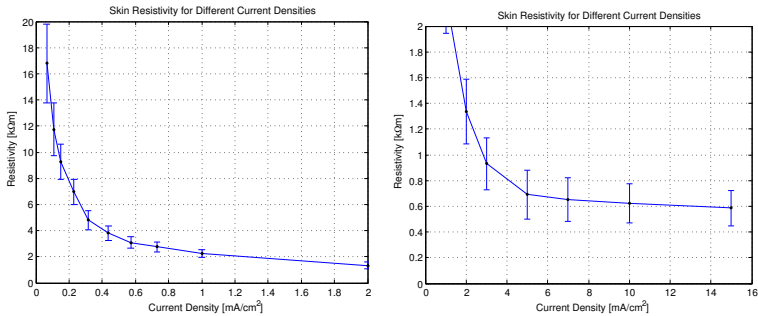


**Figure 7.3.** Non-linear behavior of skin resistivity versus the current density measured experimentally on 7 human volunteers. Two charts are provided for visual clarity where the left one shows the skin resistivity for low current densities and the right one for high current densities.

### 7.2.1.3. Discussion and Conclusions

The influence of the skin non-linearity on a TES simulation was investigated. It was found that the non-linearity of the skin resistivity can be neglected if only nerve activation is of interest. However, if the voltage on the electrodes is also of importance the non-linearity of the skin has to be incorporated (e.g., voltage regulated stimulation, see Figure 3.4 and the Discussion of section 7.1).

## 7.2.2. Common Resistivity Changes

In this section the impact of the tissues' resistivity variability that can be expected in humans on nerve activation is analyzed. These resistivity changes are investigated for two reasons: They give information about the influence of the biological diversity on electrical stimulation and also establish the sensitivities of the model for different parameters.

### 7.2.2.1. Methods

The parameters that were used for the TES model (section 3.3) are summarized in the tree structure below.

FE model	
└─	Geometry .....cylindrical geometry
└─┬─	Tissue thicknesses .....standard values from Table 3.2
└─┬─	Tissue properties .....standard values from Table 3.3
└─┬─	Electrode type ..... single electrodes
└─┬─┬─	Electrode sizes ..... $3 \times 3 \text{ cm}^2$
└─┬─┬─	Electrode distance ..... 11 cm
└─	Equation .....static equation (3.17)
└─	Stimulation pulse .....monopolar current regulated
└─┬─	Amplitude ..... 5 mA - 20 mA
└─┬─	Duration ..... 0.05 ms - 2 ms
Nerve model	
└─	Model ID ..... D (Table 3.4)
└─	Type ..... multiple nerve bundles (see Figure 3.7)
└─	Axon diameter .....bimodal with peaks at $6 \mu\text{m}$ and $13 \mu\text{m}$
└─	Axon depth .....0.2 cm - 1.1 cm

Laplace’s equation was employed to describe the static potential distribution because it was shown in section 7.1 that the capacitive effects can be neglected. Individual tissue resistivities were adapted in order to investigate the influence of resistivity changes on nerve activation. The resistivities were set to the maximal and minimal published values given in Table 3.3 and  $\pm 10\%$  changes from the values in Table 3.2 were used in order to obtain the sensitivities. In order to quantify the influence of resistivity variations, the current to stimulate a certain depth  $I^{th}(L, D)$  (section 3.4.2.3), the selectivity SEL (section 3.4.2.4), and the chronaxie 2.2.5 were calculated.

### 7.2.2.2. Results

The influence of the tissue resistivities on nerve activation was investigated. Table 7.3 shows the simulation results for the maximal range of resistivities and Table 7.4 for the  $\pm 10\%$  resistivity changes. The second row of the tables (*italic numbers*) contains the simulation results when parameters of Table 3.3 were used. Below the calculated values are shown for changes in the specified tissue resistivity for minimal and maximal resistivity (or 10% changes). The percentage values are relative changes to the value calculated using standard values.

The influence of resistivity changes on the selectivity and the chronaxie are little ( $< 2\%$ ). Only threshold current  $I^{th}(0.1 \text{ cm}, 11 \mu\text{m})$  for changes in the muscle resistivity were larger. The resistivity of the muscle di-

rectly influences the nerves' extracellular potential and showed therefore the biggest sensitivity.

Threshold current  $I^{th}(L, D)$  was also calculated for deeper nerves but the results are very similar to the ones depicted in the two Tables (7.3 and 7.4) and are therefore not shown.

### 7.2.2.3. Discussion and Conclusions

The skin and fat resistivities were found to have a little influence on nerve activation (Table 7.3). The main reason for the observed little influence is the perpendicular current flow through the skin and fat layers which is caused by the higher resistivities (of skin and fat compared to muscle) in those layers. A change of the skin or fat layer resistivity only changes the voltage drop within the layer but not the current distribution in the underlying muscle layer. As a consequence, changes of the skin and fat resistivities have only a minor influence on nerve activation when using current-regulated TES. This is an advantage for the practical application of current regulated TES, because similar stimulation parameters can be used for different persons. Changes in muscle resistivity had the largest influence on nerve activation (Table 7.3). This was expected because a change of the muscle resistivity directly affects the axons' extracellular potential.

## 7.3. Detailed Anatomical Model (Segmentation from MRI)

The goal of this section is to find out whether anatomically based volume conductor models are necessary to describe nerve activation in TES or if the use of geometrical approximations (e.g. cylindrical) is sufficient.

Often simplified geometries are used to describe the complex human anatomy [LEM00, LEM01, TNK07]. However, advanced modeling techniques allow the inclusion of more and more anatomical details into volume conductor models. Reichel et al. investigated the stimulation of denervated muscles and developed models of the human thigh. First they used 2D models [RMR99] and later 3D models [RBMR02, MRRM04] to predict supra-threshold regions within the muscle. McIntyre et al. used a 3D volume conductor model of the spinal cord [MG02] to find optimal waveforms for stimulation. The anatomically accurate representation of the spinal cord was found to be impor-

Parameter	Variation	$I^{th}(0.1cm, 11um)$ [mA]	SEL at $I^{th}(1.1cm, 11um)$	$T_{ch}$ for $L=0.1$ [ $\mu s$ ]			
<i>Using standard parameters</i>							
		<i>5.378</i>	<i>32.928</i>	<i>444.577</i>			
Electrode-skin interface (standard: 300 $\Omega m$ )	min (1 $\Omega m$ )	11.328	110.63%	27.435	-16.68%	410.793	-7.60%
	max (10000 $\Omega m$ )	4.623	-14.05%	34.329	4.25%	435.100	-2.13%
Skin	min (500 $\Omega m$ )	5.378	0.00%	32.928	0.00%	444.577	0.00%
	max (6000 $\Omega m$ )	5.378	0.00%	32.928	0.00%	444.577	0.00%
Fat	min (10 $\Omega m$ )	5.384	0.10%	32.907	-0.06%	443.669	-0.20%
	max (600 $\Omega m$ )	5.375	-0.06%	32.942	0.04%	444.326	-0.06%
Muscle	min (2 $\Omega m$ )	7.735	43.82%	33.172	0.74%	443.813	-0.17%
	max (5 $\Omega m$ )	3.490	-35.10%	32.523	-1.23%	445.427	0.19%
Cortical bone	min (40 $\Omega m$ )	5.328	-0.92%	32.388	-1.64%	442.352	-0.50%
	max (60 $\Omega m$ )	5.449	1.32%	32.758	-0.52%	443.401	-0.26%
Bone marrow	min (10 $\Omega m$ )	5.461	1.55%	32.824	-0.32%	442.573	-0.45%
	max (15 $\Omega m$ )	5.339	-0.72%	32.278	-1.97%	442.463	-0.48%

**Table 7.3.** Current to stimulate certain depth, selectivity, and chronaxie were calculated for the range of published resistivities (see Table 3.3). The second row (*italic numbers*) contains the simulation results when standard parameters were used. The percentage numbers are relative changes to the values calculated using standard parameters.

Parameter	Variation	$I^{th}(0.1cm, 11um)$ [mA]	SEL at $I^{th}(1.1cm, 11um)$	$T_{ch}$ for $L=0.1$ [ $\mu s$ ]
<i>Using standard parameters</i>				
		5.378	32.928	444.577
Electrode-skin interface (standard: 300 $\Omega m$ )	-10%	5.453	32.806	442.173
	+10%	5.314	33.043	440.857
Skin (standard: 700 $\Omega m$ )	-10%	5.378	32.928	444.577
	+10%	5.378	32.928	444.577
Fat (standard: 33 $\Omega m$ )	-10%	5.378	32.926	444.363
	+10%	5.378	32.928	444.577
Muscle (standard: 3 $\Omega m$ )	-10%	5.902	33.003	442.364
	+10%	4.949	32.863	445.050
Cortical bone (standard: 50 $\Omega m$ )	-10%	5.350	33.020	441.609
	+10%	5.411	32.840	444.918
Bone marrow (standard: 12.5 $\Omega m$ )	-10%	5.412	32.889	442.856
	+10%	5.355	32.964	446.242

**Table 7.4.** Current to stimulate certain depth, selectivity, and chronaxie were calculated for 10% changes of the resistivities. The second row (italic numbers) contains the simulation results when standard parameters (Table 3.3) were used. The percentage numbers are relative changes to the values calculated using standard parameters.



tant. Lowery et al. [LSDK04] developed an anatomically based model of the upper arm to investigate features of surface EMG signals. The validation of her model was done by using electrical stimulation and is therefore mentioned here. A main result in Lowery's publication was that a cylindrical representation of the upper arm is sufficient to describe the surface EMG signal. These two examples of Reichel et al. and Lowery et al. show that it is anatomy and application dependent if the geometry can be simplified or if the additional effort of constructing anatomically based geometries is required. In this section it is investigated if anatomically based geometries are required in a TES model. Three forearm geometries were constructed based on MRI scans of three volunteers. Simulated nerve activation in the anatomically based geometries was compared with simulated nerve activation in cylindrical models.

### 7.3.1. Methods

**Anatomically based geometry** MRI scans of the forearms of three volunteers (two male and one female) were carried out with a Philips 1.5T scanner. The resolution of the acquired images was 0.5 mm. Three realistic model geometries were built from these MRI scans by segmenting the different tissue structures (skin, fat, muscle, cortical bone, and bone marrow). For the segmentation the MRI slices were loaded into the software package Amira (Visage Imaging Inc., Carlsbad, CA USA). Automatic segmentation worked for the high contrast regions (bones), however manual segmentation had to be used to segment all regions correctly. After the segmentation the contour lines of each MRI slice were imported into Rhinoceros (Robert McNeel & Associates, Seattle, WA USA), where for each tissue type a closed geometric volume model was built using the "lofting"-technique (consult Rhinoceros manual). The volumes were exported to ACIS-files (.sat) that were then imported into ANSYS (EMAG, Ansys Inc., Canonsburg, PA). ANSYS created the FE mesh (Figure 7.4).

The thin skin layer was not segmented from the MRI scans because the contrast was poor (due to the low water content) and the accuracy would have been unsatisfactory. Instead a constant 1.5 mm layer covering the fat layer was added in Rhinoceros. This procedure can be justified with the simulation results where it was observed that skin thicknesses of 1 mm - 3 mm have only a small influence on nerve activation (see section 7.5).

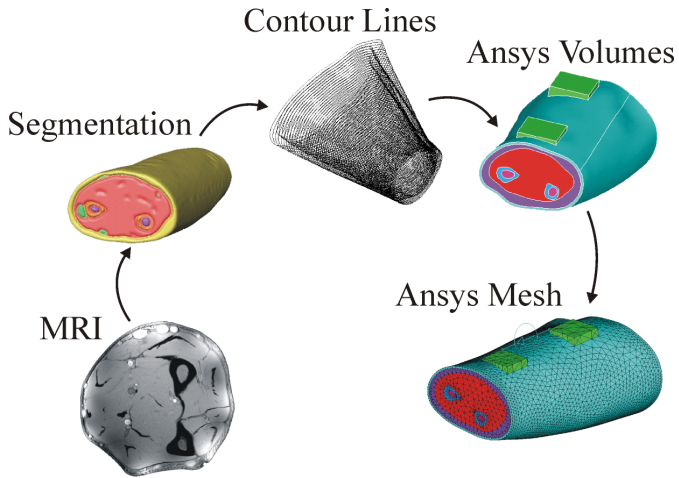


**Figure 7.4.** Shows the process from MRI scan to FE model (MRI, segmentation, contour lines, parameterized volume model with added stimulation electrodes, meshed geometry).

Two stimulation electrodes ( $2.5 \times 2.5 \text{ cm}^2$ ) were placed on the skin layer using the CAD software SolidWorks (SolidWorks Corporation, Concord, MA USA). Afterwards the volumes (including the electrodes) were imported into ANSYS. The size of the electrodes and the distance between the electrodes was chosen the same as for the cylindrical model.

**Cylindrical geometry** For the multiple layer cylindrical geometry (section 3.1.5.1) the standard thicknesses from Table 3.2 were used. Only the fat layer was adjusted to the mean fat thickness of the anatomically based models in order to compare the anatomically based geometries with the cylindrical geometry. The mean fat thickness in the anatomically based models was measured under the area covered by the cathode using custom software that was developed using VTK (Kitware Inc., NY). The mean thickness was the distance between the skin-fat interface and the fat-muscle interface. The mean fat thicknesses were 3.7 mm (volunteer 1), 1.5 mm (volunteer 2), and 2.3 mm (volunteer 3). The mean of those three values (2.5 mm) was used as fat thickness in the cylindrical geometry.

**Calculation of Nerve Activation** Nerve activation was calculated using the TES model introduced in section 3.3 with the parameters that are summarized in the tree structure below.

FE model	
└─ Geometry .....	anatomical and cylindrical geometry
└─ Tissue thicknesses .....	standard values from Table 3.2
└─ Tissue properties .....	standard values from Table 3.3
└─ Electrode type .....	single electrodes
└─ Electrode sizes .....	$3 \times 3 \text{ cm}^2$
└─ Electrode distance .....	11 cm
└─ Equation .....	static equation (3.17)
└─ Stimulation pulse .....	monopolar current regulated
└─ Amplitude .....	30 mA
└─ Duration .....	$300 \mu\text{s}$
Nerve model	
└─ Model ID .....	AF (Table 3.4)

In order to compare nerve activation in the anatomical model with nerve activation in the cylindrical model AFs (section 3.2.1.2) and activation volumes (section 3.4.2.1) were calculated.

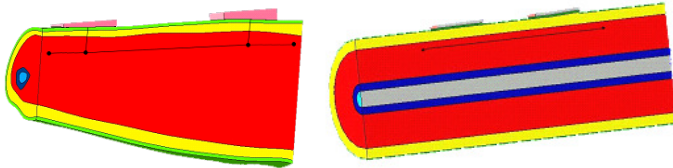


**Figure 7.5.** The interpolation line along which the AF was calculated in all three anatomical models was placed 0.5 cm below the fat/muscle interface.

In order to allow the comparison of the activation volumes of the anatomical geometries with the cylindrical geometry, a transformation between the geometries was required. Activation underneath the cathode was of interest. The transformation to make the cathode of the anatomical geometry congruent with the cathode of the cylindrical geometry was determined and applied in VTK (Kitware Inc., NY) (see Figure 7.8). Activation volumes calculated using the anatomical geometry were compared to activation volumes calculated using the cylindri-

cal geometry with mean distances which are calculated in the following way. Distances between two activation volumes are calculated by intersecting the surface normal vectors of one surface with the second surface (Figure 7.6). The distances between the base points of the normal vectors and the intersections were averaged and denoted mean distance. The activation volumes were produced for the thickest axon diameter

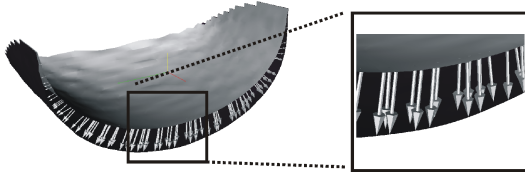


**Figure 7.6.** Two surfaces representing the boundary of two activation volumes and the distance vectors between the two surfaces indicated by arrows. The mean of all distance vectors is defined as mean distance (MD).

of  $16\ \mu\text{m}$  what corresponds to motor threshold activation (Figure 2.6) (see section 4.3.1.1 or [RHK<sup>+</sup>94, PF07]).

### 7.3.2. Results

**AF** The AFs along the modeled nerve line under the cathodes are shown in Figure 7.7. Amongst the anatomically based models the maximal variation was 20.4%. Volunteer 1 had the thickest fat layer (3.7 mm) and the lowest activation in the simulation, volunteer 2 had the thinnest fat layer and the highest activation in the simulation, and volunteer 3 was in between with both the fat thickness and the activation. This indicates that thicker fat layers result in lower values of the AF.

The cylindrical geometry was generated using the mean fat thickness of all anatomical models. The mean of the peak values of the AFs simulated using the anatomical models is 1.029 (Figure 7.7) and the peak AF simulated using the cylindrical geometry was normalized to 1. The difference between the anatomical geometry and the cylindrical geometry was therefore 2.9%. This shows that the peak AFs of anatomical models and cylindrical models are similar and that it is therefore valid to replace anatomical models with cylindrical models.

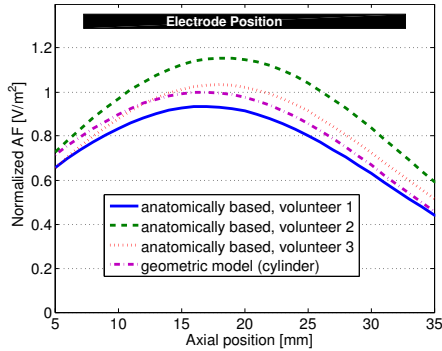


**Figure 7.7.** Comparison of the AF calculated using the three anatomical (MRI) models with the AF calculated using the cylindrical geometry.

**Activation volume (AV)** The sizes of the three activation volumes that were calculated using the anatomical geometries were compared with each other. Mean distances between two activation volumes were calculated for the three possible combinations. These mean distances are  $-0.7 \pm 1 \text{ mm}$ ,  $-0.5 \pm 0.9 \text{ mm}$ , and  $-1.1 \pm 0.8 \text{ mm}$ . These calculations show that the simulated activation volumes of the different anatomical models are very similar.

The three activation volumes of the anatomical models were also compared with the activation volume of the cylindrical model. The mean distances were  $-0.5 \pm 0.5 \text{ mm}$ ,  $-0.6 \pm 1 \text{ mm}$ , and  $0.1 \pm 0.4 \text{ mm}$ . Detailed results of the activation volumes that compared the worst ( $-0.6 \pm 1 \text{ mm}$ ) are depicted in Figure 7.8. The top right picture shows the activation volume (blue) of the anatomical geometry (volunteer 2) and the activation volume (white) of the cylindrical geometry. The plot at the bottom of Figure 7.8 shows the histogram of the distances between the blue and the white activation volume (see also Figure 7.6). Most distances are less than 2.5 mm what is small compared to the size of the two activation volumes ( $50 \times 20 \times 33 \text{ mm}^3$ ). This indicates that activation volumes produced using a cylindrical geometry are very similar to activation volumes produced using anatomical geometries.

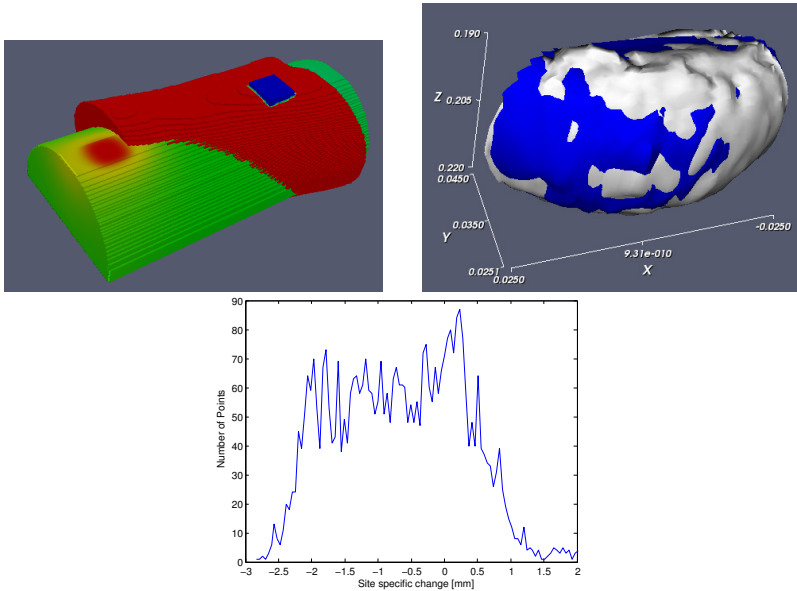


**Figure 7.8.** Comparison of the activation volume calculated using anatomically based (MRI) geometry (volunteer 2) with an activation volume calculated using the cylindrical geometry. Upper left image depicts the overlaid two geometries (red: anatomically based geometry, green: cylindrical geometry). Upper right image shows the two activation volumes (blue: anatomically based, white: cylindrical), and the bottom chart shows the histogram of the distances between the two activation volumes (compare to Figure 7.6).

### 7.3.3. Discussion and Conclusions

An anatomical geometry was built using MRI scans. The main human tissue layers (skin, fat, muscle, cortical bone, bone marrow) were included in the anatomical geometry but no small inhomogeneities. One reason is that small structures are not visible on MRI scans and furthermore the meshing is currently not possible for too detailed structures due to computational limitations. For example, tendons that are visible in the MRI scans were segmented but had to be removed prior to meshing because mesh generation in ANSYS was not possible. However, the investigation of bone to nerve distances and inhomogeneity to

nerve distances in the following section (7.4) shows that such structures have to be close to the nerve to have a significant influence on nerve activation.

The results show that when the fat thickness of a cylindrical geometry is adapted to the mean fat thickness of an anatomically based model the resulting AFs are very similar (2.9% difference). Hence, the influence of varying layer thicknesses within one geometry that is introduced with the anatomically based geometry and the non-cylindrical shape have a minor influence on nerve activation. In summary, the obtained results show that multiple layer cylindrical geometries can be used to describe nerve activation during TES in human forearms when the thickness of the fat layer is adapted accordingly.

## 7.4. Bone Position and other Inhomogeneities

The close vicinity of bones or other inhomogeneities (such as blood vessels or tendons) to nerves may have an influence on nerve activation during TES. In this section different sizes and types of inhomogeneities at different distances from nerves are investigated using the TES model.

### 7.4.1. Methods

For the computer simulations the model that is described in section 7.2.2.1 was used with standard parameters for tissue thicknesses and properties (Tables 3.2 and 3.3). The influence of inhomogeneities on an axon that was placed at a depth of 0.1 cm from the fat-muscle interface was investigated. In order to quantify this influence, the current  $I^{th}(0.1\text{ cm}, 11\ \mu\text{m})$  to stimulate this axon (section 3.4.2.3) was calculated.

#### 7.4.1.1. Bone Distance

In order to observe the influence of bones on nerve activation the bone that is located in the center of the cylinder was moved towards the axon.  $I^{th}(0.1\text{ cm}, 11\ \mu\text{m})$  was calculated for different distances between the axon and the bone.

#### 7.4.1.2. General Inhomogeneity

The influence of other inhomogeneities such as blood vessels, tendons, or interstitial fluids was covered by adding a cylindrical inhomogene-

ity in different distances from the axon (see Figure 7.9). Two sizes of inhomogeneities were added to the geometries. A smaller one with length 5 mm and diameter 2 mm, and a larger one with length 10 mm and diameter 5 mm. The resistivity of the inhomogeneity was changed to model tissues that have a larger or smaller resistivity compared to muscle. A lower resistivity models for example blood vessels or interstitial fluids ( $1 \Omega m$ ) and larger resistivities model tendons ( $10 \Omega m$ ) or bony structures ( $50 \Omega m$ ). The values of the resistivities were taken from Gabriel et al. [GLG96].

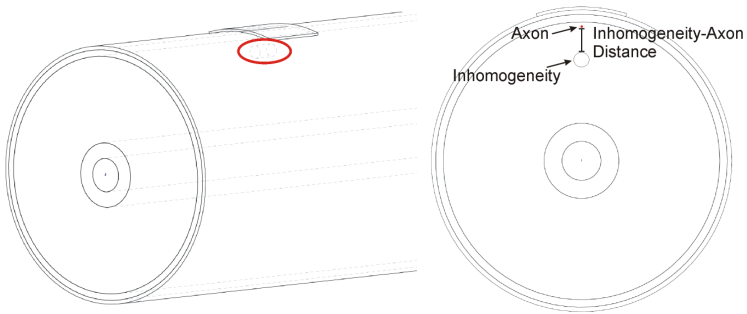


**Figure 7.9.** An inhomogeneity was added to the cylindrical geometry.

## 7.4.2. Results

### 7.4.2.1. Bone Distance

$I^{th}(0.1 \text{ cm}, 11 \mu m)$  for different bone-axon distances is shown in Figure 7.10. The influence of the bone on nerve activation is below 10% for distances above 0.8 cm.

### 7.4.2.2. General Inhomogeneity

$I^{th}(0.1 \text{ cm}, 11 \mu m)$  for different inhomogeneity-axon distances is depicted in Figure 7.11. The results show that a higher stimulation current is required for resistivities that are below the muscle resistivity and a lower stimulation current for inhomogeneities with a resistivity above muscle resistivity. For the larger inhomogeneity the distance from the axon has to be at least 0.5 cm so that the influence is below 10% (Figure



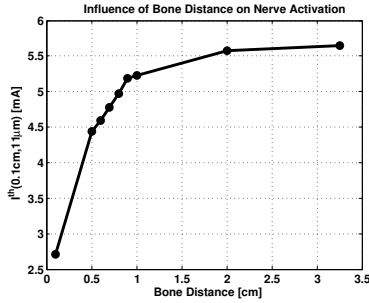


**Figure 7.10.** Current required to stimulate a certain axon ( $I^{th}(0.1 \text{ cm}, 11 \mu\text{m})$ ) versus the bone to axon distance.

7.11(a)). For the smaller inhomogeneity the influence was below 10% for distances around 0.2 cm to 0.3 cm (Figure 7.11(b)).

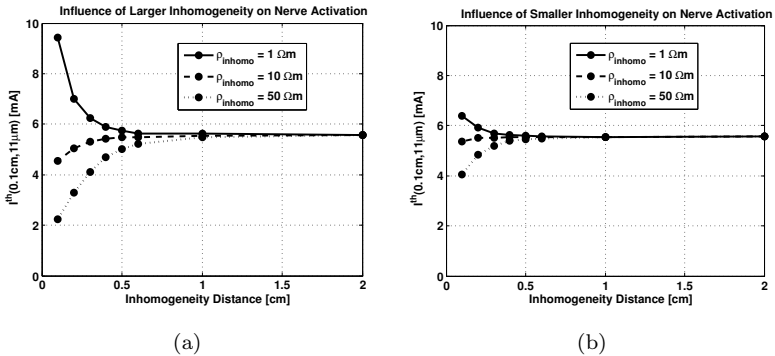


**Figure 7.11.** Current required to stimulate a certain axon ( $I^{th}(0.1 \text{ cm}, 11 \mu\text{m})$ ) is plotted against the distance from the inhomogeneity. Two sizes of inhomogeneities were investigated (7.11(a): length 10 mm, diameter 5 mm; 7.11(b): length 5 mm, diameter 2 mm) for different resistivities of the inhomogeneities.

### 7.4.3. Discussion and Conclusions

The results show that for transcutaneous electrical stimulation the influence of bone and other inhomogeneities on nerve activation is small if there is at least a distance of 0.8 cm for large inhomogeneities (1 cm diameter) and a distance of 0.3 cm for small inhomogeneities (0.2 cm diameter) between nerve and inhomogeneity. This result helps to decide which inhomogeneities can be neglected in TES models.

## 7.5. Tissue Layer Thicknesses

The tissue thicknesses in humans can vary largely what can have a substantial impact on TES. It is for example generally known that fatter people require higher current amplitudes to generate similar activation as thinner people. In this section the influence of changing tissue layer thicknesses on nerve activation is systematically quantified.

### 7.5.1. Methods

For the assessment of the tissue thicknesses the same model as described in section 7.2.2.1 was used. For the resistivities the standard values from Table 3.3 were used and the tissue layer thicknesses were changed in the range of values that covers a large part of the variation found in humans (Table 3.2). Also the sensitivities for 10% changes of the tissue thicknesses were calculated.

### 7.5.2. Results and Conclusions

The influence of the tissue thicknesses on  $I_{th}(0.1\text{ cm}, 11\mu\text{m})$  is below 7.5% for skin, muscle, cortical bone, and bone marrow (see Tables 7.5 and 7.6). The influence of the range of fat thicknesses found in humans is much larger (468%). It will be shown in the following section 7.6 that the main reason for this increase is the larger distance between electrode and axon.

The selectivity was influenced mainly by the fat and the muscle thicknesses (see Tables 7.5 and 7.6). Larger fat layers decrease the selectivity due to the spread of the current in the larger fat layer. Thicker muscles have mainly an influence on the diameter of the arm. In a thinner arm the selectivity is higher because the volume  $V_{AV}$  in Equation (3.33) is smaller.

The influence of the tissue thicknesses on the chronaxie was generally low (see Tables 7.5 and 7.6). The largest influence was found with the large fat thickness (6.32%). The reason is the spreading of the current in the thicker fat layer. As a consequence the activation field is broader at the axon and more nodes are activated simultaneously. This causes the chronaxie values to increase. This effect is discussed in more detail in section 12.1.

## 7.6. Nerve Depth and Axon Diameter

In this section the relation between nerve activation, nerve depth, and axon diameter is analyzed. For point sources with an electrode-axon distance up to 0.8 cm that relation is well documented [RB87, Gri99, Rat08]. However, for larger electrodes that are further away from the nerves the relation has not been investigated. The combined TES model (section 3.3) was used in order to calculate the threshold axon activation for different nerve depths and axon diameters. The aim of this section is to provide quantitative values for the influence of the nerve depth and the axon diameter on nerve activation in order to find the parameters that have the largest influence on TES (section 9). Furthermore, it can be shown whether point sources are applicable to describe TES.

### 7.6.1. Methods

For the assessment of the nerve depths (electrode-axon distance) and the axon diameters the same model as described in section 7.2.2.1 was used. For the resistivities and the tissue thicknesses the standard values from Tables 3.3 and 3.2 were used. Square electrodes with sizes of  $3 \times 3 \text{ cm}^2$  and electrode-axon distances between 0.5 cm and 2.9 cm were investigated. Electrode-axon distances were chosen such that the range of expected nerve positions in human arms are covered ([Sta05]). Additionally an electrode size of  $0.1 \times 0.1 \text{ cm}^2$  served as a point source model in order to compare the results with results in literature using point sources [RB87, Gri99, Rat08].

### 7.6.2. Results

The simulation results in Figure 7.12(a) show the activation thresholds of axons in different depths and with different diameters, from which the recruitment of nerve bundles in different depths can be predicted. If it is for example known that a target recruitment of  $\sim 50\%$  (in our

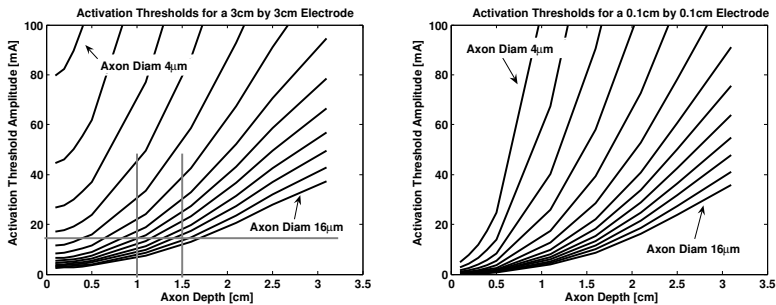
Parameter	Variation	$I^{th}(0.1cm, 1lum)$ [mA]	SEL at $I^{th}(1.1cm, 1lum)$	$T_{ch}$ for $L=0.1$ [ $\mu s$ ]	
<i>Using standard parameters</i>					
		<i>5.378</i>	<i>32.928</i>	<i>444.577</i>	
Electrode-skin interface (standard: 1 mm)	min (0.5 mm)	5.972	1.04%	32.066	445.185
	max (2 mm)	5.020	-6.65%	33.536	442.065
Skin (standard: 1.5 mm)	min (1 mm)	5.347	-0.57%	32.315	440.85
	max (3 mm)	5.780	7.48%	33.275	442.978
Fat (standard: 2.5 mm)	min (2 mm)	5.481	1.92%	32.571	439.578
	max (30 mm)	30.524	467.58%	27.979	472.691
Muscle (standard: 33.5 mm)	min (20 mm)	4.989	-7.23%	50.437	444.218
	max (60 mm)	5.696	5.91%	23.254	442.019
Cortical bone (standard: 6 mm)	min (4 mm)	5.346	-0.59%	33.175	444.444
	max (8 mm)	5.403	0.47%	33.165	444.662
Bone marrow (standard: 6.5 mm)	min (4 mm)	5.345	-0.61%	33.125	444.024
	max (8 mm)	5.398	0.37%	33.135	443.556

**Table 7.5.** Current to stimulate certain depth, selectivity, and chronaxie were calculated for the range of expected tissue thicknesses (see Table 3.2). The second row (*italic numbers*) contains the simulation results when standard parameters were used. The percentage numbers are relative changes to the values calculated using standard parameters.

Parameter	Variation	$I^{th}(0.1cm, 11um)$ [mA]	SEL at $I^{th}(1.1cm, 11um)$	$T_{ch}$ for $L=0.1$ [ $\mu s$ ]	
<i>Using standard parameters</i>					
		<i>5.378</i>	<i>32.928</i>	<i>444.577</i>	
Electrode-skin interface (standard: 1 mm)	-10%	5.453	32.849	443.481	-0.25%
	10%	5.321	33.105	441.965	-0.59%
Skin (standard: 1.5 mm)	-10%	5.367	32.891	443.757	-0.18%
	10%	5.407	33.054	442.856	-0.39%
Fat (standard: 2.5 mm)	-10%	5.376	32.873	444.09	-0.11%
	10%	5.408	33.081	445.246	0.15%
Muscle (standard: 33.5 mm)	-10%	5.329	35.954	442.727	-0.42%
	10%	5.449	29.254	443.932	-0.15%
Cortical bone (standard: 6 mm)	-10%	5.354	33.163	442.131	-0.55%
	10%	5.391	33.078	442.64	-0.44%
Bone marrow (standard: 6.5 mm)	-10%	5.315	33.135	442.851	-0.39%
	10%	5.388	33.143	441.64	-0.66%

**Table 7.6.** Current to stimulate certain depth, selectivity, and chronaxie were calculated for 10% changes of the tissue thicknesses. The second row (*italic numbers*) contains the simulation results when standard parameters (Table 3.2) were used. The percentage numbers are relative changes to the values calculated using standard parameters.

model a nerve diameter down to  $11\ \mu\text{m}$  activated) of a nerve in 1 cm depth is stimulated the co-activation of axon in other depths can be predicted. For example at 1.5 cm depth  $15\ \mu\text{m}$  axons will be activated but not  $14\ \mu\text{m}$  axons (see horizontal line indicated in Figure 7.12(a)). Figure 7.12(b) contains the simulation results of the model using small  $0.1\times 0.1\ \text{cm}^2$  stimulation electrodes. By comparing these curves with the results produced using the  $3\times 3\ \text{cm}^2$  electrodes (Figure 7.12(a)) it can be seen that at superficial depths ( $<1\ \text{cm}$ ) the activation thresholds for different axon diameters are much closer together with the 'point'-electrode compared to the  $3\times 3\ \text{cm}^2$  electrode.



(a) Activation thresholds for different axon depths and axon diameters using a  $3\times 3\ \text{cm}^2$  electrode.

(b) Activation thresholds for different axon depths and axon diameters using a  $0.1\times 0.1\ \text{cm}^2$  electrode.

**Figure 7.12.** Activation thresholds for different axon depths and axon diameters.

### 7.6.3. Discussion and Conclusions

Nerve activation is strongly influenced by the axon depth and the axon diameter (Figures 7.12(a) and 7.12(b)). Amongst the influences that were investigated in this section the axon depth and the axon diameter have a strong influence on nerve activation. All influences are summarized and compared in chapter 9.

The comparison of the results in Figure 7.12(a) with the results in Figure 7.12(b) shows that activation thresholds have a different characteristic for different electrode sizes. This indicates that the electrode size is an important parameter in TES and has to be incorporated in

models describing TES. Point sources are in most cases not adequate to describe TES because nerve activation decreases differently with distance for different electrode sizes. The influence of different electrode sizes is further investigated in part IV.





# 8

## **Influence of Nerve Bundles on Extracellular Potential**

The axons that are stimulated during TES are gathered in nerve bundles. These nerve bundles are composed of different tissue types that might influence the electrical current flow and nerve activation during TES. Models of implantable systems take these tissues into account because they are known to influence activation when electrodes are close to the nerve bundle [LGD06, STT08]. The aim of this chapter is to analyze with a modeling approach if nerve bundles (inhomogeneous structures) influences individual axon activation when stimulated with TES.

## 8.1. Introduction

Peripheral nerve bundles have a complex anatomy [Sta05] and contain several fascicles each of which contains many axons (Figure 2.6). Each fascicle is surrounded by a thin perineurial layer and inside the fascicle the axons are embedded in connective tissues called endoneurium. The nerve bundle is surrounded by an encapsulating layer that is similar to the perineurial tissue [RACS98].

Volume conductor models are used to calculate the current and potential distribution inside human tissues when electrical currents are applied (chapter 3). Up to now the inhomogeneous structure of nerve bundles is not included in volume conductor models [MM08, Gri99, CS85]. Inhomogeneities are assumed to be negligible because nerve bundles are very thin [McN76]. However, this assumption has to be checked by including actual nerve bundles in the volume conductor model.

Selectivity is an important aspect in electrical stimulation to stimulate specific nerves and muscles. Selectivity can be assessed as the ratio of the amount of force generated at the target muscle compared to the co-contraction of other muscles [KLK07]. For implanted electrical stimulation there exist simulation studies for multi electrode cuff systems which aim at improving selectivity [LD04, YD05, CCD01]. These studies showed that specific axons within the whole nerve bundle can be stimulated and that the selectivity can be improved up to a certain point. They disproved earlier studies where it was stated that intrafascicular stimulation is needed in order to get good selectivity with multi electrode implanted systems [VvVS<sup>+</sup>89]. For transcutaneous electrical stimulation a selective stimulation of single axons in the nerve bundle is not possible because the electrode to nerve distance is too large in order to get a specific selective activation. However, it is important that as many fibers as possible that innervate the target muscle are activated and not only part of them (in order to achieve a strong force). Therefore, it was investigated how much the nerve activation changes when the position of the axon within the nerve bundle changes.

## 8.2. Methods

### 8.2.1. Finite Element Model

In order to investigate the influence of the different tissues in nerve bundles and axons on nerve activation two nerve geometries were built: A single axon and a nerve bundle, which are depicted with their dimen-

sions in Figure 8.1. The dimensions were taken from [RACS98] and [CCD01]. The single axon and the nerve bundle were embedded in a square muscle volume because the meshing of square geometries were more efficient compared to circular or other shapes. The 2D geometry shown in Figure 8.1 was meshed with a 2D 8-node-quadrilateral element and extruded to a 20-node-hexahedral element. The extruded models had a length of 10 cm (Figure 8.2). The surrounding material of the single axon and the nerve bundle had the properties of muscle (Table 3.3). The meshing of the geometry and the calculation of the potential distribution was performed with the FEM software Ansys (EMAG, Ansys Inc., Canonsburg, PA).

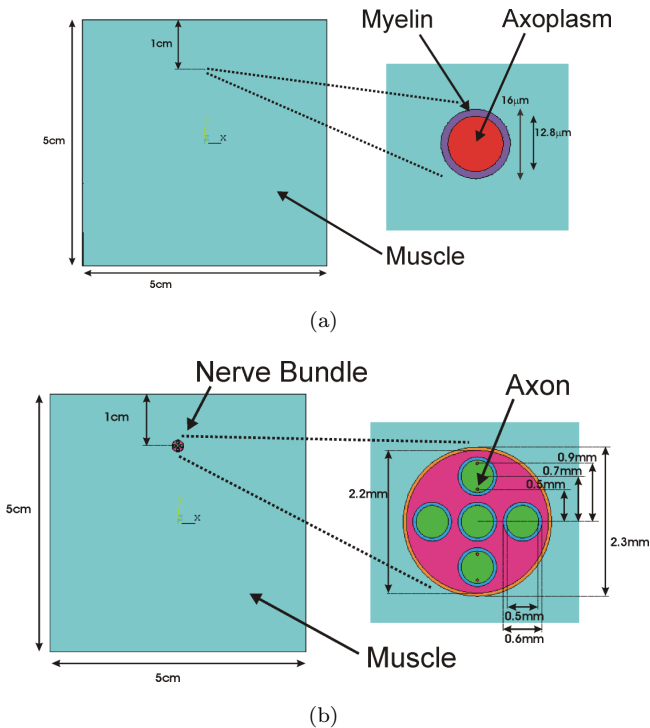


**Figure 8.1.** Geometry with dimensions of the single axon (8.1(a)) and the nerve bundle (8.1(b)).

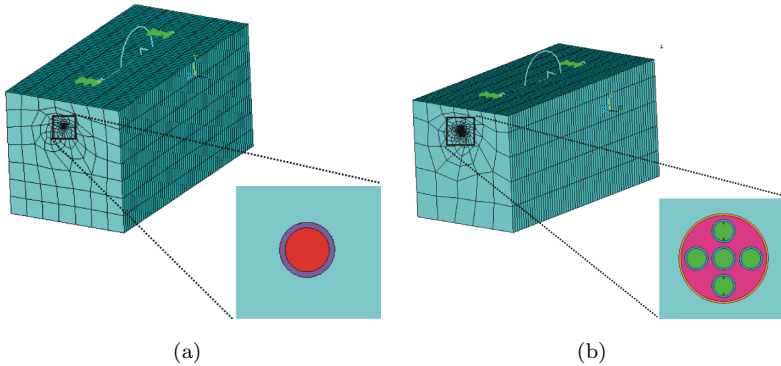


**Figure 8.2.** Meshed and extruded geometry for the single axon (8.2(a)) and the nerve bundle (8.2(b)) with surrounding muscle tissue and stimulation electrodes.

The single axon model consisted of axoplasm with a myelin layer (see Figure 8.3). The nodes of Ranvier were modeled by removing  $5\ \mu\text{m}$  of the myelin layer at a spacing of  $1.5\ \text{mm}$  (see Figure 8.3 and [Sta05]). This spacing corresponds to a motor axon with a large diameter of  $16\ \mu\text{m}$  ([MRG02]). The resistivities of the different materials that were used in the model are given in Table 8.1 and were taken from [CCD01].

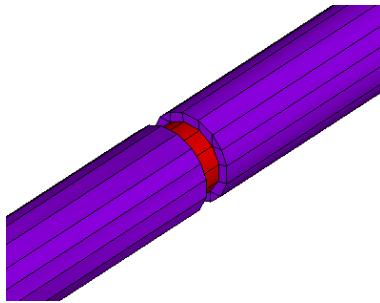


**Figure 8.3.** Image shows the axon model with node of Ranvier.

The nerve bundle model consisted of epineurium, perineurium, endoneurium, axoplasm and an encapsulating layer (membrane) that en-

Tissue	Resistivity [ $\Omega m$ ]
Myelin	33.3e3
Axoplasm	0.7

**Table 8.1.** Properties used for single axon.

Tissue	Resistivity [ $\Omega m$ ]
Axoplasm	0.7
Perineurium	478
Epineurium	12.11
Endoneurium	1.75
Encapsulating Layer	80

**Table 8.2.** Properties used for nerve bundle model.

closes the whole nerve bundle (Figure 8.4). The corresponding tissue resistivities are given in Table 8.2 (taken from [CCD01]). Four axons were placed within the endoneurium at different distances from the electrode (Figure 8.1). Only four axons were modeled because the number of FEs was too large to fill the whole fascicle with axons. The myelin layer which would enclose each axon was not included because the number of FEs was too large for reasonable simulation times and the influence is very small as will be shown using the single axon model.

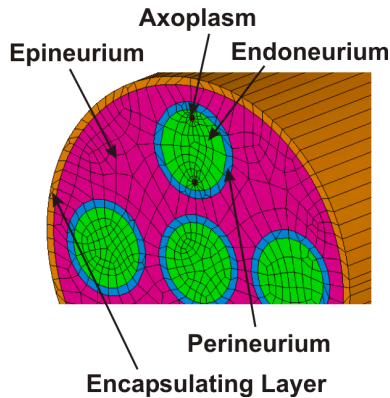


**Figure 8.4.** Nerve bundle with the terms for the different tissues.

Stimulation electrodes were added to the surrounding material (Figure 8.2) and had a size of 5 mm x 10 mm with an inter electrode spacing of 5.5 cm. The electrode size was chosen such that it covered multiple nodes of Ranvier. A constant current source was connected to the electrodes.

### 8.2.2. Nerve Model

The electrical potentials that were calculated using the FE model were interpolated on lines that were placed along the axons (on the electrode facing side) in order to obtain the axons' extracellular potentials. The potentials were then interpreted either directly, or the MRG axon model (model  $D$  or  $D^P$  in Table 3.4) was used to conclude from these extracellular potentials onto nerve activation (the TP). The linear axon model  $D^P$  was used in order to obtain quantitative measures and not only the all or nothing ('AP' and 'no AP') response that is obtained by the non-linear axon model  $D$ . The axon's TP was always monitored at the node underneath the cathode where maximal activation occurred because this is the place where an AP is first generated.

### 8.2.3. Influence of Single Axon on Extracellular Potential

The assumption that the axon does not influence the extracellular potential was investigated using the single axon model (Figure 8.1). The interpolation line in the FE model was placed at the border of the nerve ( $10\ \mu\text{m}$  from axon center; see Figure 8.1) in order to obtain the axons' extracellular potentials. Three different settings of the material properties were compared. First, the material properties of the axon were set to muscle. Second, the standard material properties for axoplasm with a myelin layer were used. Third, the axon model with added nodes of Ranvier was used.

### 8.2.4. Influence of a Nerve Bundle on the Axon's Extracellular Potential

The influence of the presence of a nerve bundle on the axons' extracellular potentials was investigated by comparing the results from models with tissue properties of nerve bundles set to muscle properties, or to standard nerve bundle properties (Table 8.2). The potentials were obtained from an interpolation line at 0.91 mm (measured from the nerve bundle center) which was aligned with the axon closest to the stimula-

tion electrode (compare to Figure 8.1). These extracellular potentials were applied to axon models in order to quantify the influence of the nerve bundle on the axon's activation.

### 8.2.5. Axon Diameter and Electrode-Axon Distance in Nerve Bundle

It was investigated if first all thick axons within a nerve bundle are activated or if first all axons that are closest to the electrode are activated. The main goal was to compare position changes of the axon within the nerve bundle with changes of the axon diameter. Three simulations with different axon diameters and different axon positions were performed (16  $\mu\text{m}$  axon at 0.9 mm, 16  $\mu\text{m}$  axon at -0.9 mm and a 10  $\mu\text{m}$  axon at 0.9 mm).

## 8.3. Results and Conclusions

### 8.3.1. Influence of Single Axon on Extracellular Potential

The assumption that the axon does not influence the extracellular potential was investigated. The potentials along the single axon model were computed for the three different material properties settings (no nerve; nerve without nodes of Ranvier; nerve with nodes of Ranvier) and compared with each other. Subtractions at points of the interpolation line between the simulation results for the different material settings are shown in Figure 8.5 (left chart). The largest influence on the potential (0.28 mV) was found underneath the stimulation electrodes at axial positions of 23 mm and 78 mm (see Figure 8.5(a)). At the axial position of 23 mm the TP was calculated using the linear nerve model and is shown in the right chart of Figure 8.5. The maximal deviation of the TP (0.06 mV, 0.15%) is very small as can be seen from the nearly congruent lines in Figure 8.5.

These results indicate that neither the low resistivity of the axoplasm, nor the high resistivity of the myelin influences the extracellular potentials of axons. This shows that the influence of the inhomogeneity evoked by an axon on the extracellular potential is small and can be neglected in FE models.

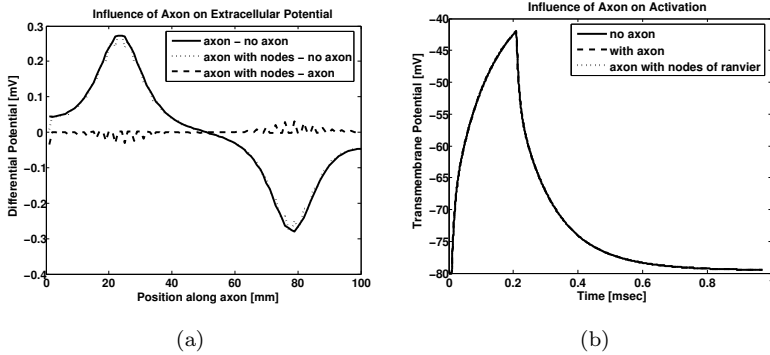


**Figure 8.5.** The left plot (8.5(a)) shows the subtraction of the extracellular potential over the whole length of the model for different material properties. The right plot (8.5(b)) shows the TP for the same material properties (the curves are congruent).

### 8.3.2. Influence of a Nerve Bundle on the Axon's Extracellular Potential

The influence of the presence of a nerve bundle on the extracellular potential of axons was investigated. Figure 8.6 shows the results from the linear nerve model where activation of a model with nerve bundle was compared with a model without nerve bundle. A small difference of the TP at the peak after the stimulation pulse was found (0.21 mV). The activation threshold using the non-linear axon model increased from 2.94 mA to 2.96 mA when including the tissue properties of the nerve bundle. These results show that the influence of the nerve bundle tissues on the axons' extracellular potential and axon activation is small. Therefore, in conclusion, the geometry and properties of nerve bundles do not need to be incorporated in FE models describing TES.

### 8.3.3. Axon Diameter and Electrode-Axon Distance in Nerve Bundle

The plot in Figure 8.7 shows that a maximal position change inside the nerve bundle (from 0.9 mm to -0.9 mm) reduces the simulated TP in the linear nerve model from  $-58.7$  mV to  $-69.3$  mV. About the same reduction of activation from  $-58.7$  mV to  $-69.8$  mV was found



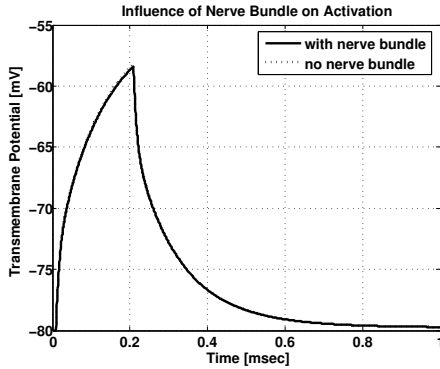


**Figure 8.6.** Comparison of nerve activation in a model that includes the geometry and properties of a nerve bundle with a model where the nerve bundle was neglected. A small influence of the presence of a nerve bundle on the axon’s extracellular potential and activation was found.

when changing the axon diameter of the axon at position 0.9 mm from  $16\ \mu\text{m}$  to  $10\ \mu\text{m}$ . This means that when all  $16\ \mu\text{m}$  axons within the nerve bundle are activated only axons down to  $10\ \mu\text{m}$  are activated although thinner axons are present in the nerve bundle. This indicates that it can be difficult to generate large recruitments (activate thin axon diameters) without generating co-contractions by stimulating deeper and adjacent nerves. This agrees well with clinical observations made with TES on patients.

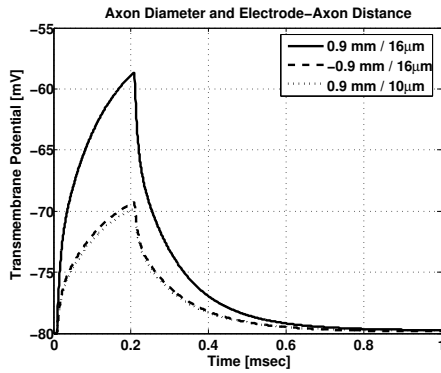


**Figure 8.7.** The TP versus time is depicted for two axon positions (deviation from nerve bundle center 0.9 mm and -0.9 mm) and two axon diameters ( $16 \mu m$ ,  $10 \mu m$ ).

# 9

## Main Influences in TES (Summary)

The influences of different tissue properties and tissue compositions were analyzed in this part (part III) and are summarized in Table 9.1. The column "Max influence" in the table are the changes that are obtained when one of the parameters is changed from the standard value (Table 3.2 and 3.3) to either the maximal or minimal value that was found in own experiments or in literature. The column "10% sensitivity" shows the influence of a change of 10% from the standard value. The detailed discussion of the results for every parameter can be found under the specified reference.

A large percentage value in the column "10% influence" of Table 9.1 means that already a small perturbation of this parameter can have a large influence on nerve activation. As a consequence these are considered the dominant parameters for TES as they strongly influence the resulting nerve activation. The results show that the *muscle resistivity*, the *axon depth*, and the *axon diameter* have the largest influences. The big influence of the axon depth also implies that the large range of fat

thicknesses found in humans has a large influence on nerve activation (see column "Max influence"). In general, the parameters with a large influence have to be incorporated in TES models whereas parameters with a small influence on nerve activation can be neglected or approximated in TES models (as for example in [SMHR07] where the thin skin layer was removed and a combined skin-fat layer was used instead).

Parameter		Max influence [%]	10% sensitivity [%]	Reference
Permittivity	Elec-skin inter	0.1	< 0.1	Section 7.1
	Skin, fat	2	< 0.1	
	Muscle	4.8	< 0.1	
Resistivity	Skin	< 0.1	< 0.1	Section 7.2
	Fat	0.1	< 0.1	
	Muscle	43.82	9.74	
	Bone	1.55	0.63	
Detailed anatomy		2.9	-	Section 7.3
Bone-axon distance		10 (for inhom-axon spacing above 0.8cm)	-	Section 7.4
Inhomogeneity		10 (for inhom-axon spacing above 0.5cm)	-	
Layer thickness	Skin	7.48	0.54	Section 7.5
	Fat	467.58	0.56	
	Muscle	7.23	1.32	
	Bone	0.61	0.44	
Axon depth		1458 (changing depth from 0.1cm to 3.1cm)	11.28	Section 7.6
Axon diameter		1488 (changing diameter from 11 $\mu\text{m}$ to 4 $\mu\text{m}$ )	17.24	Section 7.6
Nerve bundle geometry		< 0.1	< 0.1	Chapter 8

**Table 9.1.** Table summarizes the maximal influence and the 10% sensitivity of different tissue properties and tissue composition on nerve activation. The largest influence (maximal range of published parameters) was found for the muscle resistivity, the fat thickness, the axon depth, and the axon diameter. When looking at the sensitivity (10%), the muscle resistivity, the axon depth, and the axon diameter have the largest influence.



Part IV

**ELECTRODE  
PROPERTIES AND  
ELECTRODE  
GEOMETRIES**





# 10

## Overview

In this part the influence of electrode properties and electrode geometries on nerve activation are analyzed. First it is investigated whether locally high current densities which are due to skin and electrode inhomogeneities can be reduced using high resistance electrodes (chapter 11). Afterwards, in section 12.2 the influence of different electrode materials on nerve activation and comfort is investigated. Based on these results and additional simulation results the electrode size is optimized for selectivity and comfort in section 12.3. After discussing single electrodes in chapter 12, array electrodes are the topic of chapter 13. It is shown how the gap sizes between array elements and the resistivity of the electrode-skin interface material should be chosen in order to produce a good efficiency of array electrodes compared to standard single electrodes.



# 11

## Homogeneous Current Densities using High Resistance Electrodes

In TES self adhesive hydrogel electrodes are used to deliver electrical currents into the tissues with the aim to generate APs in motor nerves. The electrodes are crucial for effective and comfortable stimulation [AKH94]. Localized high current densities can cause discomfort or even skin burns [PYS<sup>+</sup>05]. Such high current densities can have different origins:

- Inhomogeneities of the resistance in the electrode material can cause locally high current densities and worsen stimulation comfort. The size of such inhomogeneities is usually a couple of mil-

limeters [LK05].

- Current densities are higher at the edges of electrodes (edge effects) [Rat90].
- The skin layer has a complex structure with local inhomogeneities that lead to resistance changes [PCWS93, PWS94], which cause locally higher or lower current densities. Different sizes of inhomogeneities were identified: Small inhomogeneities from pores and sweat glands which have a size of 50 to 100  $\mu m$  [Gri84, CIK<sup>+</sup>98]; larger inhomogeneities that are due to different water content and due to different skin structures that have a size of a couple of millimeters [RACS98].

It is hypothesized that high resistance electrodes can improve the homogeneity underneath surface electrodes. Panescu et al. [PWS94] presented a 2D FE model with millimeter sized skin inhomogeneities to analyze this hypothesis. They showed that high resistivity electrodes can improve the distribution of the current density underneath surface electrodes. Sha et al. [SKH<sup>+</sup>07b] integrated one pore sized ( $\mu m$ ) skin inhomogeneity in a 2D axis-symmetric FE model. They also found that higher electrode resistivities can reduce high current densities peaks due to the skin inhomogeneities. Here a more detailed 3D FE model is presented that allowed the investigation of large ( $mm$ ) and small ( $\mu m$ ) inhomogeneities in the skin and additionally in the electrode.

## 11.1. Methods

The influence of the edge effects and the inhomogeneities in electrode gels and skin on the localized current densities is investigated. The potential and the current density distribution were calculated using the static FE model described in section 3.1.5. Three different geometries were implemented to investigate edge effects, small inhomogeneities ( $\mu m$ ), and large inhomogeneities ( $mm$ ) in the following three subsections.

### 11.1.1. Electrode Edge Effects

The electrode edge effects can be investigated using the AF (section 3.2.1.2) [Rat90]. The AF was calculated underneath the cathode at typical depths from the fat-muscle interface between 0.1 cm and 2.5 cm.

These are depths where motor nerves can be expected in human arms. The edge effects were defined as  $EE = 1 - \frac{AF_{center}}{AF_{max}}$  where  $AF_{center}$  is the the AF value at the center of the electrode and  $AF_{max}$  is the maximal AF value underneath the electrode. The maximal AF value can be at the edge but also at the center when no edge effect is present. The edge effects reach a maximum at  $EE = 1$  when  $AF_{max} \gg AF_{center}$ , and no edge effects are present at  $EE = 0$  when  $AF_{max} = AF_{center}$ . The edge effects were calculated for two electrode sizes ( $3 \times 3 \text{ cm}^2$ , and  $5 \times 5 \text{ cm}^2$ ) and at different electrode gel resistivities between  $1 \Omega m$  and  $10k \Omega m$ . The influence of changes of the tissue resistivities such as skin or fat (see Table 3.3) on the edge effects were also quantified.

### 11.1.2. Small Skin Inhomogeneities (Pores, Glands)

Figure 11.1 shows the geometry that was used to model small inhomogeneities within the skin structure. An array of small channels through the skin representing pores and glands (identified as black dots in Figure 11.1(a)) were placed under the electrode surface with a density of 100 per  $\text{cm}^2$  and diameters of 50 or  $100 \mu m$  (common values for a human forearm). A small electrode of  $0.5 \times 0.5 \text{ cm}^2$  was modeled because larger areas significantly increased the number of finite elements in the FE model. The tissue properties are given in Table 3.3 and the skin inhomogeneity (e.g. pore) had a resistivity of  $1.4 \Omega m$  [SKH<sup>+</sup>07b]. A current of 5 mA was applied between the stimulation electrode and the plane underneath the volume representing muscle.

### 11.1.3. Large Inhomogeneities (Water Content, Structure)

Larger inhomogeneities in electrode and skin were investigated using the geometry shown in Figure 11.2. The inhomogeneities in the electrode and the skin were assumed to have a factor of 10 lower resistivity than the surrounding electrode gel resistivity or skin resistivity ( $\frac{\rho_{gel}}{10}$  and  $\frac{\rho_{skin}}{10}$ ) [PWS94]. Either skin inhomogeneities or electrode inhomogeneities were modeled, but the combined effects were not investigated. The inhomogeneities had a diameter of either 0.2 cm or 1 cm [PWS94, Odl83].

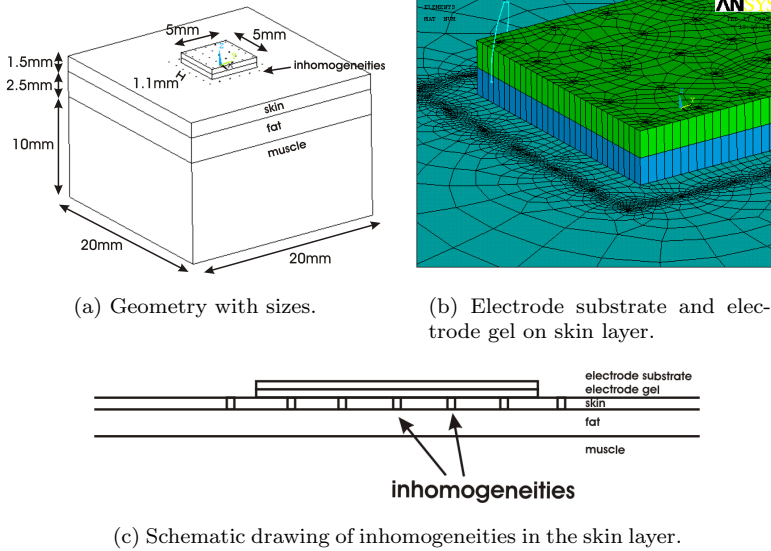


**Figure 11.1.** Geometry and mesh of the model used to analyze small inhomogeneities.

#### 11.1.4. Comparison of Current Densities underneath Inhomogeneities

In this subsection it is described how the influence of the electrode and skin inhomogeneities on the local current densities were quantified in the models introduced in the previous two subsections.

Relative changes  $\delta CD_i$  (Equation (11.1)) of the current densities ( $CD$ ) between cases with and without inhomogeneities were investigated at different locations ( $i$ ) underneath the cathode. The  $CD_i$  values are the average current densities on the circle representing the inhomogeneity at the electrode-skin interface, the skin-fat interface, and the fat-muscle interface.

$$\delta CD_i = \frac{(CD_i^{WithInhomo} - CD_i^{NoInhomo})}{CD_i^{NoInhomo}} \quad (11.1)$$

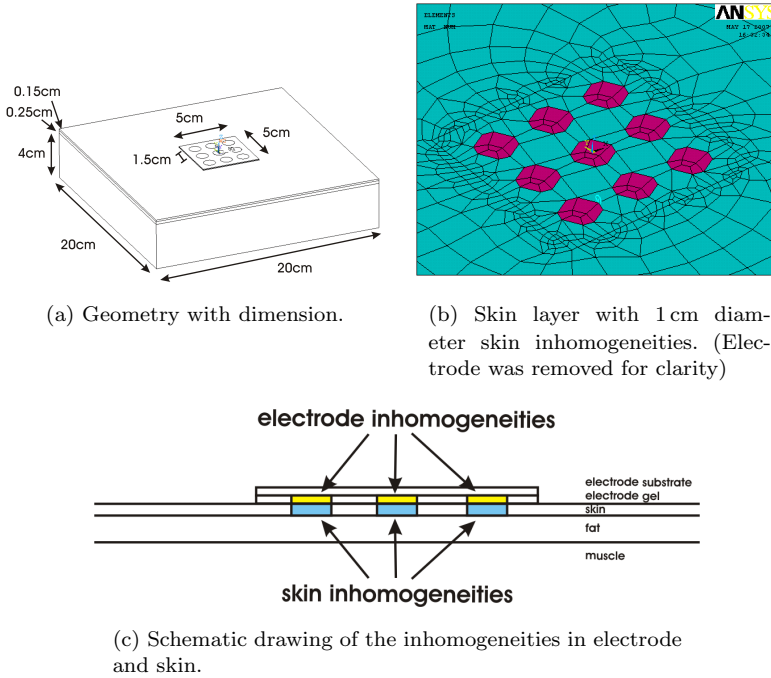


**Figure 11.2.** Geometry and mesh of the model used to analyze large inhomogeneities in electrode and skin.

## 11.2. Results and Discussion

### 11.2.1. Electrode Edge Effects

The edge effects that are present under a  $5 \times 5 \text{ cm}^2$  electrode with a gel resistivity of  $\rho_{gel} = 300 \Omega m$  (hydrogel) are depicted in Figure 11.3. It can be seen that the edge effects diminish quickly with depth due to the spreading of the current.

The influence of different resistivity changes (skin, fat, muscle, and bones) on the electrode edge effects was investigated and the change of  $EE$  is below 0.1% for resistivity changes in the ranges given in Table 3.3.

The edge effects for two electrode sizes and different electrode gel re-

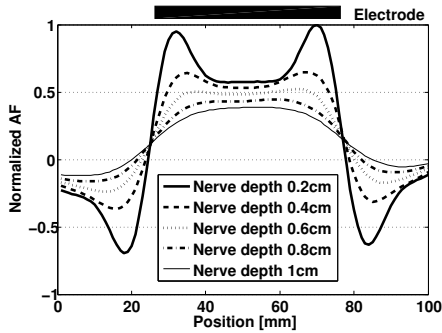


**Figure 11.3.** AF at different depths underneath a  $5 \times 5 \text{ cm}^2$  cathode ( $\rho_{gel} = 300 \Omega m$ ). Edge effects are largest for superficial nerves.

sistivities are shown in Figures 11.4 and 11.5. A higher gel resistivity and smaller electrodes reduce the edge effects. For  $1 \times 1 \text{ cm}^2$  electrodes the edge effects were 0 and are therefore not shown in a Figure.

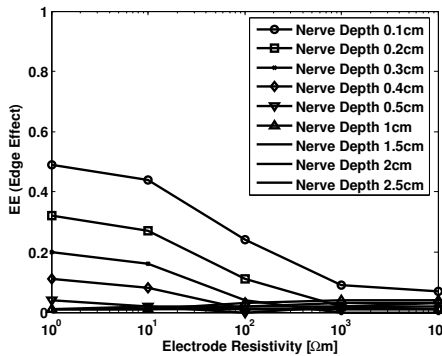


**Figure 11.4.** Edge Effects for different electrode gel resistivities and nerve depths using a  $3 \times 3 \text{ cm}^2$  electrode. The edge effects decrease for larger electrode gel resistivities and deeper nerves.



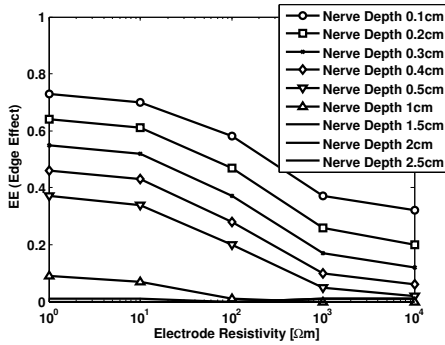


**Figure 11.5.** Edge Effects for different electrode gel resistivities and nerve depths using a  $5 \times 5 \text{ cm}^2$  electrode. The edge effects decrease for larger electrode gel resistivities and deeper nerves.

Observed location	50 $\mu\text{m}$ diam. inhomo.	100 $\mu\text{m}$ diam. inhomo.
electrode-skin interface	7.86%	14.40%
skin-fat interface	12.38%	24.33%

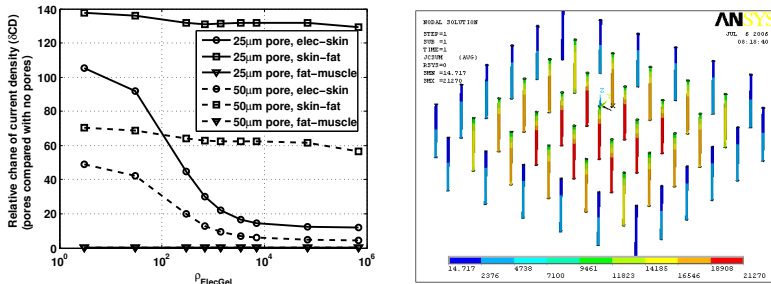
**Table 11.1.** Percentage of the total current flowing through the inhomogeneity at the electrode-skin and skin-fat interface (hydrogel electrode with  $\rho_{gel} = 300 \Omega\text{m}$ ).

### 11.2.2. Small Skin Inhomogeneities (Pores, Glands)

Table 11.1 shows the percentage of the current that flowed through the inhomogeneity at the electrode-skin and the skin-fat interface for a gel resistivity similar to standard hydrogel electrodes ( $\rho_{gel} = 300 \Omega\text{m}$ ). With inhomogeneities in the skin layer, a large portion of the current (7.86% and 14.40%) flowed into the inhomogeneities (Table 11.1) at the electrode-skin interface. An even larger portion of the current flowed out of the inhomogeneity at the skin-fat interface (12.38 and 24.33%). Knowing that the area of the pores at the electrode skin interface was only 0.19% of the total electrode area indicates how much the current is attracted by the good conducting skin channels.

The effect of high resistivity electrodes on the homogeneity of the current was investigated using the relative change  $\delta CD_i$  (Equation (11.1)). In Figure 11.6(a)  $\delta CD_i$  at different locations  $i$  (depths) is shown.  $\delta CD$  at the fat-muscle interface was 0 for all electrode gel resistivities show-

ing that the inhomogeneities have no influence on motor nerves which are located in the muscle layer. At the electrode-skin interface  $\delta CD$  decreased from 105.5 to 12.12 for a  $25\mu m$  diameter inhomogeneity when changing the electrode gel resistivity from 3 to  $700000\Omega m$ . However, at the skin-fat interface  $\delta CD$  was only decreased from 137.6 to 129.1. These results indicate that higher gel resistivities decrease the locally high current density at the electrode-skin interface, but not at the skin-fat interface. It can be seen in Figure 11.6(b) that the current densities inside the inhomogeneities increase with depth within the skin layer what means that more current enters the good conducting inhomogeneities within the skin layer.



(a) Relative change of the current density  $\delta CD_i$  of the current density in the circles representing the inhomogeneities at the electrode/skin, the skin/fat, and the fat/muscle interface.

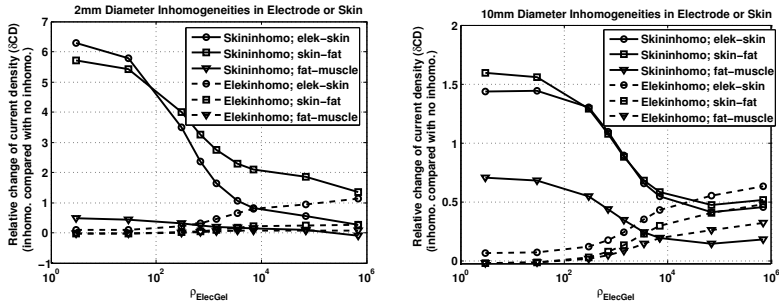
(b) Current density within the inhomogeneities.

**Figure 11.6.** Simulation results using model with small skin inhomogeneities.

### 11.2.3. Large Inhomogeneities (Water Content, Structure)

The influence of high electrode gel resistivities on the homogeneity of the current density was investigated when large inhomogeneities are present in the electrode gel or the skin. For a  $2\text{ mm}$  diameter inhomogeneity in the electrode  $\delta CD$  at the electrode-skin interface increases from 0.08 to 1.1 when increasing the electrode gel resistivity from 3 to  $700000\Omega m$  (see Figure 11.7(a)). For an inhomogeneity in the skin  $\delta CD$

decreased for the same electrode gel resistivity change from 6.3 to 0.26. These results show that for an increasing electrode gel resistivity, the inhomogeneities in the electrode and the skin have contrary effects on  $\delta CD$  (Figure 11.7). For low electrode gel resistivities the skin inhomogeneities are dominant and for high electrode gel resistivities the inhomogeneities of the electrode are dominating the relative change of the current density  $\delta CD$ . As a consequence an optimal electrode gel resistivity can be found. The optimal resistivity is the crossing point of the lines for electrode inhomogeneities and skin inhomogeneities for a certain interface (in Figure 11.7). At different interfaces and for different inhomogeneity sizes the optimal resistivity is not the same. Therefore, no general optimal electrode gel resistivity can be presented. However, it is important to know that when electrode impurities (inhomogeneities) are present, the electrode gel resistivity should not be as high as possible because the impurities decreases the homogeneity of the current density.



(a)  $\delta CD$  for 2 mm electrode and skin inhomogeneities.

(b)  $\delta CD_i$  for 10 mm electrode and skin inhomogeneities.

**Figure 11.7.** Relative change of the current density  $\delta CD_i$  in the circles representing the inhomogeneities at the electrode/skin, the skin/fat, and the fat/muscle interface when large inhomogeneities are present in the electrode or the skin layer.

### 11.2.3.1. Small vs. Large Inhomogeneities

For the small inhomogeneities (section 11.2.2) it was found that higher electrode gel resistivities cannot improve the homogeneity of the cur-

rent density throughout the whole skin layer. The reason was that the homogeneity was only improved at the electrode-skin interface and not at the skin-fat interface. In Figures 11.7(a) and 11.7(b) where the results of the large skin inhomogeneities are shown it can be seen that  $\delta CD$  decreases at both the electrode-skin and the skin-fat interfaces. Hence, for the large inhomogeneities the higher electrode gel resistivity can improve the homogeneity of the current density within the skin layer.

### 11.3. Conclusions

- The higher current densities at the edge of surface electrodes compared to the center of the electrodes (edge effect) can be reduced by using a higher electrode gel resistivity.
- Locally high current densities occurring from large skin inhomogeneities can be decreased with high resistive electrodes. Compared to standard hydrogel electrodes ( $300 \Omega m$ ) a high resistive electrode ( $70000 \Omega m$ ) decreased the relative change of the current density  $\delta CD_i$  from 4 to 2 (50% improvement) at the skin-fat interface. These results compare well with [PWS94] where a more even current density distribution was also predicted. However, for small skin inhomogeneities (e.g. pores), where much higher peak current densities are present, there was only a small improvement from 136 to 132 (3%) at the skin-fat interface. These simulation results are in agreement with an experimental study that showed only marginal comfort improvements when using high resistance electrodes [SKH<sup>+</sup>07a].

In another study Sha et al. [SKH<sup>+</sup>07b] predicted in a simulation study that for small inhomogeneities (pores) the current density distribution can be improved using high resistance electrodes which could not be reproduced with the presented model. In Figure 11.6(b) it is shown that the current densities inside the inhomogeneities increase with depth within the skin layer. It might be that this effect is more prominent in a 3D model as shown here compared to the 2D model presented in [SKH<sup>+</sup>07b]. In a 3D model the current can enter the pore from all sides, whereas the 2D case has only two boundary lines where the current can flow from the skin into the pore.

- A direct conclusion from a changing  $\delta CD_i$  onto changing human sensation is not yet possible because other influences such as electrode size, location of the electrode, pain aversion of the person, and many more effects would have to be taken into account. Many of these influences currently can't be quantified and are subject to future research. A possible way to incorporate sensation (comfort) in a TES model is presented in section 12.3 where a combined approach using modeling and experiments is presented.
- Inhomogeneities in high resistivity electrodes cause locally high current densities. This effect increases for higher electrode gel resistivities. Therefore, electrode inhomogeneities should be avoided in the production process of high resistivity electrodes.
- The electrode gel resistivity should not be as high as possible. There is trade-off between a more homogeneous current distribution due to a higher electrode gel resistivity and a uneven current distribution due to inhomogeneities in the electrode material. In general electrodes with smaller inhomogeneities in the electrode material can have a higher resistance.
- The results show that there is no universal electrode gel resistivity that is best for all parameter combinations. However, the results indicate (see Figures 11.7(a) and 11.7(b)) that using electrode gel resistivities that are above the values of the skin resistivity ( $\rho_{gel} > 700 \Omega m$ ) should be favored. Lower gel resistivities always resulted in a less homogeneous current distribution. Significantly higher resistivities do not improve homogeneity much further and will only cause high voltages at the stimulation electrodes. (The influence of the gel resistivity on motor activation was found to be small in simulations (Table 9.1) and experiments (Figure 12.1).)



# 12

## Single Electrodes

This chapter examines three topics that are related to the properties (size and material composition) of single electrodes:

- The effect of electrode size on chronaxie is analyzed and compared to experimental results.
- The influence of the electrode material on comfort (sensation) and nerve activation is investigated.
- Electrode sizes with a good trade-off between comfort and selectivity are derived.

### 12.1. Explaining Chronaxie Diversity

In section 4.2 it was introduced that chronaxie values that were experimentally measured in humans vary between  $200 - 700 \mu s$  [SKPS05, Har71, KBAB00] and it was shown that the presented TES model can describe chronaxie values within this range (Figure 4.6). However, it was not investigated which parameters are mainly causing the large range of chronaxie values found in experimental measurements. For the

near-field situation (implantable systems) it has been shown that the electrode size and the electrode/nerve distance are the main reasons for the variation (30 – 150  $\mu s$ ) of the chronaxie values [RB87, RACS98]). In the far-field situation other parameters like tissue layer thicknesses or the capacitive effects might also have an influence on the chronaxie. The aim was to investigate with our computer model which parameters cause the large range of chronaxie values (200 – 700  $\mu s$ ) observed in strength-duration measurements with surface electrodes (far-field situation).

### 12.1.1. Methods

The TES model with nerve model  $D$  (Table 3.4) that was introduced in section 3.3 was used in order to investigate the effect of different parameter changes on the chronaxie. The chronaxie ( $T_{ch}$ ) was calculated from strength duration curves as described in section 4.2.1.3. Influences from the following parameters on the chronaxie were analyzed: tissue thicknesses, tissue resistivities, tissue permittivities, electrode size, and nerve depth. The influences of the thicknesses, the resistivities, and the permittivities were already presented in sections 7.5, 7.2, and 7.1. The relevant results will be reviewed in the discussion of this section. Electrode sizes between  $0.1 \times 0.1 \text{ cm}^2$  and  $7 \times 7 \text{ cm}^2$  and two nerve depths (from fat-muscle interface) of 0.2 cm and 1.5 cm were considered. Electrode sizes below  $0.5 \times 0.5 \text{ cm}^2$  are usually not used in TES and were included to allow a comparison of our simulated chronaxie values with publications that use point sources as electrodes.

### 12.1.2. Results and Discussion

The resulting chronaxie values ( $T_{ch}$ ) obtained from changing the electrode size or the nerve depth are shown in Table 12.1 for nerve model  $D$ . It can be seen that the chronaxie values change in the range from 220  $\mu s$  to 574  $\mu s$ . In general, smaller electrodes and more superficial nerves result in smaller chronaxie values and vice versa.

Changing tissue thicknesses (section 7.5), tissue resistivities (section 7.2), and tissue permittivities (7.1) in the range of values that cover most human forearms resulted in chronaxie changes below 1.1%. Only the thickest fat layer (30 mm) had a larger influence on the chronaxie (6.3%). This is due to the spread of the current in the thicker fat layer that influences more nodes of the nerve models simultaneously. These are small changes compared to the influence of different electrode sizes



Electrode size [ $cm^2$ ]	$T_{ch}$ (0.2 cm) [ $\mu s$ ]	$T_{ch}$ (1.5 cm) [ $\mu s$ ]
$0.1 \times 0.1$	220	465
$0.2 \times 0.2$	255	467
$0.5 \times 0.5$	274	467
$1 \times 1$	303	468
$2 \times 2$	384	471
$3 \times 3$	445	477
$5 \times 5$	457	510
$7 \times 7$	433	574

**Table 12.1.** Simulated chronaxie values  $T_{ch}$  using nerve model D (MRG) for different electrode sizes and two nerve depths (0.2 cm and 1.5 cm).

and the nerve depths shown in Table 12.1. These results show that the electrode sizes and the electrode-nerve distance have the largest influence on chronaxie values amongst the tested parameters. We conclude that the electrode size and the electrode-nerve distance influence more nodes of Ranvier, which leads to an increase of the chronaxie values. The result that smaller electrodes and smaller electrode-nerve distances generate smaller chronaxie values was also found in studies that investigated implantable electrodes close to the axon [RB87, RACS98].

### 12.1.3. Conclusions

For implantable stimulation (near-field) it was shown that mainly the electrode size and the electrode/nerve distance influence the chronaxie. Our results show that the chronaxie in the far-field situation is influenced as well as with implantable electrodes mainly by the electrode size and the electrode/nerve distance. With electrode sizes between ( $0.1 \times 0.1 cm^2$  and  $7 \times 7 cm^2$ ) and electrode-axon distances between 0.6 cm and 1.5 cm, chronaxie values between  $220 \mu s$  and  $574 \mu s$  were obtained. The capacitive effects, variations of the tissue resistivities, and variations of the tissue thicknesses were found to have a minor influence.

## 12.2. Influence of Electrode Material on Nerve Activation and Comfort

In clinical applications different electrode materials are used for ES: Metal plates with soaked cotton, silver-silver chloride electrodes, carbon rubber electrodes, hydrogel electrodes, and many more. The de-

cision on the electrode type depends mostly on the application it is used for. For example carbon rubber electrodes are usually used for iontophoresis or hydrogel electrodes are used for neuromuscular stimulation in the rehabilitation of stroke or spinal cord injured subjects. Further, new stimulation techniques [LPK<sup>+</sup>08] require new materials with adapted electrical properties in order to minimize losses; for example higher resistivities are required for array electrodes as will be described in chapter 13. All these electrodes have very different physical (sticky, wet, dry, ...) and electrical properties which might influence stimulation comfort and the intensity of nerve and muscle activation. The aim of this section is to investigate how the choice of electrode material influences the comfort and the nerve activation during TES. Simulations and experimental measurements were performed.

### 12.2.1. Methods

Experimental measurements were performed to identify motor thresholds and pain thresholds for different electrode materials on the forearm of human volunteers. The tested materials were Hydrogel ( $200\ \Omega m$ ), Hotmelt ( $400\ \Omega m$ ), and Carbon Rubber ( $5\ \Omega m$ ). Motor thresholds were measured with the automated motor threshold measurement using an accelerometer described in section 4.2.1.2 on the same ten subjects as in section 4.2.1.2.

Following the automated motor threshold detection of each electrode material, the excitatory levels (sensory-, motor-, pain-, and stop threshold) were recorded without removing the electrode. Although mainly interested in the pain thresholds we also measured all excitatory levels according to the standard procedure used in [AKH94]. Rectangular, biphasic current regulated pulses with a pulse duration of  $300\ \mu s$  and a repetition frequency of 25 Hz were applied (see Figure 2.9). These are normal parameters for TES. Continuous stimulation was slowly ramped with 1 mA every 2 seconds. The volunteers were asked to indicate when they felt stimulation (sensory threshold), when a minimal visible muscle contraction was observed (motor threshold), when the stimulation was painful and uncomfortable (pain threshold), and when the volunteer could no longer tolerate higher stimulation amplitudes (stop threshold) [AKH94]. This test was repeated until the four thresholds in the two last measurements were within  $\pm 1\ mA$ . Usually the experiments had to be repeated once or twice.

### 12.2.2. Results and Discussion

Motor thresholds in ten human volunteers were automatically determined using an accelerometer. The resulting stimulation amplitudes are shown in Figure 12.1 for two electrode sizes. The effect of the electrode material was analyzed using a one way analysis of variance (ANOVA). For both electrode sizes the ANOVA test was not significant ( $p < 0.7958$  for the data in Figure 12.1(a) and  $p < 0.6471$  for the data in Figure 12.1(b)). Fisher's post hoc test revealed that the current amplitude does not significantly change as the electrode material is changed. This indicates that the electrode material does not have an influence on motor nerve activation. Similar results were found using simulation as described in the next paragraph.

Simulation results that were performed using the model described in section 7.2 also showed a small influence of the electrode resistivity. Changing the electrode resistivities in the range given in Table 3.3 changed  $I^{th}(1.1cm, 11\mu m)$  from  $4.16 mA$  to  $4.31 mA$ . This confirms the small influence of the material resistivity on motor nerve activation that was found experimentally (Figure 12.1(a)).

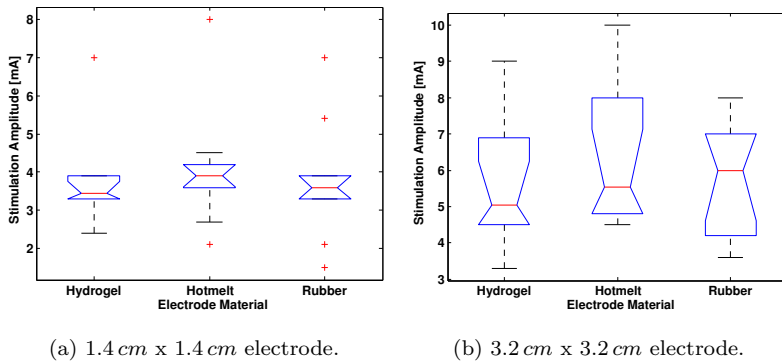


**Figure 12.1.** Measured motor thresholds using different electrode materials and electrode sizes.

The pain thresholds for different electrode materials were also determined and are shown in Figure 12.2. The ANOVA test on the pain threshold resulted in significant differences among the different electrode materials at the ( $p < 0.01$ ) level. Fisher's post hoc test showed

that the pain threshold for the carbon rubber was significantly lower than the pain threshold using hydrogel or hotmelt. However, between the hydrogel and the hotmelt no significant difference is present. This result was found for both electrode sizes.

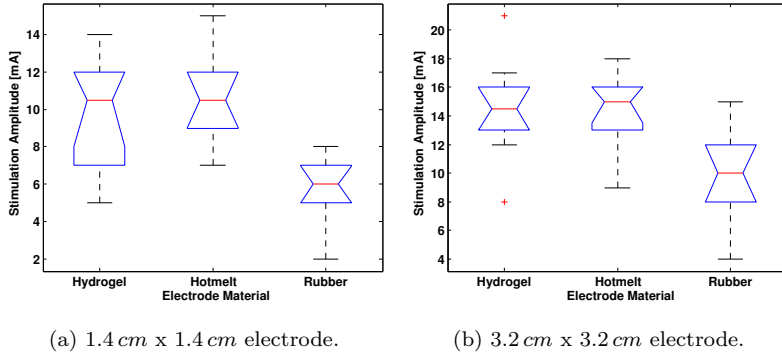


**Figure 12.2.** Measured pain thresholds using different electrode materials and electrode sizes.

### 12.2.3. Conclusions

The results show that the motor thresholds are not influenced by the tested electrode materials when using current regulated stimulation. Simulations yield similar results when the electrode resistivity was varied (see section 7.2). However, the comfort (pain threshold) is largely influenced by the choice of electrode material over a wide range of current densities. This means that new electrodes can be designed with the focus on optimizing stimulation comfort without compromising stimulation magnitude.

Two limitations of this conclusion have to be considered:

- The voltage that has to be applied to the electrode in order to maintain a constant current increases when the electrode resistivity is increased. Lower voltages are preferred due to the reduced power consumption and for safety reasons.
- These results are only valid for single electrodes where the electrode substrate has the same size as the electrode gel. For larger

gel layers, as for example in section 13 where array electrodes are used that have a substrate smaller than the gel layer, the current can spread within the gel layer. For lower electrode resistivities this spread is larger than with higher electrode resistivities. As a result a higher stimulation current is required when using low electrode resistivities in order to achieve the same nerve activation as with higher electrode resistivities.

### 12.3. Optimizing Electrode Size to Stimulate a Certain Depth

In the background section 1.1 it was mentioned that clinically, TES is often applied for the rehabilitation of stroke subjects or spinal cord injured subjects [BMB<sup>+</sup>00], or for supporting tasks of daily living [KKLM07] using so called neuroprostheses [Nat79, Nat92, PGWK97, CC98]. In these applications two main aspects are important (i) the selective activation of specific muscles in order to generate the intended motor function and (ii) a comfortable stimulation in order to increase patient acceptance of TES. In this section the influence of the electrode size on these two aspects is investigated.

In the upper extremities, specifically for hand functions, the electrode size has an influence on selective activation of the multiple muscles bundled closely together. More selective activation of the different muscles can be achieved using smaller electrodes. Small electrodes are used for example in array electrodes which were proposed to improve efficacy of TES systems [PBBJ<sup>+</sup>05]. Such array electrodes are composed of multiple small electrode elements which can be individually activated to form a virtual electrode of arbitrary size and location [LKK04, KLKM06]. However, there are no guidelines on how small the individual elements should be in order to achieve comfortable stimulation of deep nerves. Elements that are too small might not be effective on persons with thick fat layers because the large current spread within the fat layer prevents the current to reach the motor nerves laying deeper [KK07]. Another effect of small electrodes is the generation of high current densities, which may be uncomfortable, indeed painful, and can limit the effectiveness of TES [GT75]. However, not only the current density influences the perceived comfort during TES but also electrode size and stimulation parameters [BMB<sup>+</sup>00, LLCM<sup>+</sup>04]. McNeal [MB88] investigated the comfort of two electrode sizes ( $4.5 \times 4.5 \text{ cm}^2$  and  $6 \times 6 \text{ cm}^2$ ) on the quadriceps and the hamstrings. For generating the same muscle

force output the human volunteers preferred the larger electrodes. More different electrode sizes were investigated by Alon et al. [AKH94]. Excitatory levels (sensory-, motor-, pain-, and maximal tolerable threshold) were experimentally investigated for four different square electrode sizes with edge lengths 6.3 cm, 4.5 cm, 3 cm, and 1.5 cm on the gastrocnemius. The two largest electrodes ( $6.3 \times 6.3 \text{ cm}^2$  and  $4.5 \times 4.5 \text{ cm}^2$ ) were significantly more comfortable and produced the highest force, when compared to the smaller electrodes. Hence, the  $4.5 \times 4.5 \text{ cm}^2$  electrode was the size of choice because the  $6.3 \times 6.3 \text{ cm}^2$  electrode could not further improve comfort and force. Lyons et al. [LLCM<sup>+</sup>04] compared the two largest electrode sizes ( $4.5 \times 4.5 \text{ cm}^2$  and  $6.3 \times 6.3 \text{ cm}^2$ ) used by Alon [AKH94] and showed that on the gastrocnemius the smaller  $4.5 \times 4.5 \text{ cm}^2$  electrode was significantly more comfortable compared to the  $6.3 \times 6.3 \text{ cm}^2$  electrode. Verhoeven et al. [VvD06] compared the generated pain of  $0.6 \times 0.6 \text{ cm}^2$  electrodes with the generated pain of  $3.6 \times 3.6 \text{ cm}^2$  electrodes when stimulating the tibial nerve for conduction studies. They found that pain could be reduced with the larger electrode ( $3.6 \times 3.6 \text{ cm}^2$ ) without compromising H- or M-waves. These studies show that differently sized electrodes were most comfortable on different subjects and on different body parts. However, what causes certain electrode sizes to be more comfortable than others and why from a certain size on larger electrodes become more painful was not conclusively analyzed up to now.

Finite element (FE) and nerve models have been used to describe TES [Cob85, RMMR04, KK07] (section 1.2). However, the influence of different transcutaneous electrode sizes on nerve activation has not been investigated. Only in other fields as for example in Defibrillation different electrode sizes were analyzed using a modeling approach [CLE95, KS96]. The aim in this section is to use the TES model in order to calculate optimized electrode sizes with respect to selectivity and comfort for different fat layer thicknesses and nerve depths. These results will help to determine what electrode sizes should be favored on different persons and body parts.

### 12.3.1. Methods

In the introduction of this section it was explained that the comfort is not only a function of the current density but also of the electrode size. In order to estimate the comfort in the TES model, pain thresholds were measured experimentally on healthy subjects in order to derive a

comfort index as a function of stimulation amplitude (current density) and electrode size (section 12.3.1.1). Comfort and selectivity of different electrode sizes were then calculated with the TES model for different fat layer thicknesses and nerve depths in order to determine optimized electrode sizes for different parameter combinations (section 12.3.1.2).

### 12.3.1.1. Experimental Measurements

The goal of the experiments was to identify pain thresholds for different electrode sizes on the forearm of human volunteers. Hydrogel was used as electrode interface material because this is the material generally used for neuroprostheses [KKLM07]. The experiments were undertaken in the same ten healthy subjects as for the motor thresholds (see section 4.2.1.2). After the determination of the motor threshold of each electrode size (section 4.2.1.2), the excitatory levels (sensory-, motor-, pain-, and stop threshold) were recorded without removing the electrode. The experimental procedure is described in section 12.2.1 where the pain thresholds for different electrode materials were analyzed. The pain thresholds that were measured are named  $ThP_A$  where  $A$  denotes the different electrode sizes (areas) that were tested.

**Data Analysis** The effect of electrode size was analyzed using a one way analysis of variance (ANOVA). Significant ( $p < 0.01$ ) F ratios were further analyzed with Fisher's post hoc test.

### 12.3.1.2. TES Model

Nerve activation was calculated using the TES model introduced in section 3.3 with the parameters that are summarized in the tree structure below.

FE model	
└─ Geometry .....	cylindrical geometry
└─┬─ Tissue thicknesses .....	standard values from Table 3.2
└─┬─ Tissue properties .....	standard values from Table 3.3
└─┬─ Electrode type .....	single electrodes
└─┬─┬─ Electrode sizes .....	0.8×0.8 - 4.1×4.1 cm <sup>2</sup>
└─┬─┬─ Electrode distance .....	11 cm
└─ Equation .....	static equation (3.17)
└─ Stimulation pulse .....	monopolar current regulated
└─┬─ Amplitude .....	$I$
└─┬─ Duration .....	300 $\mu$ s
Nerve model	
└─ Model IDs .....	$D^P$ (Table 3.4)
└─ Type .....	multiple single axons
└─ Axon diameter .....	11 $\mu$ m
└─ Axon depth .....	0.1 cm - 1.1 cm

Spatial nerve activation was described using activation volumes (AVs) that were introduced in section 3.4.2.1. The activation volumes were constructed for axons of 11  $\mu$ m diameter in order to model an intermediate recruitment of about 50% [RACS98]. In order to quantify the depth and the selectivity of nerve activation, the activation depth (defined in section 3.4.2.2) and the selectivity (defined in section 3.4.2.4) were calculated for different model parameters (e.g. electrode configuration, fat thickness,...).

**Estimated Comfort (COMF)** As proposed in [VvD06] pain was assumed to be proportional to the current density in the TES model. Current density underneath the stimulation electrodes was not measured directly but estimated by dividing the amplitude of stimulation  $I$  by the area of the electrode. However, because pain is not perceived the same for different electrode areas [AKH94], the current density was corrected for different electrode areas with the average factor  $\overline{ThP_A}$ . The factor  $\overline{ThP_A}$  is the mean pain threshold amongst the ten volunteers (section 12.3.1.1) for electrode areas  $A$ . Hence, the measure for the estimated pain was  $\frac{I/A}{\overline{ThP_A}/A}$ , where  $I$  is the applied current amplitude and  $A$  is the electrode area. For the estimated comfort (COMF) we used the inverse of the pain:



$$COMF = \frac{1}{\frac{I/A}{\overline{ThP_A/A}}} = \overline{ThP_A}/I \tag{12.1}$$

### 12.3.2. Results

#### 12.3.2.1. Experimental Pain Thresholds

The pain thresholds for different electrode sizes were determined on ten human volunteers. The ANOVA test on the pain threshold resulted in significant differences among the different electrode sizes at the ( $p < 0.01$ ) level. The current amplitudes at pain threshold increased significantly (Fisher’s post hoc test) for larger electrode sizes (Figure 12.3).

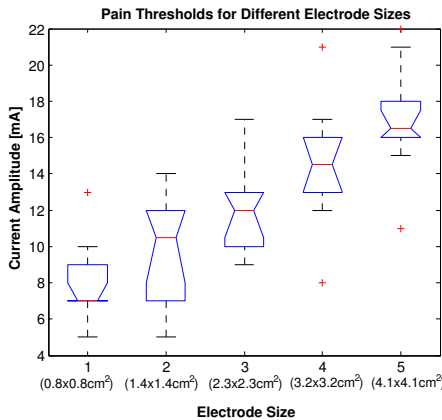


**Figure 12.3.** Notched box plot of the experimentally measured pain thresholds for different electrode sizes.

The actual current density that was present at the pain threshold for the different electrode sizes is shown in Figure 12.4. It is noticeable that the human volunteers could tolerate higher current densities with smaller electrodes.

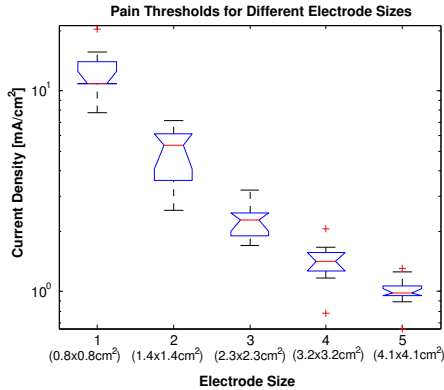


**Figure 12.4.** Notched box plot of the current density present at the experimentally measured pain thresholds for different electrode sizes.

### 12.3.2.2. Simulation Results using TES Model

**Estimated Comfort (COMF) vs. Selectivity (SEL)** The estimated comfort and the selectivity of different electrode sizes were assessed using the TES model for different fat thicknesses and activation depths. The stimulation amplitudes  $I$  were set such that for all combinations of electrode sizes and fat thicknesses a certain activation depth was reached. Using the current  $I$ , COMF values were calculated using the experimentally obtained pain thresholds (see equation (12.1)) and SEL values were calculated based on the size of the activation volume as described in section 3.4.2.4. The results in Figure 12.5 were calculated for different activation depths, different fat thicknesses, and different electrode sizes. The plot in Figure 12.5 depicts how comfortable and how selective different electrode sizes were in different anatomical situations. Each line shows the resulting COMF and SEL for a certain fat thickness and activation depth when the electrode size is changed. With increasing fat layers or larger activation depth the comfort and the selectivity decreased. Smaller electrodes were more selective compared to larger electrodes. In Table 12.2 the range of COMF and the range of SEL that was obtained with different electrode sizes is summarized. A larger range of SEL and COMF was found using smaller electrodes. This indicated that when using smaller electrodes the fat thickness and the activation depth have a much larger influence on the comfort and

the selectivity. This is an advantage for thin fat layers and small activation depths because a good comfort can be achieved. However, with thicker fat layers and larger activation depths small electrodes can be worse than larger electrodes. The optimized electrode sizes are given in the following section.

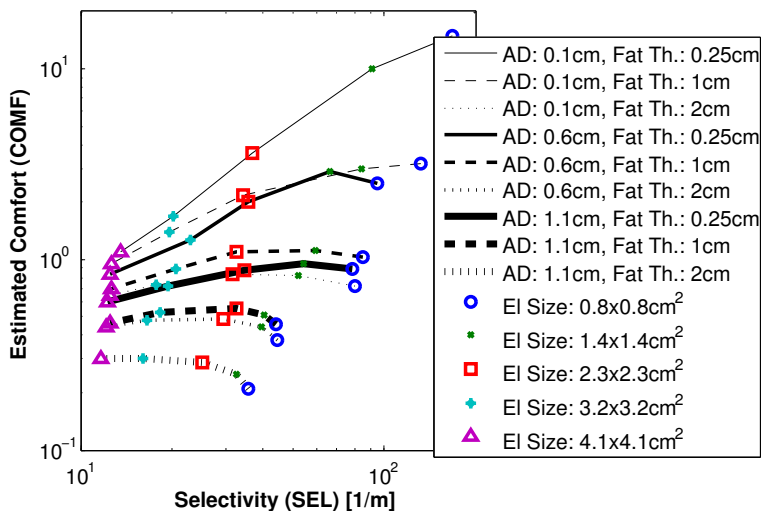


**Figure 12.5.** Comfort versus selectivity using different electrode sizes are depicted for different fat thicknesses and activation depths.

**Optimized Electrode Size** The electrode sizes with the largest COMF value (best comfort) were identified for all tested combinations of fat thicknesses and activation depths in Figure 12.5. The obtained electrode sizes are summarized in Table 12.3. The results show that for thicker fat layers and larger activation depths the electrode size with the best comfort increased.

### 12.3.3. Discussion

Pain thresholds were measured in ten human volunteers for different electrode sizes. In contrast to an earlier study that investigated pain thresholds on the leg [AKH94], the presented study concentrated on the forearm. The pain thresholds obtained over the Flexor Digitorum

El. Size.	COMF			SEL		
	min	max	range	min	max	range
0.8	0.2098	14.99	14.7802	35.56	168.4	132.84
1.4	0.2507	9.993	9.7423	32.62	91.13	58.51
2.3	0.2897	3.598	3.3083	25.18	36.98	11.8
3.2	0.3014	1.686	1.3846	16.07	20.28	4.21
4.1	0.3035	1.099	0.7955	11.72	13.61	1.89

**Table 12.2.** Range of comfort and selectivity that can be achieved with different electrode sizes with the tested fat thicknesses (0.25 cm - 2 cm) and activation depths (0.1 cm - 1.1 cm).

	Opt. El. Edge Length [cm]	Activation Depth (AD)		
		0.1 cm	0.6 cm	1.1 cm
Fat Thickness	0.25 cm	0.8	1.4	1.4
	1 cm	0.8	1.4	2.3
	2 cm	2.3	2.3	4.1

**Table 12.3.** Optimized electrode edge lengths [cm] (best comfort) for different fat layer thicknesses and activation depths.

Superficialis (forearm) (see Figure 12.3) were about a factor of 1.5 lower when compared to the thresholds of the gastrocnemius (leg) [AKH94] because the sensitivity for pain is higher on arms [RACS98].

The simulation results show that the most comfortable electrode size depends on the fat thickness and the nerve depth (Figure 12.5 and Table 12.3). For thin fat layers and superficial nerves to be activated smaller electrodes were more comfortable to achieve a specific activation or force (Table 12.3). The reason why smaller electrodes can be more comfortable than larger electrodes is because one can tolerate higher current densities on smaller electrodes (see Figure 12.4). The same has been shown in an experimental study by Alon et al. [AKH94], where the current density at pain threshold increased for smaller electrode sizes. This is because more nerve fibers and skin receptors are located under larger electrodes and their activation is spatially summed in the nervous system [MGP04]. As the electrode area is increased, the current density is lowered, but more nerves and nerve endings are stimulated. Hence, there are two concurring effects that may explain why optimal electrode sizes depend on the target nerve depth: For a constant current density smaller electrodes are more comfortable (see Figure 12.4), however deeper nerves can only be reached with larger electrodes because the spreading of the current is smaller.

Verhoeven et al. [VvD06] found that larger electrodes ( $3.6 \times 3.6 \text{ cm}^2$ ) were more comfortable for electrical stimulation of the gastrocnemius muscle compared to smaller electrodes ( $0.6 \times 0.6 \text{ cm}^2$ ). Lyons et al. [LLCM<sup>+</sup>04] investigated two larger sized electrodes ( $4.5 \times 4.5 \text{ cm}^2$  and  $6.3 \times 6.3 \text{ cm}^2$ ) and found that the smaller one  $4.5 \times 4.5 \text{ cm}^2$  was more comfortable. Our simulation results are not directly comparable with these experiments on the leg because other pain thresholds and a larger diameter cylinder would have to be used in the presented model. However, when applying the pain thresholds (gastrocnemius) that were presented in Alon's paper [AKH94] to the TES model and using a thick fat layer (1-2 cm) and a large activation depth (1 cm), the optimized electrode size was between  $3.2 \times 3.2 \text{ cm}^2$  and  $4.2 \times 4.2 \text{ cm}^2$ . This is in approximate agreement with Verhoevens [VvD06] and Lyons [LLCM<sup>+</sup>04] experimental results.

The optimized electrode sizes that are given in Table 12.3 were electrode sizes with the best comfort amongst the investigated sizes. The selectivity could still be improved as it can be seen in Figure 12.5. Therefore, these optimized electrode sizes should be viewed as upper limit. Smaller electrodes than these optimized sizes increase the selec-

tivity but decrease the comfort. Larger electrodes decrease both the selectivity and the comfort, and are therefore not efficient and should not be used.

#### 12.3.4. Conclusions

Comfort and selectivity of different electrode sizes were calculated with the TES model for different fat layer thicknesses and nerve depths. We were able to find optimal electrode sizes for different anatomies. Small electrodes ( $0.8 \times 0.8 \text{ cm}^2$ ) were found to be more comfortable for thin fat layers ( $0.25 \text{ cm}$ ) and superficial nerves ( $0.1 \text{ cm}$ ) and larger electrodes ( $4.1 \times 4.1 \text{ cm}^2$ ) were more comfortable for thicker fat layers ( $2 \text{ cm}$ ) and deeper nerves ( $1.1 \text{ cm}$ ). Hence, using the same electrode sizes on different body parts and amongst different subjects is not optimal. We recommend to adjust the used electrode size according to the expected nerve depth, the estimated fat thickness and required selectivity.

# 13

## Array Electrode Design

The aim of the work presented in this chapter was to design an array electrode that produces a similar nerve activation as a standard single electrode.

Clinically, TES is often applied in the rehabilitation of stroke subjects or spinal cord injured subjects [BMB<sup>+</sup>00], or for supporting tasks of daily living [SC07] using so called neuroprostheses. So far such neuroprostheses use single stimulation electrodes [PPK02, SMitG<sup>+</sup>00]. Array electrodes were proposed to improve efficacy of such TES systems (see section 1.1). Array electrodes consist of multiple single elements which can be individually activated to form a virtual electrode of arbitrary size and location. For good wearability textile array electrodes are produced by embroidering silver coated fibers in the form of array electrodes into garments [LPK<sup>+</sup>08]. One large layer of self-adhesive hydrogel is used as skin interface between the skin and the array electrode [KKLM07]. The gaps between array elements and the resistivity of the interface (gel) layer influence the current distribution flowing into the human limb.

In previous works the sizes of the gaps between array elements and the resistivity of the gel layer were chosen intuitively [PBBJ<sup>+</sup>05, EFP04, KKLM07]. In this chapter the TES model (see section 3.3) is used in order to analyze and better understand the influence of the gap sizes and the gel resistivity on nerve activation. Using the TES model it was investigated how large the gaps should maximally be chosen and how this decision is related to the choice of the gel resistivity.

Previously, the indifferent electrode (anode) was placed separately from the array [PBBJ<sup>+</sup>05, EFP04]. However, in [LPK<sup>+</sup>08] it was shown that active (cathode) and indifferent electrode (anode) can be placed on the same array. This simplifies the application of TES because only one electrode has to be applied to the human body instead of one array plus a separate indifferent electrode. Obviously, a part of the applied current is lost because it will directly flow from the cathode to the anode through the hydrogel. However, it is unclear how much of the applied current is lost in the gel layer depending on different parameters (e.g., gel resistivity, skin resistivity, ...). To address these issues different parameter combinations were applied to the TES model in order to quantify these losses and to possibly reduce the losses using adjusted array electrodes.

## 13.1. Methods

### 13.1.1. Combined FE and Nerve Model

Computer simulations were performed using the TES model presented in section 3.3. The cylindrical geometry with standard layer thicknesses from Table 3.2 was used. The resistivity of the skin ( $\rho_{skin}$ ) depends non-linearly on the applied current density [KKPM06]. The current densities that are typically applied are between  $1 \text{ mA/cm}^2$  and  $15 \text{ mA/cm}^2$  [LPK<sup>+</sup>08] leading to skin resistivities between  $600 \Omega\text{m}$  and  $2100 \Omega\text{m}$  (see Figure 7.3). In order to cover a wide range of these experimentally found skin resistivities low ( $700 \Omega\text{m}$ ) and high skin resistivities ( $2000 \Omega\text{m}$ ) were used in the TES model. The resistivities of the other tissues were the standard values given in Table 3.3.

The TES model was used to compare array electrodes with standard single electrodes because the aim is that nerve activation using multiple array elements is similar to using single electrodes having the same size. Therefore, two different electrode layouts were considered. In the first one, an array electrode and a single electrode were placed on the



cylinder (Figure 13.1). In the second layout, two single electrodes were used (sketch A in Figure 13.2). Between cathode and anode biphasic current regulated pulses with a pulse amplitude  $I$  and a pulse duration of  $300 \mu s$  were used.

The single elements of the array electrode had a size of 13 mm ( $l_{elem}$  in Figure 13.1), the gap sizes ( $l_{gap}$ ) were between 1 mm and 5 mm ( $l_{gap}$  in Figure 13.1), and the resistivity of the single elements was  $1.6 \cdot 10^{-8} \Omega m$  (silver). These parameters were chosen according to the specifications of array electrodes used in another study [LPK<sup>+</sup>08]. Underneath the array elements a single hydrogel layer provided an interface to the skin. This gel layer had thicknesses ( $l_{gel}$ ) between 0.25 mm and 2 mm, and resistivities ( $\rho_{gel}$ ) between  $1 \Omega m$  and  $10'000 \Omega m$ . This is the range of hydrogels that can be produced by manufactures as for example Sekisui Plastics Co., Ltd., Tokyo.

In order to compare single with array electrodes their edge lengths have to be of comparable size. The size of the single cathode ( $s$  in Figure 13.2) in the second layout (sketch A in Figure 13.2) was always adapted to the size of the corresponding 2 by 2 electrode (array) it was compared with. The edge length of the single cathode ( $s$ ) was  $s = 2 * l_{elem} + l_{gap}$ . The centers  $n_d$  of the single electrode and the 2 by 2 virtual electrode were kept congruent.

Nerve activation in the TES model was calculated using the linear MRG model (nerve model  $D^P$  in Table 3.4) and was assessed underneath the cathode (active electrode). The lowest activation using the array electrode compared to using the single electrode is underneath the gap in the center of the 2x2 active region ( $n_d$  in Figure 13.2). Because array electrodes should produce similar activation to single electrodes this location of lowest activation was investigated for two nerve depths ( $d$ ); a superficial (1 mm) and a deep nerve (16 mm) as depicted in Figure 13.3. These two nerve depths represent common extreme nerve depths found in humans [Sta05].

The experimental verification of the TES model with array electrodes that is used in this chapter is described in section 4.2.2.3.

### 13.1.2. Influence of Gel Resistivity and Array Gaps on Nerve Activation

The influence of the gaps between the single array elements on nerve activation was investigated. The aim was to find out what gel resistivities should be used for different gap sizes in order to have a small influence

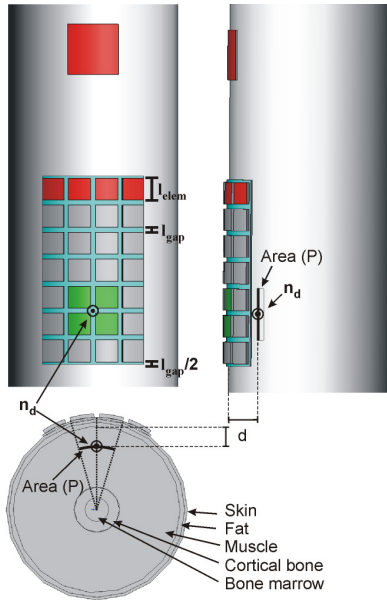


**Figure 13.1.** Cylindrical arm model with array electrode and a separate single electrode. Underneath the array one large gel layer provides the interface between array elements and skin. A region of 2x2 array elements was used as cathode and the anode (red electrode or red array elements) was either on the separate single electrode or on the array.

on nerve activation underneath the gaps compared to single electrodes. For that purpose activation generated using array geometry B (Figure 13.2) was compared with the activation generated using single electrode geometry A (Figure 13.2). The influence was quantified by calculating the additional current  $I_{add}$  that was required in the array geometry to generate the same nerve activation at locations  $n_d$  as in the single electrode geometry. The additional current  $I_{add}$  was calculated for the two nerve depths ( $d$ ) of 1 mm and 16 mm shown in Figure 13.3 and for an intermediate recruitment (11  $\mu m$  axon diameter). When axons down to a diameter of 11  $\mu m$  are activated in a nerve bundle, an intermediate recruitment of about 50% is present [RACS98].

Apart from the worst case (nerve activation underneath the gaps) the

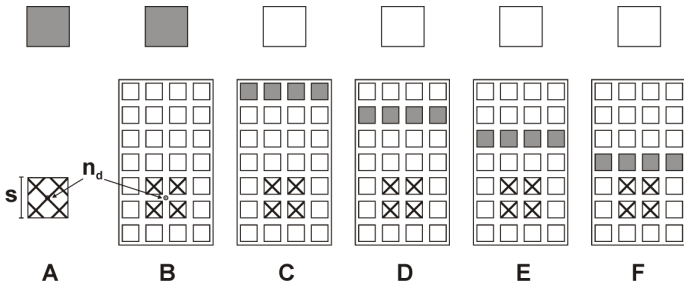


**Figure 13.2.** In the Figure grey electrodes indicate anodes and electrodes with crossed lines are the cathodes. A: two single electrodes for comparison with array electrodes. B: Array electrode with separate single anode. C to F: Arrays with anode and cathode on same array. Different distances between anode and cathode are shown (C: 51mm, D: 35mm, E: 19mm, F: 3mm).

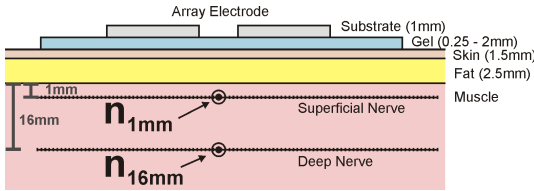


**Figure 13.3.** Superficial and deep nerve within the volume representing muscle tissue. The locations indicated with  $n_d$  are the places where nerve activation was investigated and represent common extreme nerve depths found in humans [Sta05].

mean additional current  $I_{add,area}$  of multiple locations on an area underneath the active electrodes was calculated. The area was located on cylinders that were concentric with the arm model. One of the areas on which the mean of the nerve activation was calculated is indicated with Area (P) in Figure 13.1. Two cylinder radii (corresponding to nerve depths 1 mm and 16 mm) were used in order to calculate  $I_{add,area}$  at different depths. The same two physiologically motivated nerve depths as in Figure 13.3 representing a superficial and a deep nerve were used.

### 13.1.3. Losses in the Gel Layer when Anode and Cathode are on the same Array

The losses that emerge when the cathode and the anode are on the same array were investigated. Depending mainly on parameters like gel resistivity  $\rho_{gel}$ , gel layer thickness  $l_{gel}$ , skin resistivity  $\rho_{skin}$ , and the distance between cathode and anode, a certain part of the applied current flows directly through the gel layer from cathode to anode. Our goal was to find out how high the gel resistivity  $\rho_{gel}$  should be in order to keep these losses at a low level. The losses were quantified by calculating the additional current  $I_{loss}$  that was required to generate the same nerve activation using geometries C, D, E or F (Figure 13.2) compared to geometry B (separate anode). Because the losses are larger for deeper nerves this additional current  $I_{loss}$  was calculated for a deep nerve at 16 mm nerve depth (Figure 13.3) and an intermediate nerve recruitment (11  $\mu m$  axon diameter).

## 13.2. Results

### 13.2.1. Influence of Gel Resistivity and Array Gaps on Nerve Activation

Qualitatively, the influence of gel resistivity on electrical current distribution is shown in Figure 13.4. The upper sketch shows the spreading of the current for a high resistivity (e.g., 10'000  $\Omega m$ ) of the gel layer and the lower sketch for a low resistivity (e.g., 1  $\Omega m$ ). A higher gel resistivity focuses the current underneath the single pads. As a result superficial nerves in region A are less activated compared to region D and deep nerves in region B are more activated compared to region E. In adjacent regions to the activated array elements activation is lower for high resistivities (region C) than for low resistivities (region F).

Quantitatively, the additional current  $I_{add}$  that is required to achieve the same activation with array electrodes compared to single electrodes is plotted in Figure 13.5 versus the gel resistivity  $\rho_{gel}$  for different gap sizes  $l_{gap}$  and nerve depths  $d$  as described in section 13.1.2.

It can be seen by comparing Figure 13.5(a) with Figure 13.5(b) that the influence of the gap size  $l_{gap}$  and of the gel resistivity  $\rho_{gel}$  on  $I_{add}$  is not the same for superficial and deep nerves. The curves for the different gap sizes in Figure 13.5(a) (superficial nerve) are further apart compared to the chart in Figure 13.5(b) (deep nerve). This indicates that the gap size  $l_{gap}$  has a larger influence on superficial nerves compared to

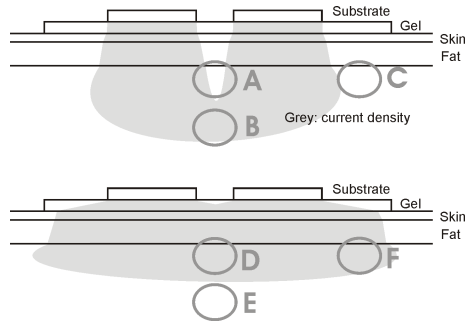


**Figure 13.4.** Depicts qualitatively the influence of different gel resistivities on the spreading of the current (grey area). The upper sketch shows the spread for a high gel resistivity (e.g.,  $10'000 \Omega m$ ) and the lower sketch for a low gel resistivity (e.g.,  $1 \Omega m$ ).

deep nerves because the current spreads out within the muscle and diminishes the influence of the array gaps on deep nerves. For low gel resistivities ( $\rho_{gel} < 20 \Omega m$ )  $I_{add}$  is large for both superficial and deep nerves. The reason is that the current spreads out in the gel layer and the effective electrode is much larger than the  $2 \times 2$  active elements on the array. For large gel resistivities ( $\rho_{gel} > 3000 \Omega m$ )  $I_{add}$  is not the same for superficial and deep nerves. Due to the small spread of the current at high gel resistivities high currents are required to activate superficial nerves underneath large array gaps ( $l_{gap} > 3.5 mm$ ). For deeper nerves also nerves underneath the gaps are activated due to the spreading of the current in the muscle.

The curves depicted in Figure 13.5 allow to choose a gel resistivity that the additional current  $I_{add}$  is minimal depending on the gap size  $l_{gap}$  of the array. For example, a gel resistivity of  $\sim 100 \Omega m$  should be used when the gap size is 5 mm and a superficial nerve is stimulated (Figure 13.5(a)). However, the results in Figure 13.5 show that these gel resistivities with minimal  $I_{add}$  are not the same for superficial and deep nerves. To equally weight superficial and deep nerves the mean of the curves in Figure 13.5(a) (superficial) and Figure 13.5(b) (deep) were calculated. These curves are shown for a skin resistivity of  $700 \Omega m$  in Figure 13.6(a) and for a skin resistivity of  $2000 \Omega m$  in Figure 13.6(b). The minimal values for the different curves in both plots of Figure 13.6 are summarized in Figure 13.7. Larger gap sizes require a larger spread

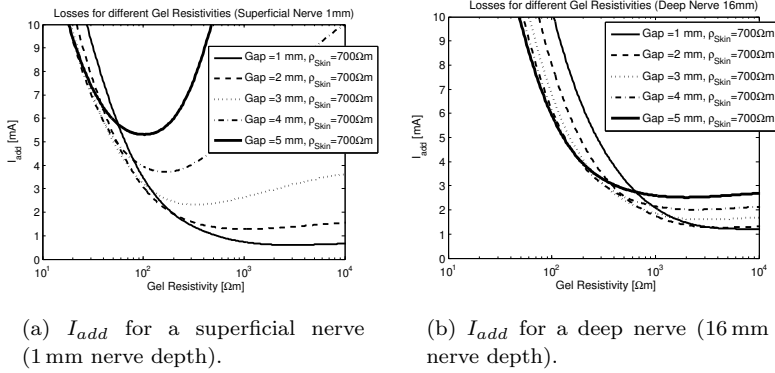


**Figure 13.5.** The additionally required current  $I_{add}$  versus the gel resistivity are shown for different parameter combinations.  $I_{add}$  was calculated between geometry B (Figure 13.2) and geometry A.

of the current in the gel layer and therefore a smaller gel resistivity (Figure 13.7). Furthermore, the results indicate that for a fixed gap size larger skin resistivities require larger gel resistivities.

The additional current  $I_{add}$  at the optimal gel resistivity for the different gap sizes (minima of each curve) in Figure 13.6 is larger for larger gap sizes (e.g.,  $I_{add}$  is 5 mA for a gap size of 5 mm but only 1 mA for a gap size of 1 mm). This indicates that lower losses can be achieved with smaller gap sizes. The results in Figure 13.6 indicate that in order to keep the additional currents  $I_{add}$  below  $\sim 2$  mA gap sizes below  $\sim 3$  mm are required.

Apart from the worst case (nerve underneath the gaps) the mean additional current  $I_{add,area}$  underneath the array was calculated (see section 13.1.2). The losses are much lower (Table 13.1) compared to the worst cases in Figure 13.5. For all tested gap sizes and nerve depths the losses were 4 mA or lower (Table 13.1).

### 13.2.2. Losses in the Gel Layer when Anode and Cathode are on the same Array

The losses  $I_{loss}$  versus the gel resistivity  $\rho_{gel}$  were calculated for different cathode-anode distances, skin resistivities  $\rho_{skin}$  (Figure 13.8), and gel thicknesses  $l_{gel}$  (Figure 13.9) as described in section 13.1.3.

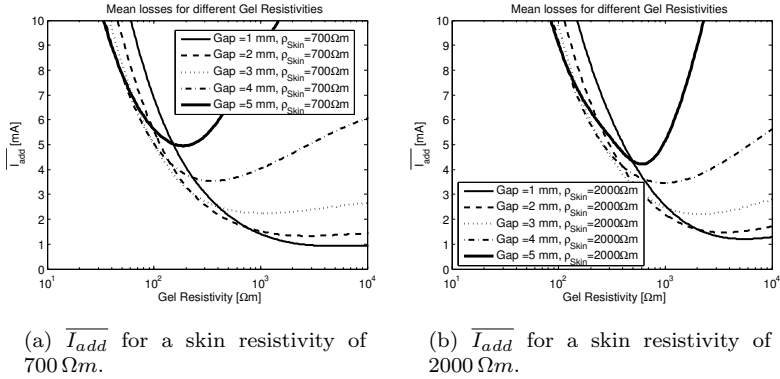


**Figure 13.6.** Mean of  $I_{add,superficial}$  (Figure 13.5(a)) and  $I_{add,deep}$  (Figure 13.5(b)) (denoted with  $\overline{I_{add}}$ ) versus the gel resistivity are shown for different gap sizes.

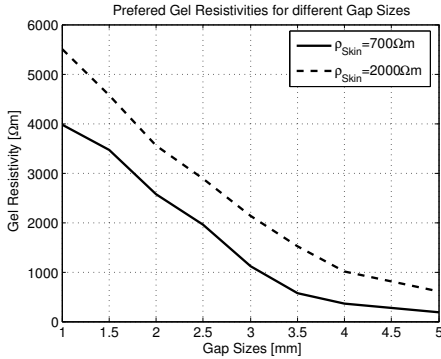


**Figure 13.7.** The plot gives the gel resistivities that should be preferred for different gap sized of the array. The values were derived from the minimas of the curves in Figure 13.6.

For lower  $\rho_{gel}$  the losses  $I_{loss}$  increased because a larger part of the current flew directly through the gel layer and did not add to nerve activation (Figure 13.8 and 13.9). A limit for  $I_{loss}$  of 2mA was introduced in order to obtain lower limits for the gel resistivities where

No.	Gap Size $l_{gap}$ [mm]	Nerve Depth $d$ [mm]	Mean Additional Current $I_{add,area}$ [mA]
1	1	1	<b>0.4</b>
2	2	1	<b>0.6</b>
3	3	1	<b>0.8</b>
4	4	1	<b>1.2</b>
5	5	1	<b>1.6</b>
6	1	16	<b>1.6</b>
7	2	16	<b>1.8</b>
8	3	16	<b>2</b>
9	4	16	<b>3.2</b>
10	5	16	<b>4</b>

**Table 13.1.** Mean additional current  $I_{add,area}$  for different gap sizes and nerve depths. The skin resistivity  $\rho_{skin}$  was  $2000\ \Omega m$  and the gel resistivity  $\rho_{gel}$  was  $3000\ \Omega m$ .

losses are at an acceptable level. Losses of 2 mA are acceptable because the additional current does not introduce much more pain [LLCM<sup>+</sup>04] and does not require much more power from the stimulator. For short cathode-anode distances (3 mm) the losses were above 2 mA (Figure 13.8). Therefore, cathode-anode distances below  $\sim 19\ mm$  should be avoided when on the same gel layer. For cathode-anode distances above 19 mm the losses  $I_{loss}$  were below 2 mA for gel resistivities  $\rho_{gel}$  above  $50\ \Omega m$ .

The larger skin resistivity  $\rho_{skin}$  of  $2000\ \Omega m$  required a slightly larger gel resistivity  $\rho_{gel}$  to produce the same losses  $I_{loss}$  (Figure 13.8). However, compared to the cathode-anode distance and the gel resistivity, the skin resistivity has a smaller influence on the losses.

The results in Figure 13.9 show that thicker gel layers produce larger losses and that the influence of the gel thicknesses on the losses is larger for low gel resistivities. However, because gel resistivities above  $50\ \Omega m$  should be used as described in the two previous paragraphs the results show that there is only a little gain using thinner gel layers.

In summary, these results show that for cathode-anode distances larger than 19 mm and gel resistivities  $\rho_{gel}$  above  $50\ \Omega m$  the losses are below 2 mA for all tested combinations of parameters (Figure 13.8). This defines a lower limit for the cathode-anode distance and the gel resistivity  $\rho_{gel}$  when cathode and anode are supposed to be on the same array.



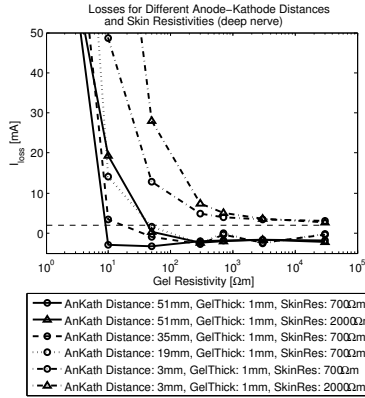


**Figure 13.8.** The losses  $I_{loss}$  versus the gel resistivity are shown for different cathode-anode distances and skin resistivities. The nerve depth was 16 mm and the gap sizes were 3 mm.

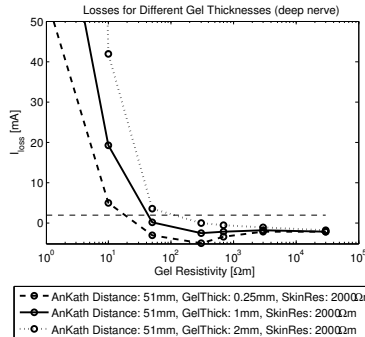


**Figure 13.9.** The losses  $I_{loss}$  versus the gel resistivity are shown for different gel thicknesses. The nerve depth was 16 mm and the gap sizes were 3 mm.

### 13.3. Discussion

The array technology is a versatile approach that can dynamically change the size and position of the active region of a stimulation electrode. This approach shortens the time-consuming procedure of finding optimal electrode positions and sizes. However, it was unclear how the

gaps between the array elements and the resistivity of the interface layer (gel resistivity) influence activation. Furthermore, it was unclear how big the losses are when cathode and anode are placed on the same array connected by the gel layer. A combined FE and nerve model was employed to clarify what gel resistivities and gap sizes should be used. A modeling approach was favored over experiments because it has the advantage that specific influences and parameter ranges can be investigated. With experiments only the number of different configurations that can be investigated would be very limited.

The simulation results with gap sizes between 1 mm and 5 mm indicated that low resistivities lead to a large spread of the current within the gel layer. As a consequence the area where the current enters the skin is larger than the area of a single array element. The advantage of the large spread is that the activation is more uniform and that gaps have less influence. However, the selectivity is reduced. On the other hand the results show that a too high gel resistivity dramatically reduces activation underneath the gaps of the array because the current flows perpendicular down into the muscle and does not reach nerves located directly underneath the gaps. As a consequence for high gel resistivities the activation is non-uniform but selective. For these reasons the gel resistivity is an important design parameter that has to be properly chosen depending on the gap sizes of the constructed array electrode (Figure 13.7) in order to achieve a good tradeoff between uniformity and selectivity activation. Because the skin resistivity of most humans is between  $700 \Omega m$  and  $2000 \Omega m$  [RACS98, KKPM06] the gel resistivity should be chosen between the two curves depicted in Figure 13.7.

Apart from the nerve activation underneath the gaps of the array also the mean losses under the whole electrode were calculated. These losses were smaller compared to the losses underneath the gaps (Table 13.1). This gives evidence that only few places have a lower activation (primarily underneath gaps). However, for automatic identification algorithms that find optimal stimulation regions [KHLK06] it is important that all locations underneath the electrodes experience similar activations. Therefore, it can be important to produce a uniform current distribution underneath the array.

The simulation results where cathode and anode were on the same gel layer (section 13.2.2) showed that the gel resistivity should be at least  $50 \Omega m$  and the cathode-anode distances should be above 19 mm in order to keep losses below 2 mA. The requirement that the gel resistivity should be above  $50 \Omega m$  is less restrictive than the gel resistivities that

produce minimal losses for different gap sizes (see Figure 13.7). Hence, it is sufficient to ensure that cathode and anode are never closer than about 20 mm in order to keep losses at a low level when anode and cathode are on the same interface layer.

A thinner gel layer thickness decreases the losses when anode and cathode are on the same gel layer (Figure 13.9). However, the effect of using a larger gel resistivity was found to be more effective (Figure 13.9) compared to a thinner gel layer thickness. Additionally the gel layer thickness should not be thinner than 1 mm due to safety reasons. When using current regulated stimulation a break through of the interface material can cause skin burns.

The presented gap sizes and gel resistivities with minimal additional current were calculated for parameters of a common human forearm (see Figure 13.7). If an array electrode that was produced using such standard arm parameters is applied to other body parts the losses will not have a minimal additional current. The main parameters that change when moving to other body parts are the nerve depth and the fat layer thickness. A thicker fat layer has a comparable effect as a deeper nerve because the nerves are also farther away from the stimulating electrode. The effect of a deeper nerve can be estimated by comparing Figure 13.5(a) with Figure 13.6(a). In the results of Figure 13.6(a), both superficial and deep nerves are taken into account whereas in Figure 13.5(a) only the superficial nerves are taken into account. The optimal gel resistivities moved towards higher values when incorporating deeper nerves. However, the changes were low (e.g., for a gap size of 3 mm from  $400 \Omega m$  to  $1000 \Omega m$ ) compared to the whole range of possible gel resistivities for different gap sizes given in Figure 13.7. This indicates that the gap size is the dominant parameter and that other parameters and therefore also different body locations (arm, leg,...) have a minor influence on the optimal gel resistivity.

In conclusion, for a good trade-off we suggest, based on the simulation results, that gap sizes should be smaller than 3 mm in order to have losses below 2 mA. For 3 mm gap sizes the preferred gel resistivity was  $\sim 1500 \Omega m$ , for 2 mm gap sizes  $\sim 3000 \Omega m$ , and for 1 mm gap sizes  $\sim 4500 \Omega m$  (see Figure 13.7).



Part V

**CONCLUSIONS AND  
OUTLOOK**



## Summary and Conclusions

A TES model comprising a finite element model and non-linear nerve models was developed (section 3.3) with the aim to investigate new TES technologies and to better understand specific effects in TES. With the TES model nerve activation was calculated either in nerve bundles or by using activation volumes (AVs) which describe whole regions where nerves are activated. Quantitative measures to estimate the activation depth and the selectivity were derived from activation volumes (section 3.4.2).

The developed TES model was first verified with experiments and then used for different investigations. The main conclusions that were drawn throughout this thesis project are summarized below.

### Comparison of the TES model with experiments

- Strength-duration curves and recruitment-duration curves calculated by the TES model containing axon model D (MRG) compared well with experiments. Until now axon model D (MRG-model) was exclusively used for implanted ES systems [LGD06]. With the presented investigation it was shown that the MRG-model can also be used to model transcutaneous ES where the electrode-nerve distances are much larger than in implanted systems (section 4.3).

### Tissue properties

- The high variability of the bulk tissue capacitances were found to have a minor influence on recruitment in TES. Therefore, the Laplace equation can be used to describe the potential distribution in the volume conductor. However, there are cases where the time varying solution has to be used. These cases were discussed in section 7.1.
- The non-linearity of the skin resistivity can be neglected if only nerve activation is of interest. However, if the voltage on the electrodes is also of importance the non-linearity of the skin has to be incorporated (section 7.2.1).
- The skin and fat resistivities were found to have little influence on nerve activation when using current-regulated TES. This is an

advantage for the practical application of current regulated TES, because similar stimulation parameters can be used for different persons (section 7.2.2).

- An anatomical geometry was segmented from MRI scans and included in the TES model. Nerve activation in a TES model using a multiple layer cylindrical geometry was compared with a TES model using an anatomical geometry. This comparison showed that a simplified multiple layer cylindrical geometry can be used to describe nerve activation during TES in human forearms (section 7.3).
- The influence of bone and other inhomogeneities on nerve activation is small if there is at least a distance of 0.8 cm for large inhomogeneities (1 cm diameter) and a distance of 0.3 cm for small inhomogeneities (0.2 cm diameter) between nerve and inhomogeneity. This result helps to decide which inhomogeneities can be neglected in TES models (section 7.4).
- In summary, the results of the sensitivity analysis show that the *muscle resistivity*, the *axon depth*, and the *axon diameter* have the largest influences on nerve activation. The big influence of the axon depth also implies that the large range of fat thicknesses found in humans has a large influence on nerve activation. In general, the parameters with a large influence have to be incorporated in TES models whereas parameters with a small influence on nerve activation can be neglected or approximated in TES models (section 9).

## Electrode material

- The higher current densities at the edge of surface electrodes compared to the center of the electrodes (edge effects) can be reduced by using a higher electrode gel resistivity (section 11).
- Locally high current densities occurring from large skin inhomogeneities (1 cm diameter) can be reduced with high resistive electrodes. Locally high current densities that are due to small inhomogeneities (100  $\mu\text{m}$  diameter) cannot be reduced using high resistive electrodes. This indicates that high resistance electrodes are not a solution to improve the comfort in TES (section 11).



- Experimental measurements and simulations using the TES model show that the resistivity of the electrode material does not influence the motor thresholds. However, the comfort (pain threshold) is strongly influenced by the choice of electrode material over a wide range of current densities. This means that new electrode materials can be designed with the focus on optimizing stimulation comfort without compromising stimulation magnitude (section 12.2).

### Electrode size

- Comfort and selectivity of different electrode sizes were calculated with the TES model for different fat layer thicknesses and nerve depths. Optimized electrode sizes which produced maximal selectivity and comfort for different anatomies were identified. The sizes varied between  $0.8 \times 0.8 \text{ cm}^2$  and  $4.1 \times 4.1 \text{ cm}^2$  depending on the anatomy (fat thickness, nerve depth). Hence, using the same electrode sizes on different body parts and amongst different subjects is not optimal. It is recommended to adjust the used electrode size according to the expected nerve depth, the estimated fat thickness and the required selectivity (section 12.3).

### Array electrodes

- Simulation results show that by adequately choosing array gap sizes and gel resistivities, activation of single electrodes can be mimicked using array electrodes. It is suggested, based on the simulation results, that gap sizes should be smaller than 3 mm in order to have losses below 2 mA. For 3 mm gap sizes the preferred gel resistivity was  $\sim 1500 \Omega m$ , for 2 mm gap sizes  $\sim 3000 \Omega m$ , and for 1 mm gap sizes  $\sim 4500 \Omega m$  (section 13).

## Outlook

One of the main questions in modeling is the level of detail that is incorporated in a model. In the Electrical Stimulation Group at the Automatic Control Lab (ETH Zurich) the presented TES model was used to answer specific technological design questions (e.g. electrode resistance, array electrode design) or to better understand different influences on TES (e.g. skin resistivity, nerve depth). For such applications detailed and computationally expensive models were required. However, certain model simplifications were possible as presented in chapter 9. The further development of the TES model depends on future applications. Two main directions are possible:

- If the aim is to find, for example, optimized activation regions (on array electrodes) for new neuroprostheses, a more detailed TES model is required. The results in section 7.3 (anatomically based geometry) indicate that a multiple layer cylindrical volume conductor model should be sufficient to describe the potential distribution within the arm (we believe that for certain studies even simpler cube shaped models can be used). The model improvement would be to include a more realistic nerve bundle model (morphology, curvature). Currently, all nerve bundles are oriented in the same direction (in axial direction of the cylindrical model). By incorporating a detailed network of axons as for example done in [KDR<sup>+</sup>07] the selective activation of specific muscles can be better analyzed.
- If the future direction is to use the model in a real-time environment (e.g. to dynamically change the electrode size in a neuroprosthesis based on real-time simulation results), a much simplified model is required. The volume conductor model could be replaced with an analytical model as for example introduced by Livshitz [LEM01] or more recently by Mesin [MM08]. By using the AF to predict nerve activation based on the potential distribution it should be possible to implement a model that can be solved in real-time. Also look-up tables can be an option in certain cases. The main challenge to be solved would be the changing activation due to the movements of the motor points when the arm is, for example, supinated or pronated. Sensors have to measure these movements and correct the model for the changed motor point locations.

Further points that are not related to the level of detail of the TES model:

- We were not able to directly validate the shape of activation volumes. Co-contractions of adjacent muscles to the targeted muscle did not allow an accurate measurement on human volunteers. An in-vitro setup or animal experiments would be required in order to validate the shape of activation volumes.
- The current version of the TES model only includes motor nerves. In section 12.3 a pain index was used to conclude on stimulation comfort. However, the actual sensory nerves are not included in the TES model. It would be interesting to see how the fiber diameter distribution influences the required pulse duration for motor and sensory nerve excitation. This could help to find stimulation pulses that maximize motor nerve activation and minimize sensory nerve activation.



Part VI

**APPENDIX**



# A

## Anatomy (Muscles in the Forearm)

### A.1. Flexors in the Forearm

#### Deepest Layer

- m. Supinator* The supinator muscle is the main muscle that supinates the arm, rotates the radius. The muscle originates at the proximal part of the ulna and the very distal part of the humerus. The insertion is at the proximal third of the radius. The deep branch of the radial nerve (C7,C8) innervates the Supinator muscle.
- m. Pronator Quadratus* This small, quadrangular muscle is, amongst others, responsible for the opposite movement of the *m. supinator*, pronation. It originates at the distal fourth of the anterior surface of the ulna, the insertion is at the distal fourth of the anterior surface of the radius. Innervation of the muscle comes from the anterior interosseous nerve which is a branch of the medial nerve (C8,T1).

## Deep Flexors

***Flexor Digitorum Profundus*** M. flexor digitorum profundus finds its origin at the proximal end of anterior side of the proximal quarter of the medial and anterior surfaces of the ulna. Its insertion lies on the basis of the distal phalanges of the medial four fingers. The muscle can flex the distal interphalangeal joints of the fingers; the DIP, PIP and MPC joint of the fingers. The muscle is innervated by the medial part of the ulnar nerve (C8,T1) and the lateral part of the median nerve (C8,T1).

## Intermediate Layer of Flexors

***m. Flexor Digitorum Superficialis (FDS)*** The muscle has two heads, the humeroulnar head and the radial head. The first is attached to the medial epicondyle of the humerus and the coronoid process of the ulna. The latter of the two heads attaches to the superior half of the anterior border of the radius. The m. flexor digitorum superficialis gives rise to four tendons, each serving one of the fingers. Its insertion lies on the middle phalanges of the medial four digits, the four fingers. This means it can flex the proximal interphalangeal joints, together with the metacarpophalangeal joints and the wrist joint. Innervation of the muscle comes from the median nerve (C7,C8,T1).

## Superficial Layer of Flexors

***m. Flexor Carpi Radialis (FCR)*** The proximal attachments of this muscle lie on the medial epicondyle of the humerus, its insertion is at the base of the 2nd and 3rd metacarpal bone. Therefore the muscle is suitable for flexion and abduction of the wrist. Innervation is by the median nerve (C7,C8). It is a muscle with a slim belly and a very long tendon which takes it to the metacarpal bones.

***m. Palmaris Longus (PL)*** The Palmaris Longus is a muscle that can flex the wrist and tens the palmar fascia. It originates at the medial epicondyle of the humerus, inserts at the proximal superficial palmar fascia and is innervated by the median nerve (C7,C8).



***m. Flexor Carpi Ulnaris (FCU)*** The most medial of the superficial flexors of the forearm is the m. flexor carpi ulnaris, which is responsible for flexion of the wrist joint and adduction of the hand. The proximal attachments of the muscle are for the humeral head, the medial epicondyle of the humerus and for the ulnar head, the olecranon and the posterior border of the ulna. Distally the muscle attaches to the two carpals and the metacarpal of the fifth digit. The muscle is innervated by the ulnar nerve (C7,C8).

## A.2. Extensors in the Forearm

The muscles for the extension of the fingers are situated on the posterior side of the forearm.

***m. Extensor Digitorum*** A muscle innervated by the posterior interosseous nerve (C7,C8) and a branch of the radial nerve. Its function is to extend the fingers and the wrist.

***m. Extensor Digiti Minimi*** Innervated by the same nerves as the m. extensor digitorum. The function is to extend the proximal phalanx of the fifth digit (the little finger) at the metacarpophalangeal joint and to assist in the extension of the carpometacarpal joints, the wrist.

***m. Extensor Carpi Ulnaris Muscle*** A two headed muscle which attaches at the base of the fifth metacarpal bone. Innervated by the posterior interosseous nerve (C7,C8) and a branch of the radial nerve. The m. extensor carpi ulnaris can extend and adduct the hand at the wrist.

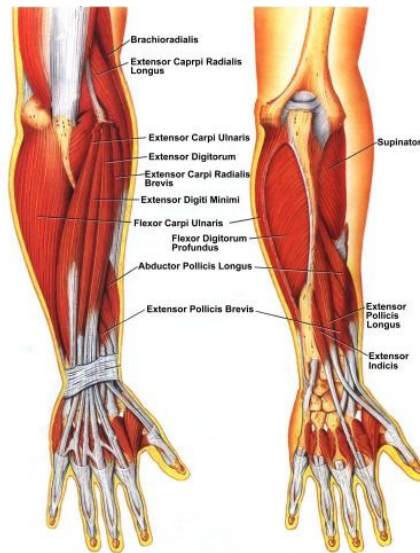


**Figure A.1.** The muscles on the posterior side of the forearm. [Sta05]

# B

## ArmSimP

**What is ArmSimP?** ArmSimP (Arm Simulation Program) is a Software-Package to build, simulate and manage TES models. It was developed in order to simplify and accelerate the simulation process. ArmSimP was designed using an object oriented approach in order to enable future extension.

Detailed descriptions of ArmSimP can be found in a technical report [Kuh05] and in different semester project reports [Bas05, AB07, Man07]. Here only a summary of the main functionality is provided.

**Main Steps performed in ArmSimP** ArmSimP was designed to perform the three main steps (volume conductor, nerve model, post-processing) that are required for TES models (see Figure B.1). These are the same steps that were introduced in chapter 3 (Figure 3.1).

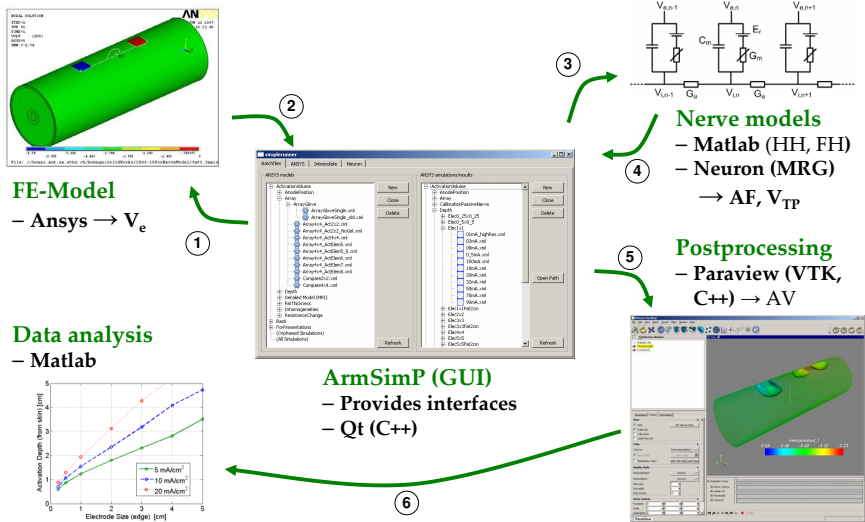
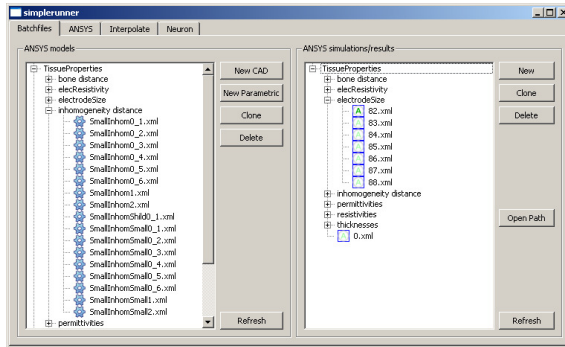


Figure B.1. Summarizes the main procedure that is conducted in ArmSimP.

## Main Functionality

### TES Model Management

- The model and simulation parameters are stored in a folder structure (see Figure B.2).
- The geometry for the FE simulations can either be CAD data or the parametric model (cylindrical geometry), which provides a set of parameters (see Figure B.3).



**Figure B.2.** Simulation parameters and models can be stored in a folder structure. The left list holds the items containing the geometry and the corresponding parameters (tissue properties, tissue thicknesses, ...). The right list contains simulation parameters like pulse amplitude or the specification of the active elements on array electrodes.

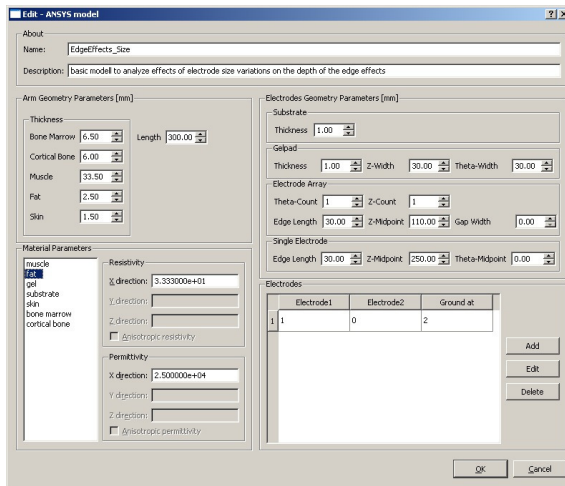


**Figure B.3.** The parametric models can be specified with a set of predefined parameters. It is a cylindrical model that can model both single and array electrodes.

- Single and array electrodes can be placed on the geometry.
- Stimulation parameters (pulse amplitude, pulse width, ...) can be set.
- When modeling array electrodes an arbitrary number of array elements can be combined to a virtual electrode. Any number of virtual electrodes can be defined which are connected to an arbitrary number of current sources. For each current source stimulation pulse parameters can be individually chosen.

### **FE Simulation**

- The defined model is sent to ANSYS (EMAG, Ansys Inc., Canonsburg, PA) in order to calculate the electrical potential distribution within the geometry (compare to section 3.1.5).
- Batchprocessing of multiple models is possible.
- The resulting electrical potentials are interpolated onto nerve lines which can be specified in ArmSimP.
- The simulation results with all parameters are stored in a data structure.

### **Nerve Model**

- Calculate the TP (activation distribution) using a linear or non-linear nerve model (compare to section 3.2).

### **Postprocessing**

- Construct activation volumes (AVs) based on the activation distribution (compare to section 3.4.2.1).
- Compare two activation volumes with each other using mean distances (compare to section 5.1.3).
- Calculate activation depth and selectivity based on the activation volume (compare to sections 3.4.2.2 and 3.4.2.4).
- Calculate strength-duration curves and derive chronaxie and rheobase (compare to section 4.2.1.3).
- Calculate recruitment-duration curves and its rise time (compare to section 4.3.1.3).

## Used Software Packages

- Visual Studio 2005 (8.0) (Used to compile Paraview)
- Cmake 2.4.1 (makefile generation for various platforms)
- Tortoise CVS (to download the vtk and paraview source)
- Tortoise SVN (for ckecking out and committing changes to the custom source code)
- Ansys (for FE simulations)
- Matlab (for AF calculation (second derivative), curve fitting)
- Neuron (simulate nerve activation)
- Qt with MinGW (for the compilation of the user interface of ArmSimP)
- Paraview (for Postprocessing, display activation volume (AV))
- paraviewFES (custom VTK functions which are included in Paraview)
- Cygwin 1.5.9 (used for moving and deleting data in ArmSimP)
- Perl





## Bibliography

- [AB07] S. Axmann and S. Berg. Untersuchung neuer Stimulationsmethoden mittels Muskel- und Nervensimulationen. *IFA Semester Project*, 2007. 187
- [AKH94] G. Alon, G. Kantor, and H. S. Ho. Effects of electrode size on basic excitatory responses and on selected stimulus parameters. *J Orthop Sports Phys Ther*, 20(1):29–35, 1994. 48, 131, 146, 150, 152, 155, 157
- [Bas05] M. Baschnagel. Programmpaket zur Analyse von transkutaner Elektrostimulation mit Potential- und Nervenmodellen. *IFA Semester Project*, 2005. 187
- [BCHM07] C. R. Butson, S. E. Cooper, J. M. Henderson, and C. C. McIntyre. Patient-specific analysis of the volume of tissue activated during deep brain stimulation. *Neuroimage*, 34(2):661–70, 2007. 86
- [BJ87] T. J. Bajzek and R. J. Jaeger. Characterization and control of muscle response to electrical stimulation. *Ann Biomed Eng*, 15(5):485–501, 1987. 65
- [BK04] N. Bhadra and K. L. Kilgore. Direct current electrical conduction block of peripheral nerve. *IEEE Trans Neural Syst Rehabil Eng*, 12(3):313–24, 2004. 56
- [BM05] C. R. Butson and C. C. McIntyre. Tissue and electrode capacitance reduce neural activation volumes during deep brain stimulation. *Clin Neurophysiol*, 116(10):2490–500, 2005. 86
- [BM06] C. R. Butson and C. C. McIntyre. Role of electrode design on the volume of tissue activated during deep brain stimulation. *J Neural Eng*, 3(1):1–8, 2006. 44, 72, 74, 79
- [BMB<sup>+</sup>00] L. L. Baker, D. R. McNeal, L.A. Benton, B. R. Bowman, and R. L. Waters. *Neuro muscular electrical stimulation*. 4 edition, 2000. 19, 22, 65, 149, 159

- [Bos83] H. Bostock. The strength-duration relationship for excitation of myelinated nerve: computed dependence on membrane parameters. *J Physiol*, 341:59–74, 1983. 56
- [CBM07] L. W. Chou and S. A. Binder-Macleod. The effects of stimulation frequency and fatigue on the force-intensity relationship for human skeletal muscle. *Clin Neurophysiol*, 118(6):1387–96, 2007. 67
- [CC98] S. E. Crook and P. H. Chappell. A portable system for closed loop control of the paralysed hand using functional electrical stimulation. *Med Eng Phys*, 20(1):70–6, 1998. 72, 149
- [CCD01] A. Q. Choi, J. K. Cavanaugh, and D. M. Durand. Selectivity of multiple-contact nerve cuff electrodes: a simulation analysis. *IEEE Trans Biomed Eng*, 48(2):165–72, 2001. 41, 114, 115, 116, 117
- [CIK<sup>+</sup>98] Y. A. Chizmadzhev, A. V. Indenbom, P. I. Kuzmin, S. V. Galichenko, J. C. Weaver, and R. O. Potts. Electrical properties of skin at moderate voltages: contribution of appendageal macropores. *Biophys J*, 74(2 Pt 1):843–56, 1998. 7, 132
- [CLE95] M. A. Camacho, J. L. Lehr, and S. R. Eisenberg. A 3-dimensional finite-element model of human transthoracic defibrillation - paddle placement and size. *Ieee Transactions on Biomedical Engineering*, 42(6):572–578, 1995. 150
- [CO04] M.J. Callaghan and J.A. Oldham. Electric muscle stimulation if the quadriceps in the treatment of patellofemoral pain. *Arch Phys Med Rehabil*, 85:956–62, 2004. 4
- [Cob85] B. Coburn. A theoretical study of epidural electrical stimulation of the spinal cord—part ii: Effects on long myelinated fibers. *IEEE Trans Biomed Eng*, 32(11):978–86, 1985. 5, 6, 7, 150
- [CPMVdM74] P. E. Crago, P. H. Peckham, J. T. Mortimer, and J. P. Van der Meulen. The choice of pulse duration for chronic

- electrical stimulation via surface, nerve, and intramuscular electrodes. *Ann Biomed Eng*, 2(3):252–64, 1974. 65
- [CRRS79] S. Y. Chiu, J. M. Ritchie, R. B. Rogart, and D. Stagg. A quantitative description of membrane currents in rabbit myelinated nerve. *J Physiol*, 292:149–66, 1979. 39, 40, 42, 56
- [CS85] B. Coburn and W. K. Sin. A theoretical study of epidural electrical stimulation of the spinal cord—part i: Finite element analysis of stimulus fields. *IEEE Trans Biomed Eng*, 32(11):971–7, 1985. 114
- [DR99] S. J. Dorgan and R. B. Reilly. A model for human skin impedance during surface functional neuromuscular stimulation. *IEEE Trans Rehabil Eng*, 7(3):341–8, 1999. 7, 28, 35, 54, 89, 90, 91
- [Ede71] R. Edelberg. *Electrical properties of the skin*. Wiley-Interscience, New York, 1071. 28
- [EFP04] A. Elsaify, J.C. Fothergill, and W. Peasgood. A portable fes system incorporating an electrode array and feedback sensors. In *Vienna Int. Workshop on Functional Electrostimulation*, volume 8, pages 191–4, 2004. 5, 160
- [EH79] E. Eriksson and T. Haggmark. Comparison of isometric muscle training and electrical stimulation supplementing isometric muscle training in the recovery after major knee ligament surgery. a preliminary report. *Am J Sports Med*, 7:169–71, 1979. 5
- [FH64] B. Frankenhaeuser and A. F. Huxley. The action potential in the myelinated nerve fiber of *xenopus laevis* as computed on the basis of voltage clamp data. *J Physiol*, 171:302–15, 1964. 39, 41
- [Fit62] R. Fitzhugh. Computation of impulse initiation and saltatory conduction in a myelinated nerve fiber. *Biophys J*, 2:11–21, 1962. 56

- [FS89] K. R. Foster and H. P. Schwan. Dielectric properties of tissues and biological materials: a critical review. *Crit Rev Biomed Eng*, 17(1):25–104, 1989. 27, 35, 36
- [GDB07] C. M. Gregory, W. Dixon, and C. S. Bickel. Impact of varying pulse frequency and duration on muscle torque production and fatigue. *Muscle Nerve*, 35(4):504–9, 2007. 65
- [Ged72] Leslie Alexander Geddes. *Electrodes and the measurement of bioelectric events*. Wiley-Interscience, New York etc., 1972. 48
- [Ged04] L. A. Geddes. Accuracy limitations of chronaxie values. *IEEE Trans Biomed Eng*, 51(1):176–81, 2004. 56
- [GK98] D. Graupe and K. H. Kohn. Functional neuromuscular stimulator for short-distance ambulation by certain thoracic-level spinal-cord-injured paraplegics. *Surg Neurol*, 50(3):202–7, 1998. 5
- [GLG96] S. Gabriel, R. W. Lau, and C. Gabriel. The dielectric properties of biological tissues: Iii. parametric models for the dielectric spectrum of tissues. *Phys Med Biol*, 41(11):2271–93, 1996. 7, 35, 36, 85, 104
- [Gri84] S. Grimnes. Pathways of ionic flow through human skin in vivo. *Acta Derm Venereol*, 64(2):93–8, 1984. 7, 132
- [Gri99] Jr. Grill, W. M. Modeling the effects of electric fields on nerve fibers: influence of tissue electrical properties. *IEEE Trans Biomed Eng*, 46(8):918–28, 1999. 107, 114
- [GT75] F. Gracanic and A. Trnkoczy. Optimal stimulus parameters for minimum pain in the chronic stimulation of innervated muscle. *Arch Phys Med Rehabil*, 56(6):243–9, 1975. 149
- [Har71] R. Harris. Chronaxy. In Licht S., editor, *Electrodiagnosis and Electromyography*, pages 218–239. Baltimore, 1971. 56, 60, 143

- [HH52] A. L. Hodgkin and A. F. Huxley. A quantitative description of membrane current and its application to conduction and excitation in nerve. *J Physiol*, 117(4):500–44, 1952. 6, 39, 42
- [HYL<sup>+</sup>98] Y. Hu, J. Yu, K. D. K. Luk, Y. W. Wong, W. W. Lu, and J. C. Y. Leong. Modeling of the current density distribution under surface poster-tibial-nerve electric stimulator. *Proceedings of the 20th Annual International Conference of the IEEE Engineering in Medicine and Biology Society*, 20(6):2991–3, 1998. 6, 7
- [ITitG<sup>+</sup>96] M.J. Ijezerman, Stoffers T.S., F.A.C.G. in 't Groen, M.A.P. Klatte, G.J. Snoeck, J.H.C. Vorsteveld, R.H. Nathan, and H.J. Hermens. The ness handmaster orthosis: restoration of hand function in c5 and stroke patients by means of electrical stimulation. *J Rehab Sci*, 9(3):86 – 9, 1996. 5
- [JM05] S. Jezernik and M. Morari. Energy-optimal electrical excitation of nerve fibers. *IEEE Trans Biomed Eng*, 52(4):740–3, 2005. 54, 88
- [JNT83] J.B. Jack, D. Noble, and R.W. Tsien. *Electric Current Flow in Excitable Cells*. Oxford University Press, London/New York, 1983. 37
- [KBAB00] M. C. Kiernan, D. Burke, K. V. Andersen, and H. Bostock. Multiple measures of axonal excitability: a new approach in clinical testing. *Muscle Nerve*, 23(3):399–409, 2000. 56, 60, 143
- [KBM06] T. Kesar and S. Binder-Macleod. Effect of frequency and pulse duration on human muscle fatigue during repetitive electrical stimulation. *Exp Physiol*, 91(6):967–76, 2006. 65
- [KBO<sup>+</sup>04] S. Kuwabara, H. Bostock, K. Ogawara, J. Y. Sung, S. Misawa, Y. Kitano, K. Mizobuchi, C. S. Lin, and T. Hattori. Excitability properties of human median axons measured at the motor point. *Muscle Nerve*, 29(2):227–33, 2004. 58, 59

- [KDR<sup>+</sup>07] J. H. Kim, J. B. Davidson, O. Rohrle, T. K. Soboleva, and A. J. Pullan. Anatomically based lower limb nerve model for electrical stimulation. *Biomed Eng Online*, 6:48, 2007. 178
- [KHLK06] T. Keller, B. Hackl, M. Lawrence, and A. Kuhn. Identification and control of hand grasp using multi-channel transcutaneous electrical stimulation. In *International Functional Electrical Stimulation Society Conference*, volume 11, pages 29–31, Zao, Japan, 2006. 170
- [KK05] A. Kuhn and T. Keller. A 3d transient model for transcutaneous functional electrical stimulation. In *International Functional Electrical Stimulation Society Conference*, volume 10, pages 385–7, Montreal, Canada, 2005. 36
- [KK06] A. Kuhn and T. Keller. The influence of capacitive properties on nerve activation in transcutaneous electrical stimulation. In *International Symposium on Computer Methods in Biomechanics and Biomedical Engineering*, volume 7, Antibes, France, 2006. 29
- [KK07] A. Kuhn and T. Keller. A model for transcutaneous electrical stimulation using activation volumes to describe the influence of the electrode placement and size. In *Vienna Int. Workshop on Functional Electrostimulation*, volume 9, pages 151–4, 2007. 149, 150
- [KKLM07] T. Keller, A. Kuhn, M. Lawrence, and M. Morari. Textile neuroprosthesis garment for functional electrical stimulation. In *Vienna Int. Workshop on Functional Electrostimulation*, volume 9, 2007. 149, 151, 159, 160
- [KKPM06] A. Kuhn, T. Keller, B. Prenaj, and M. Morari. The relevance of non-linear skin properties for a transcutaneous electrical stimulation model. In *International Functional Electrical Stimulation Society Conference*, volume 11, Zao, Japan, 2006. 48, 53, 160, 170
- [KLK07] T. Keller, M. Lawrence, and A. Kuhn. Selective finger and wrist activation using multi-channel transcutaneous electrical stimulation electrodes. In *Interna-*

- tional Functional Electrical Stimulation Society Conference*, volume 12, Philadelphia, PA USA, 2007. 114
- [KLKM06] T. Keller, M. Lawrence, A. Kuhn, and M. Morari. New multi-channel transcutaneous electrical stimulation technology for rehabilitation. In *Annual International Conference of the IEEE Engineering in Medicine and Biology Society (IEEE Cat. No. 06CH37748)*, pages 184–7, 2006. 5, 149
- [KLT03] T. Kirstein, M. Lawrence, and G. Tröster. Functional electrical stimulation (FES) with smart textile electrodes. In *International workshop on a new generation of wearable systems for e-health*, Pisa, Italy, 2003. 5
- [KPA<sup>+</sup>00] T. Keller, M.R. Popovic, M. Amman, C. Andereggen, and C. Dumont. A system for measuring finger forces during grasping. In *International Functional Electrical Stimulation Society Conference*, Aalborg, Denmark, 2000. 67
- [KPPM02] T. Keller, M. R. Popovic, I. P. I. Pappas, and P. Y. Muller. Transcutaneous functional electrical stimulator "complex motion". *Artificial Organs*, 26(3):219–223, 2002. 53, 58, 67, 90
- [KS96] Y. M. Kim and P. H. Schimpf. Electrical behavior of defibrillation and pacing electrodes. *Proceedings of the Ieee*, 84(3):446–456, 1996. 150
- [Kuh05] A. Kuhn. Manual for building a model for transcutaneous electrical stimulation with ansys. *IFA Technical Report AUT05-16*, 2005. 187
- [Lap07] L. Lapique. Recherches quantitatives sur l'excitation électrique des nerfs traitée comme une polarisation. *J Physiol Paris*, 9:622–35, 1907. 60
- [LC87] W.E. Lorenson and H.E. Cline. Marching cubes: A high resolution 3d surface construction algorithm. In *International Conference on Computer Graphics and Interactive Techniques*, volume 14, pages 163–9. ACM Press, 1987. 46, 75

- [LD04] Z. Lertmanorat and D. M. Durand. A novel electrode array for diameter-dependent control of axonal excitability: a simulation study. *IEEE Trans Biomed Eng*, 51(7):1242–50, 2004. 114
- [LEM00] L. M. Livshitz, P. D. Einziger, and J. Mizrahi. Current distribution in skeletal muscle activated by functional electrical stimulation: image-series formulation and isometric recruitment curve. *Ann Biomed Eng*, 28(10):1218–28, 2000. 32, 94
- [LEM01] L. M. Livshitz, P. D. Einziger, and J. Mizrahi. A model of finite electrodes in layered biological media: hybrid image series and moment method scheme. *ACES Journal*, 16(2):145–54, 2001. 32, 94, 178
- [LEM02] L. M. Livshitz, P. D. Einziger, and J. Mizrahi. Rigorous green’s function formulation for transmembrane potential induced along a 3-d infinite cylindrical cell. *IEEE Trans Biomed Eng*, 49(12 Pt 2):1491–503, 2002. 6, 32
- [LGD06] Z. Lertmanorat, K. J. Gustafson, and D. M. Durand. Electrode array for reversing the recruitment order of peripheral nerve stimulation: experimental studies. *Ann Biomed Eng*, 34(1):152–60, 2006. 3, 6, 7, 41, 65, 69, 113, 175
- [LK05] M. Lawrence and T. Keller. A transcutaneous electrode measurement system. In *International Functional Electrical Stimulation Society Conference*, pages 400–2, Montreal, Canada, 2005. 132
- [LKK04] M. Lawrence, T. Kirstein, and T. Keller. Electrical stimulation of finger flexors using ‘virtual electrodes’. In *Vienna Int. Workshop on Functional Electrostimulation*, volume 8, 2004. 5, 8, 149
- [LLCM<sup>+</sup>04] G. M. Lyons, G. E. Leane, M. Clarke-Moloney, J. V. O’Brien, and P. A. Grace. An investigation of the effect of electrode size and electrode location on comfort during stimulation of the gastrocnemius muscle. *Med Eng Phys*, 26(10):873–8, 2004. 149, 150, 157, 168



- [LME01] L. M. Livshitz, J. Mizrahi, and P. D. Einziger. Interaction of array of finite electrodes with layered biological tissue: effect of electrode size and configuration. *IEEE Trans Neural Syst Rehabil Eng*, 9(4):355–61, 2001. 54
- [LPK<sup>+</sup>08] M. Lawrence, G. Pitschen, T. Keller, A. Kuhn, and M. Morari. Finger and wrist torque measurement system for the evaluation of grasp performance with neuroprosthesis. *Artif Organs*, in press, 2008. 5, 146, 159, 160, 161
- [LSDK04] M. M. Lowery, N. S. Stoykov, J. P. Dewald, and T. A. Kuiken. Volume conduction in an anatomically based surface emg model. *IEEE Trans Biomed Eng*, 51(12):2138–47, 2004. 52, 68, 97
- [LSTK02] M. M. Lowery, N. S. Stoykov, A. Taflove, and T. A. Kuiken. A multiple-layer finite-element model of the surface emg signal. *IEEE Trans Biomed Eng*, 49(5):446–54, 2002. 7
- [Lyk71] D.T. Lykken. Square-wave analysis of skin impedance. *Psychophysiology*, 7(2):262–75, 1971. 28, 54, 90, 91
- [Man07] D. Many. Integrieren eines parameterischen Modells in ArmSimP und Verluste in Array-Elektroden. *IFA Semester Project*, 2007. 187
- [MB88] D. R. McNeal and L. L. Baker. Effects of joint angle, electrodes and waveform on electrical stimulation of the quadriceps and hamstrings. *Ann Biomed Eng*, 16(3):299–310, 1988. 149
- [McN76] D. R. McNeal. Analysis of a model for excitation of myelinated nerve. *IEEE Trans Biomed Eng*, 23(4):329–37, 1976. 5, 6, 37, 39, 40, 41, 42, 56, 114
- [MG02] C. C. McIntyre and W. M. Grill. Extracellular stimulation of central neurons: influence of stimulus waveform and frequency on neuronal output. *J Neurophysiol*, 88(4):1592–604, 2002. 6, 72, 94

- [MGP04] O. Martinsen, S. Grimnes, and H. Piltan. Cutaneous perception of electrical direct current. *ITBM-RBM*, 25(4):240–3, 2004. 157
- [MH90] C. E. Miller and C. S. Henriquez. Finite element analysis of bioelectric phenomena. *Crit Rev Biomed Eng*, 18(3):207–33, 1990. 6, 26, 33, 85
- [MM08] L. Mesin and R. Merletti. Distribution of electrical stimulation current in a planar multilayer anisotropic tissue. *IEEE Trans Biomed Eng*, 55(2):660–70, 2008. 114, 178
- [MMG04] M. A. Moffitt, C. C. McIntyre, and W. M. Grill. Prediction of myelinated nerve fiber stimulation thresholds: limitations of linear models. *IEEE Trans Biomed Eng*, 51(2):229–36, 2004. 43, 71, 72, 73, 79
- [MRG02] C. C. McIntyre, A. G. Richardson, and W. M. Grill. Modeling the excitability of mammalian nerve fibers: influence of afterpotentials on the recovery cycle. *J Neurophysiol*, 87(2):995–1006, 2002. 6, 42, 45, 56, 64, 116
- [MRRM04] J. Martinek, M. Reichel, F. Rattay, and W. Mayr. Analysis of calculated electrical activation of denervated muscle fibres in the human thigh. In *Proc. of 8th Vienna International Workshop on Functional Electrical Stimulation*, pages 228–31, 2004. 6, 94
- [MSD<sup>+</sup>06] J. Martinek, Y. Stickler, F. Dohnal, M. Reichel, W. Mayr, and F. Rattay. Simulation der funktionellen elektrostimulation im menschlichen Oberschenkel unter Verwendung von femlab. In *Proceedings of the COMSOL Users Conference 2006*, pages 20–23, Frankfurt, 2006. 7, 54
- [Nat79] R. H. Nathan. Functional electrical stimulation of the upper limb: charting the forearm surface. *Med Biol Eng Comput*, 17(6):729–36, 1979. 72, 149
- [Nat92] R. H. Nathan. The isometric action of the forearm muscles. *J Biomech Eng*, 114(2):162–9, 1992. 72, 149

- [NR03] N. H. Nessler and W. Reischer. Measuring device for neutral electrodes in electrosurgery. *Measurement*, 33(2):197–203, 2003. 7
- [Odl83] G.F. Odland. *Structure of the skin*. Oxford University Press, Oxford, 1983. 133
- [PB98] R. Plonsey and R. C. Barr. Electric field stimulation of excitable tissue. *IEEE Eng Med Biol Mag*, 17(5):130–7, 1998. 72
- [PBBJ+05] A. Popovic-Bijelic, G. Bijelic, N. Jorgovanovic, D. Bojanic, M. B. Popovic, and D. B. Popovic. Multi-field surface electrode for selective electrical stimulation. *Artificial Organs*, 29(6):448–452, 2005. 5, 149, 160
- [PBL07] D. Popovic, L. L. Baker, and G. E. Loeb. Recruitment and comfort of bion implanted electrical stimulation: implications for fes applications. *IEEE Trans Neural Syst Rehabil Eng*, 15(4):577–86, 2007. 3
- [PCWS93] D. Panescu, K. P. Cohen, J. G. Webster, and R. A. Stratbucker. The mosaic electrical characteristics of the skin. *IEEE Trans Biomed Eng*, 40(5):434–9, 1993. 7, 132
- [PF86] Charles Polk and CRC Press (Boca Raton FL). *CRC handbook of biological effects of electromagnetic fields*. CRC Press, Boca Raton - Fla., 1986. 35, 36
- [PF07] D. Prodanov and H. K. Feirabend. Morphometric analysis of the fiber populations of the rat sciatic nerve, its spinal roots, and its major branches. *J Comp Neurol*, 503(1):85–100, 2007. 17, 66, 100
- [PGWK97] A. Prochazka, M. Gauthier, M. Wieler, and Z. Kenwell. The bionic glove: an electrical stimulator garment that provides controlled grasp and hand opening in quadriplegia. *Arch Phys Med Rehabil*, 78(6):608–14, 1997. 5, 72, 149
- [PH67] R. Plonsey and D. B. Heppner. Considerations of quasi-stationarity in electrophysiological systems. *Bull Math Biophys*, 29(4):657–64, 1967. 31, 85

- [PKK<sup>+</sup>01] P. H. Peckham, M. W. Keith, K. L. Kilgore, J. H. Grill, K. S. Wuolle, G. B. Thrope, P. Gorman, J. Hobby, M. J. Mulcahey, S. Carroll, V. R. Hentz, and A. Wiegner. Efficacy of an implanted neuroprosthesis for restoring hand grasp in tetraplegia: a multicenter study. *Arch Phys Med Rehabil*, 82(10):1380–8, 2001. 5
- [PKP<sup>+</sup>01] M. R. Popovic, T. Keller, I. P. Pappas, V. Dietz, and M. Morari. Surface-stimulation technology for grasping and walking neuroprosthesis. *IEEE Eng Med Biol Mag*, 20(1):82–93, 2001. 5
- [PPK02] M. R. Popovic, D. B. Popovic, and T. Keller. Neuroprostheses for grasping. *Neurol Res*, 24(5):443–52, 2002. 159
- [PSP<sup>+</sup>99] D. Popovic, A. Stojanovic, A. Pjanovic, S. Radosavljevic, M. Popovic, S. Jovic, and D. Vulovic. Clinical evaluation of the bionic glove. *Arch Phys Med Rehabil*, 80(3):299–304, 1999. 5
- [PWS94] D. Panescu, J. G. Webster, and R. A. Stratbucker. A nonlinear finite element model of the electrode-electrolyte-skin system. *IEEE Trans Biomed Eng*, 41(7):681–7, 1994. 7, 35, 132, 133, 140
- [PYS<sup>+</sup>05] A. Patriciu, K. Yoshida, J. J. Struijk, T. P. DeMonte, M. L. Joy, and H. Stodkilde-Jorgensen. Current density imaging and electrically induced skin burns under surface electrodes. *IEEE Trans Biomed Eng*, 52(12):2024–31, 2005. 131
- [RA63] S. Ruch and J.A. Abildskov. Resistivity of body tissues at low frequencies. *Circ. Res.*, 12:40–50, 1963. 28
- [RACS98] J. Patrick Reilly, Hermann Antoni, Michael A. Chilbert, and James D. Sweeney. *Applied bioelectricity from electrical stimulation to electropathology*. Springer, New York etc., 1998. 7, 17, 18, 19, 27, 33, 34, 35, 36, 43, 57, 65, 80, 114, 115, 132, 144, 145, 152, 157, 162, 170
- [Rat88] F. Rattay. Modeling the excitation of fibers under surface electrodes. *IEEE Trans Biomed Eng*, 35(3):199–202, 1988. 6, 21, 38, 42, 45, 72

- [Rat90] Frank Rattay. *Electrical nerve stimulation theory, experiments and applications*. Springer, Wien etc., 1990. 6, 42, 43, 56, 132
- [Rat08] F. Rattay. Current distance relations for fiber stimulation with pointsources. *IEEE Trans Biomed Eng*, 55(3):1122–7, 2008. 107
- [RB87] J. P. Reilly and R. H. Bauer. Application of a neuroelectric model to electrocutaneous sensory sensitivity: parameter variation study. *IEEE Trans Biomed Eng*, 34(9):752–4, 1987. 64, 107, 144, 145
- [RBMR02] M. Reichel, T. Breyer, W. Mayr, and F. Rattay. Simulation of the three-dimensional electrical field in the course of functional electrical stimulation. *Artif Organs*, 26(3):252–5, 2002. 7, 8, 32, 94
- [RHK<sup>+</sup>94] N. J. Rijkhoff, J. Holsheimer, E. L. Koldewijn, J. J. Struijk, P. E. van Kerrebroeck, F. M. Debruyne, and H. Wijkstra. Selective stimulation of sacral nerve roots for bladder control: a study by computer modeling. *IEEE Trans Biomed Eng*, 41(5):413–24, 1994. 66, 100
- [RKd<sup>+</sup>96] N. J. Rijkhoff, E. L. Koldewijn, W. d’Hollosy, F. M. Debruyne, and H. Wijkstra. Morphometric data of canine sacral nerve roots with reference to electrical sacral root stimulation. *Neurourolog Urolyn*, 15(3):235–48, 1996. 17
- [RMMR04] M. Reichel, J. Martinek, W. Mayr, and F. Rattay. Functional electrical stimulation of denervated skeletal muscle fibers in 3d human thigh - modeling and simulation. In *Proc. of 8th Vienna International Workshop on Functional Electrical Stimulation*, pages 44–7, 2004. 6, 85, 150
- [RMR99] M. Reichel, W. Mayr, and F. Rattay. Computer simulation of field distribution and excitation of denervated muscle fibers caused by surface electrodes. *Artif Organs*, 23(5):453–6, 1999. 94
- [SC07] L. R. Sheffler and J. Chae. Neuromuscular electrical stimulation in neurorehabilitation. *Muscle Nerve*, 35(5):562–90, 2007. 5, 159

- [SD01] S. Silbernagl and A. Despopoulos. *Taschenatlas der Physiologie*, volume 5. Thieme, 2001. 16, 17
- [SG06] M. A. Schiefer and W. M. Grill. Sites of neuronal excitation by epiretinal electrical stimulation. *IEEE Trans Neural Syst Rehabil Eng*, 14(1):5–13, 2006. 72
- [SKH<sup>+</sup>07a] N. Sha, L. P. Kenney, B. W. Heller, A. T. Barker, D. Howard, and W. Wang. The effect of the impedance of a thin hydrogel electrode on sensation during functional electrical stimulation. *Med Eng Phys*, 2007. 140
- [SKH<sup>+</sup>07b] N. Sha, LPJ. Kenney, BH. Heller, AT. Barker, D. Howard, and M. Moatamedi. A fe model to identify electrode influence on current distribution in the skin. In *Vienna Int. Workshop on Functional Electrostimulation*, volume 9, pages 155–8, 2007. 132, 133, 140
- [SKPS05] O. Schuhfried, C. Kollmann, and T. Paternostro-Sluga. Excitability of chronic hemiparetic muscles: determination of chronaxie values and strength-duration curves and its implication in functional electrical stimulation. *IEEE Trans Neural Syst Rehabil Eng*, 13(1):105–9, 2005. 56, 60, 143
- [SLTK01] N. S. Stoykov, M. M. Lowery, A. Taflove, and T. A. Kuiken. A finite element analysis of muscle tissue capacitive effects and dispersion in emg. *Proceeding of the 23rd Annual EMBS International Conference, Istanbul, Turkey*, pages 1044–7, 2001. 86
- [SMD87] J.D. Sweeney, J.T. Mortimer, and D. Durand. Modeling of mammalian myelinated nerve for functional neuromuscular stimulation. In *Proc. of IEEE 9th Annual Conference of the Engineering in Medicine and Biology Society*, pages 1577–8, 1987. 6, 39, 40, 42, 56
- [SMHR07] Y. Strickler, J. Martinek, C. Hofer, and F. Rattay. A finite element model of the electrically stimulated human thigh: Changes due to denervation and training. In *Proc. of 9th Vienna International Workshop on Functional Electrical Stimulation*, pages 20–3, Krems, Austria, 2007. 7, 124

- [SMitG<sup>+</sup>00] G. J. Snoek, I. Jzerman MJ, F. A. in 't Groen, T. S. Stoffers, and G. Zilvold. Use of the nese handmaster to restore handfunction in tetraplegia: clinical experiences in ten patients. *Spinal Cord*, 38(4):244–9, 2000. 159
- [SNP95] S. Saxena, S. Nikolic, and D. Popovic. An emg-controlled grasping system for tetraplegics. *J Rehabil Res Dev*, 32(1):17–24, 1995. 5
- [SS07] S. N. Sotiropoulos and P. N. Steinmetz. Assessing the direct effects of deep brain stimulation using embedded axon models. *J Neural Eng*, 4(2):107–19, 2007. 7, 41
- [Sta05] S. Standring. *Gray's Anatomy*. 39 edition, 2005. 15, 16, 18, 22, 33, 34, 40, 57, 66, 91, 107, 114, 116, 161, 163, 186
- [STT08] M. A. Schiefer, R. J. Triolo, and D. J. Tyler. A model of selective activation of the femoral nerve with a flat interface nerve electrode for a lower extremity neuroprosthesis. *IEEE Trans Neural Syst Rehabil Eng*, 16(2):195–204, 2008. 113
- [TMV99] Gerhard Thews, Ernst Mutschler, and Peter Vaupe. *Anatomie, Physiologie, Pathophysiologie des Menschen*. Wissenschaftliche Verlagsgesellschaft, Stuttgart, 5., völlig neu bearb. und erw. Aufl. edition, 1999. 15, 18, 19, 20, 21
- [TNK07] H. Takahashi, M. Nakao, and K. Kaga. Selective activation of distant nerve by surface electrode array. *IEEE Trans Biomed Eng*, 54(3):563–9, 2007. 32, 94
- [Val01] J. Valentin. Basic anatomical and physiological data for use in radiological protection: reference values. *Annals of the ICRP*, 2001. 33, 34
- [vB77] A. van Boxtel. Skin resistance during square-wave electrical pulses of 1 to 10 ma. *Med Biol Eng Comput*, 15(6):679–87, 1977. 35, 90
- [VCR67] L. Vodovnik, W. J. Crochetiere, and J. B. Reswick. Control of a skeletal joint by electrical stimulation of antagonists. *Med Biol Eng*, 5(2):97–109, 1967. 65

- [VvD06] K. Verhoeven and J. G. van Dijk. Decreasing pain in electrical nerve stimulation. *Clin Neurophysiol*, 117(5):972–8, 2006. 48, 150, 152, 157
- [VVG<sup>+</sup>92] C. R. Voorhees, 3rd Voorhees, W. D., L. A. Geddes, J. D. Bourland, and M. Hinds. The chronaxie for myocardium and motor nerve in the dog with chest-surface electrodes. *IEEE Trans Biomed Eng*, 39(6):624–8, 1992. 56
- [VvVS<sup>+</sup>89] P. H. Veltink, B. K. van Veen, J. J. Struijk, J. Holzheimer, and H. B. Boom. A modeling study of nerve fascicle stimulation. *IEEE Trans Biomed Eng*, 36(7):683–92, 1989. 114
- [WA05] R. P. Williamson and B. J. Andrews. Localized electrical nerve blocking. *IEEE Trans Biomed Eng*, 52(3):362–70, 2005. 3
- [WGD92] E. N. Warman, W. M. Grill, and D. Durand. Modeling the effects of electric fields on nerve fibers: determination of excitation thresholds. *IEEE Trans Biomed Eng*, 39(12):1244–54, 1992. 43, 71, 72, 73, 79
- [www] [www.semcad.com](http://www.semcad.com). Semcad by schmid und partner engineering ag. 32
- [YD05] P. B. Yoo and D. M. Durand. Selective recording of the canine hypoglossal nerve using a multicontact flat interface nerve electrode. *IEEE Trans Biomed Eng*, 52(8):1461–9, 2005. 114
- [YY81] T. Yamamoto and Y. Yamamoto. Non-linear electrical properties of skin in the low frequency range. *Med Biol Eng Comput*, 19(3):302–10, 1981. 28, 35, 90
- [Zie01] C. M. Zierhofer. Analysis of a linear model for electrical stimulation of axons—critical remarks on the ”activating function concept”. *IEEE Trans Biomed Eng*, 48(2):173–84, 2001. 41
- [ZKI<sup>+</sup>02] X. L. Zhao, Y. Kinouchi, T. Iritani, T. Morimoto, and M. Takeuchi. Estimation of multi-layer tissue conductivities from non-invasively measured bioresistances using



divided electrodes. *Ieice Transactions on Information and Systems*, E85D(6):1031–1038, 2002. 7



# Curriculum Vitae

## Personal Information

Andreas Kuhn  
Born June 11th 1979, Uster, Switzerland  
Citizen of Schwerzenbach ZH, Switzerland

## Education

- 2004–2008 PhD, ETH Zurich, Automatic Control Lab, Prof. Manfred Morari  
Modeling Transcutaneous Electrical Stimulation
- 2001–2007 Lectures in Management, Business, Economics, and Finance (at ETH)
- 2003–2004 Masters Thesis at University of Calgary, Canada  
Sitespecific Change Measurement of Micro-Structural Bone Adaptation
- 1999–2004 MSc ETH in Information Technology and Electrical Engineering

## Work Experience

- 2008–curr. Technology / Engineering Consultant at Altran AG
- 2003 Software Developer at SPEAG (ITIS)
- 2002 Development Engineer at Oerlikon Contraves AG, Simulation Systems and Engineering Branch
- 2001 Internship at Mettler-Toledo GmbH, Signal Processing Branch

## Awards

- 2008 S M Perren Research Award for the paper: "Using temporal trends of 3D bone micro-architecture to predict bone quality" by Yves Pauchard, Corinne Mattmann, Andreas Kuhn, Jürg Gasser, and Steven Boyd